POLITECNICO DI TORINO

Corso di Laurea Magistrale
in Ingegneria Energetica e Nucleare

Tesi di Laurea Magistrale

Development of doped Bi_2O_3 based composite cathodes for reversible solid oxide cells

Relatore
prof. Massimo Santarelli
Co-relatore
prof. San Ping Jiang

Candidato
Lorenzo Catellani

A.A. 2017-2018

Alla Ca’ ed Pepino
A Nicole

ABSTRACT

The reversible Solid Oxide Fuel Cells or Solid Oxide Cells (SOCs) will play a key role in the decarbonisation of the energy sector, thanks to their higher efficiency and fuel flexibility as compared to other typologies of fuel cell. Decreasing the operational temperature of the cell in a 600-800 °C range of temperatures is a fundamental task in order to make these systems more competitive in the market, widening the material selection of the components, improving the long-term stability of the cell, reducing the start-up time and lowering the overall cost, thanks to cheaper metal alloy materials adopted for interconnectors and manifold components. However, a lower operating temperature would decrease the electronic and ionic conductivity of the electrolyte and of the electrodes and the kinetic of the electrochemical reactions, increasing resistivities and polarization losses. In an anode supported cell with a very thin high-conductive electrolyte working at reduced temperatures, the major part (up to 65%) of the overall polarization losses can be attributed to the cathode, due to the high-activation energy and slow kinetic for the oxygen reduction reaction. For this reason, the efforts of many researchers in the last years were focused in the improvement of the cathode performance and stability to enhance the power density and the reliability of intermediate temperature SOC.

The synthesis of composite cathode, incorporating an excellent ion conductive phase, has been proved to enhance the performance and the stability of the electrode. In this study, we synthetized composite cathodes with a 50 wt.% of an electronic conductor or a MIEC material (LSM, LSCF and BSCF) and 50 wt.% of erbium stabilized bismuth oxide (ESB), an excellent ionic conductor, adopting the sol-gel method. The composite cathodes were directly applied via the *in situ* approach on YSZ pellets and then electrochemically tested under constant cathodic and anodic polarization and open circuit condition. We observed how the polarization, especially the cathodic current, helped the formation of an effective electrode/electrolyte interface in the first 2 hours of the test, decreasing considerably the contact resistance. After the test, the microstructure and the morphology of the electrode/electrolyte interface were characterized with a focus ion beam scanning electron microscope. After the development of mechanical mixed cathodes, we improved the performances and the stability, especially in electrolysis mode, of LSM-ESB and BSCF-ESB composite cathodes, synthetizing nanostructured electrodes through the gelation

method, a simple and effective decoration approach. We reached polarization resistances of less than 0.1 Ω cm^2 after 12-hour cathodic polarization at 700 °C in the case of ESB decorated LSM cathode, much lower than the one recorded for the pristine LSM cathode with the same configuration at higher temperature.

In the first chapter, a brief description and explanation of the fundamentals of fuel cells and reversible fuel cells is proposed. Then, in the second chapter, the solid oxide cells are described more in detail, with a focus on the cathode, on the *in situ* approach and on the electrode/electrolyte interface. After that, we explained the methods and the instruments used in the electrochemical test and in the microstructural characterization. At the end, the results of the experiments are proposed and discussed.

CONTENTS

Introduction 13
- The fuel cell 16
- Typologies of fuel cell 19
- Performances of a fuel cell 20
- Electrolyzers and reversible cells 27

The Solid Oxide Cell (SOC) 29
- Description of the components of the SOC 31
- The cathode 32
  - LSM 35
  - LSCF 37
  - BSCF 40
  - Composite cathodes 41
  - In situ approach: electrochemically induced electrode/electrolyte interface 42

Experimental 45
- Fabrication of the YSZ-supported half-cell and in Situ assembled cathode 45
- The electrochemical test 48
- Microscopic characterization 49

Results and Discussion 51
- LSM-ESB 51
  - Thermo-compatibility tests 51
  - Electrochemical performances 52
  - Microstructural analysis 59
- ESB decorated LSM 66
  - Electrochemical tests 66
  - Microstructural analysis 72
- LSCF-ESB 77
  - Thermo-compatibility tests 77
  - Electrochemical tests 78
- BSCF-ESB 84
  - Thermo-compatibility tests 84
  - Electrochemical tests 85
- ESB decorated BSCF 91
  - Electrochemical tests 92
  - Microstructural Analysis 99

Conclusions 103

LIST OF FIGURES

Figure 1 Actual efficiency of some of the most popular systems of production of energy as function of the power 13

Figure 2 Comparison of CO_2 emissions between combustion-based systems and a natural gas-fed SOFC 14

Figure 3 Schematic of a typical planar PEMFC 17

Figure 4 Schematic of a typical planar SOFC 17

Figure 5 A 3D scheme of a stack composed by 3 cells connected in series 18

Figure 6 Schematic of the exothermic oxidation of Hydrogen 21

Figure 7 Schematic of the additive resistances attributed to the different components of the cell 25

Figure 8 Theoretical polarization curve of a typical fuel cell 27

Figure 9 Schematic of the typical geometrical configurations of a SOFC 32

Figure 10 Schematic of the three strategies to create TPB in SOFC cathodes 33

Figure 11 Schematic of the three possible reactions paths of ORR 34

Figure 12 Oxygen deficient perovskite structure and diffusion of oxygen vacancies through the structure 36

Figure 13 Schematic diagram showing the elementary steps in a MIEC material 38

Figure 14 Ionic conductivity as function of the temperature of different solid oxide electrolytes 41

Figure 15 Scheme of the LSM electrode/YSZ electrolyte interface formation under the influence of (a) high temperature sintering, e.g., 1150 °C and (b) cathodic polarization at normal SOFC operation conditions, e.g. 800 °C. 43

Figure 16 Scheme of the in situ cathode application process 44

Figure 17 Fabrication steps for cells with a conventionally high temperature sintered LSCF and GDC interlayer process and with in situ assembled LSCF electrode 44

Figure 18 Schematic and behaviour of the three-electrode setup of the YSZ electrolyte supported half-cell 45

Figure 19 Schematic of the synthesis of nanostructured ESB decorated LSM powder via the gelation process and in situ direct assembly of the ESB-LSM electrode in a Ni-YSZ anode supported YSZ electrolyte cell 47

Figure 20 XRD patterns of the mixed LSM-ESB powder 51

Figure 21 a) Impedance spectra and b) polarization response of direct assembled mixed LSM-ESB cathode under cathodic polarization at 250 mA cm^{-2} *and at 700 °C* 53

Figure 22 a) Impedance spectra and b) polarization response of direct assembled mixed LSM-ESB cathode under cathodic polarization at 500 mA cm^{-2} *and at 700 °C* 54

Figure 23 a) Impedance spectra and b) polarization response of direct assembled mixed LSM-ESB cathode under anodic polarization at 250 mA cm-2 and at 700 °C 56

Figure 24 a) Impedance spectra and b) polarization response of direct assembled mixed LSM-ESB cathode under anodic polarization at 500 mA cm-2 and at 700 °C 57

Figure 25 Impedance spectra of direct assembled mixed LSM-ESB cathode under open circuit condition at 700 °C ____ *58*

Figure 26 SEM images at different resolution of the YSZ surface after 12-hour cathodic polarization at 250 mA cm^{-2} and removal of the direct applied mixed LSM-ESB cathode by acid treatment ____ *59*

Figure 27 SEM images at different resolution of the YSZ surface after 12-hour cathodic polarization at 250 mA cm-2 and removal of the directly assembled mixed LSM-ESB cathode by adhesive tape ____ *60*

Figure 28 SEM images at different resolution of the YSZ surface after 12-hour anodic polarization at 250 mA cm-2 and removal of the direct applied mixed LSM-ESB cathode by acid treatment ____ *61*

Figure 29 SEM images at different resolution of the YSZ surface after 12-hour anodic polarization at 250 mA cm-2 and removal of the direct applied mixed LSM-ESB cathode by adhesive tape ____ *61*

Figure 30 STEM-EDS maps of electrode/electrolyte interface after the directly assembled mixed LSM-ESB cathode was polarized at 250 mA cm^{-2} and 700 °C for 20 h under fuel cell mode ____ *62*

Figure 31 Detail of FIB-STEM elemental mapping of directly assembled mixed LSM-ESB cathode after 12-hour 250 mA cm^{-2} cathodic polarization, showing ESB and LSM particles incorporated at the interface ____ *63*

Figure 32 STEM-EDS maps of electrode/electrolyte interface after the directly assembled mixed LSM-ESB cathode was polarized at 250 mA cm−2 and 700 °C for 20 h under electrolysis mode ____ *64*

Figure 33 Detail of FIB-STEM elemental mapping of directly assembled mixed LSM-ESB cathode after 12-hour 250 mA cm-2 anodic polarization, showing ESB and LSM particles incorporated at the interface ____ *65*

Figure 34 a) Impedance spectra and b) polarization response of direct assembled ESB decorated LSM cathode under cathodic polarization at 250 mA cm-2 and at 700 °C ____ *67*

Figure 35 a) Impedance spectra and b) polarization response of direct assembled ESB decorated LSM cathode under cathodic polarization at 500 mA cm-2 and at 700 °C ____ *68*

Figure 36 a) Impedance spectra and b) polarization response of direct assembled ESB decorated LSM cathode under anodic polarization at 250 mA cm-2 and at 700 °C ____ *70*

Figure 37 a) Impedance spectra and b) polarization response of direct assembled ESB decorated LSM cathode under anodic polarization at 500 mA cm-2 and at 700 °C ____ *71*

Figure 38 Impedance spectra of direct assembled ESB decorated LSM cathode under open circuit condition at 700 °C ____ *72*

Figure 39 SEM images at different resolution of the YSZ surface after 12-hour anodic polarization at 250 mA cm^{-2} and removal of the direct applied ESB decorated LSM cathode by adhesive tape ____ *73*

Figure 40 SEM images at different resolution of the YSZ surface after 12-hour anodic polarization at 250 mA cm^{-2} and removal of the direct applied ESB decorated LSM cathode by acid treatment ____ *73*

Figure 41 SEM images at different resolution of the YSZ surface after 12-hour open circuit condition at 700 °C and removal of the direct applied ESB decorated LSM cathode by acid treatment ____ *74*

Figure 42 STEM-EDS maps of electrode/electrolyte interface after the directly assembled ESB decorated LSM cathode was polarized at 250 mA cm^{-2} and 700 °C for 20 h under fuel cell mode ____ *75*

Figure 43 STEM-EDS maps of electrode/electrolyte interface after the directly assembled ESB decorated LSM cathode was polarized at 250 mA cm^{-2} and 700 °C for 20 h under electrolysis mode ____ *76*

Figure 44 XRD patterns of the mixed LSCF-ESB powder 77

Figure 45 a) Impedance spectra and b) polarization response of direct assembled mixed LSCF-ESB cathode under cathodic polarization at 250 mA cm^{-2} *and at 700 °C* 79

Figure 46 a) Impedance spectra and b) polarization response of direct assembled mixed LSCF-ESB cathode under cathodic polarization at 250 mA cm^{-2} *and at 700 °C* 80

Figure 47 Impedance spectra and polarization response of direct assembled mixed LSCF-ESB cathode under anodic polarization at 250 mA cm^{-2} *and at 700 °C* 81

Figure 48 Impedance spectra and polarization response of direct assembled mixed LSCF-ESB cathode under anodic polarization at 500 mA cm^{-2} *and at 700 °C* 82

Figure 49 Impedance spectra of direct assembled mixed LSCF-ESB cathode under open circuit at 700 °C 83

Figure 50 XRD patterns of the mixed BSCF-ESB powder 84

Figure 51 a) Impedance spectra and b) polarization response of direct assembled mixed BSCF-ESB cathode under cathodic polarization at 250 mA cm^{-2} *and at 650 °C* 86

Figure 52 a) Impedance spectra and b) polarization response of direct assembled mixed BSCF-ESB cathode under cathodic polarization at 500 mA cm^{-2} *and at 650 °C* 87

Figure 53 a) Impedance spectra and b) polarization response of direct assembled mixed BSCF-ESB cathode under anodic polarization at 250 mA cm^{-2} *and at 650 °C* 89

Figure 54 a) Impedance spectra and b) polarization response of direct assembled mixed BSCF-ESB cathode under anodic polarization at 500 mA cm^{-2} *and at 650 °C* 90

Figure 55 Impedance spectra of direct assembled mixed BSCF-ESB cathode under open circuit at 650 °C 91

Figure 56 a) Impedance spectra and b) polarization response of direct assembled ESB decorated BSCF cathode under cathodic polarization at 250 mA cm^{-2} *and at 650 °C* 93

Figure 57 a) Impedance spectra and b) polarization response of direct assembled ESB decorated BSCF cathode under cathodic polarization at 500 mA cm^{-2} *and at 650 °C* 94

Figure 58 a) Impedance spectra and b) polarization response of direct assembled ESB decorated BSCF cathode under anodic polarization at 250 mA cm^{-2} *and at 650 °C* 96

Figure 59 a) Impedance spectra and b) polarization response of direct assembled ESB decorated BSCF cathode under anodic polarization at 250 mA cm^{-2} *and at 650 °C* 97

Figure 60 Impedance spectra of direct assembled ESB decorated BSCF cathode under open circuit at 650 °C 98

Figure 61 SEM images at different resolution of the YSZ surface after 12-hour cathodic polarization at 250 mA cm^{-2} *and removal of the direct applied ESB decorated BSCF cathode by adhesive tape* 99

Figure 62 SEM images at different resolution of the YSZ surface after 12-hour cathodic polarization at 250 mA cm^{-2} *and removal of the direct applied ESB decorated BSCF cathode by acid treatment* 100

Figure 63 SEM images at different resolution of the YSZ surface after 12-hour anodic polarization at 250 mA cm^{-2} *and removal of the direct applied ESB decorated BSCF cathode by adhesive tape* 100

Figure 64 SEM images at different resolution of the YSZ surface after 12-hour anodic polarization at 250 mA cm^{-2} *and removal of the direct applied ESB decorated BSCF cathode by acid treatment* 101

INTRODUCTION

The fuel cell technology has gained much interest in the past three decades thanks to the development of environmental concern about global warming and the need to reduce the CO_2 emissions among the industrialized countries of the world. The European Commission finds in these systems one of the main actors, especially in transport application, in order to reach the objectives of reduction of oil dependence and pollution in cities[1]. From the first demonstrations conducted by Sir William Grove in the first half of the XIX century, the fuel cells have become the most efficient technology to convert the chemical energy contained in hydrocarbons directly into electricity (e.g. the internal combustion engine and gas turbines) in terms of efficiency and performances, as shown in Figure 1[2,3].

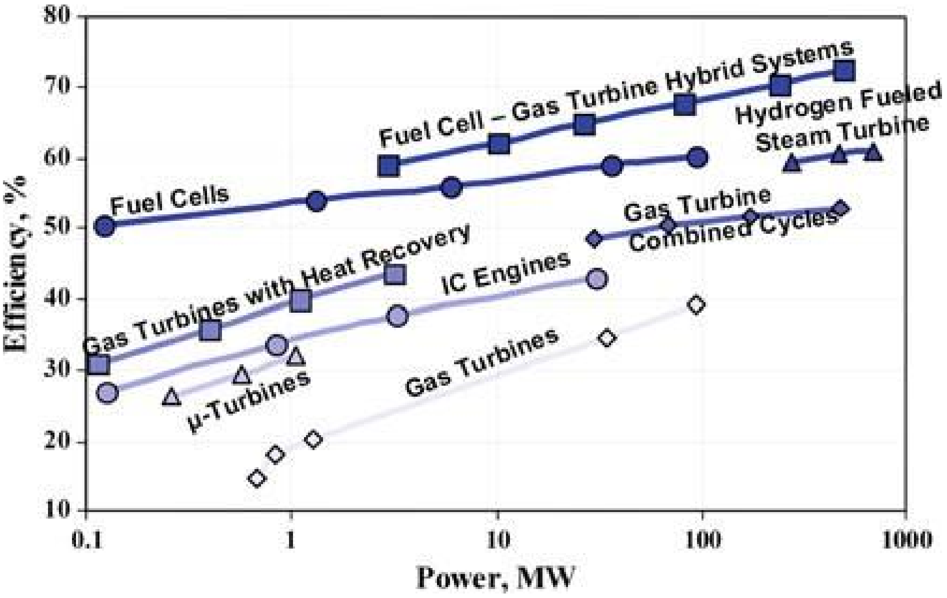

Figure 1 Actual efficiency of some of the most popular systems of production of energy as function of the power

The main reason of these higher efficiencies is that, in these devices, the chemical energy contained in the fuel is directly converted in electrical energy and heat, avoiding the combustion of the fuel and the efficiency constrains regarding the Carnot cycle. Part of the generated heat is necessary to sustain the electrochemical conversion, while the rest, especially in the case of medium and high temperature fuel cells, can be recovered in a heat cogeneration configuration or coupled with gas or steam turbines, further enhancing the efficiency in both cases.

Thanks to this issue, the Green House Gases (GHG) emissions are considerably reduced during the operation of the fuel cell, as shown in the Figure 2, and they can be avoided adopting a fuel obtained by renewable energy sources (RES), such as biogas[4], or hydrogen. Moreover, since the combustion process is avoided, nitrous oxides (NO_x) and particulate matter are not produced, as well as sulphur oxides (SO_x), since they are removed because they are detrimental for the cell. The reduction of these pollutants is necessary to solve problems such as the air pollution in modern and industrialized cities.

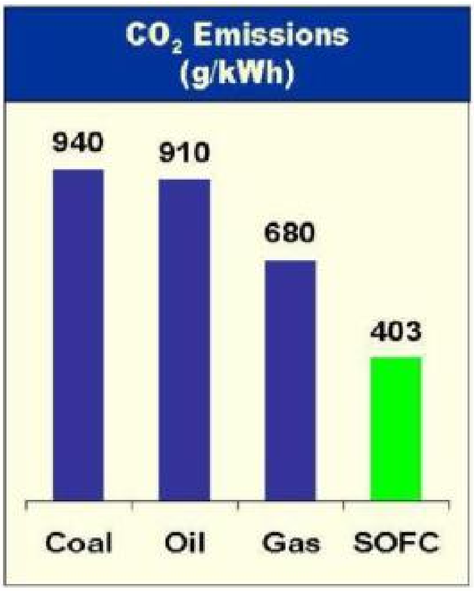

Figure 2 Comparison of CO_2 emissions between combustion-based systems and a natural gas-fed SOFC [source: Acumentrics, www.acumentrics.com]

From Figure 1 another important feature of these system can be noted: the excellent modularity of the stack, thanks also to the high efficiency at partial loads, permits to design the fuel cell plant in a wide range of power outputs, widening in this way the applications of this technology, form the stationary power production in a large range of different plants size (form micro-fuel cells with power output of less than 1 W to multi-MW prime power generation plants), to the transports and cogeneration systems[5].

In the future, in an energy sector where the renewable energy sources (RES) will gradually substitute the traditional carbon-based way of energy production, one of the most promising application for the fuel cell technology is the use as storage of the excess of electrical energy produce by the RES in form of chemical energy (i.e. hydrogen or carbon monoxide). Fuel cells have the capability to reverse the direction of the electrochemical reaction, i.e. to produce, starting from the products of the fuel cell mode

(H_2O and/or CO_2), their reactants (H_2 and/or CO), supplying electrical and thermal energy to the system. The electrical energy produced by solar and wind technology is intermittent and low predictable, then a storage would increase sensibly the yield of the plant, making it more profitable, and would improve the safety and the management of the electrical grid.

The high temperatures that can be reached in some typologies of fuel cells allow the plant to be fed by natural gas or biogas, so an advantageous fuel flexibility, due to the possibility of the internal reforming of methane in the stack.

However, the success on the energy supply market is limited by serious disadvantages. First, the fuel cell-based systems are still far from being cost-effective, due to the high cost of stack materials (e.g. precious catalysts and coated bipolar plate) and to the high cost of Balance of Plant components (e.g. pumps, fuel supply subsystem, blowers), that generally constitute about half of the cost of the system and decrease the theoretic electrical efficiency of the cells. Moreover, when hydrogen is adopted as fuel of the plant, its price is much higher than the one of a system fed by natural gas. In the German market, one of the most advanced in the hydrogen field, the total price for hydrogen produced by renewable energy sources is about 0.18 €/kWh, while the price of the natural gas is about 0.017 €/kWh. Nevertheless, some reports forecast that the price of hydrogen will cost less than methane in 2040, thanks to the higher electricity share from renewables in the grid, the lower cost of the electrolyser due to a higher commercialization and the higher cost of natural gas, as expected by the International Energy Agency (IEA)[6]. Even the absence of a capillary hydrogen dispatching grid and the safety issues in the storage of hydrogen are further obstacles in the diffusion of this technology.

At last, one of the most challenging issues is the necessary increase in the durability of fuel cells, especially in the stationary distributed generation sector, in order to become a good alternative to the current ways of power production. Nowadays, the durability of the system is mainly affected by the degradation of the cell materials in the performances due to poisoning and contamination by pollutants and impurities.

The fuel cell

As mentioned above, a fuel cell is a device that converts directly the chemical energy contained in the fuel into electrical energy and heat without the irreversible oxidation with an oxidant gas (air). The reaction is electrochemical and spatially split in two different areas of the system. The cell is essentially composed by two electrodes divided by an electrolyte: at the anode side, the fuel is oxidized, releasing electrons to an external electrical circuit; at the cathode side, the oxygen (from the air or pure) is reduced, thanks to the presence of the electronic current flowing from the external circuit. The electrolyte layer has the function of maintain the electric field generated by the two reactions, avoiding the diffusion of molecular species. The electro-neutrality, necessary to complete the redox reaction, is obtained by the flow of the so-generated charged species: the electrons flowing in the external circuit, due to the very low electronic conductivity of the electrolyte layer, producing an electrical current (the useful effect of the fuel cell), and the ions migration taking place in the electrolyte.

Considering a fuel cells fed by hydrogen, as it is the object of this study, the total redox reaction occurring in the system is the following:

$$2H_2 + O_2 \rightarrow 2H_2O$$

The reaction is split in two electrochemical half reactions occurring at the electrodes[7], fed by a coherent flow of electrons, driven by a potential gradient between the two electrodes.

Hydrogen oxidation reaction (HOR) at the anode side: $2H_2 \leftrightarrow 4H^+ + 4e^-$

Oxygen reduction reaction (ORR) at the cathode side: $O_2 + 4e^- \leftrightarrow 2O^{2-}$

Water is form at the anode or at the cathode, if the species migrating are oxygen ions or hydrogen ions respectively, depending on the type of the cell used and the electrolyte material adopted. The process is illustrated in Figure 3 and Figure 4[7], showing the case of a low temperature fuel cell (PEMFC) and the corresponding high temperature fuel cell (SOFC). The cells showed are characterized by the planar configuration, much more used and simple than the alternative tubular one.

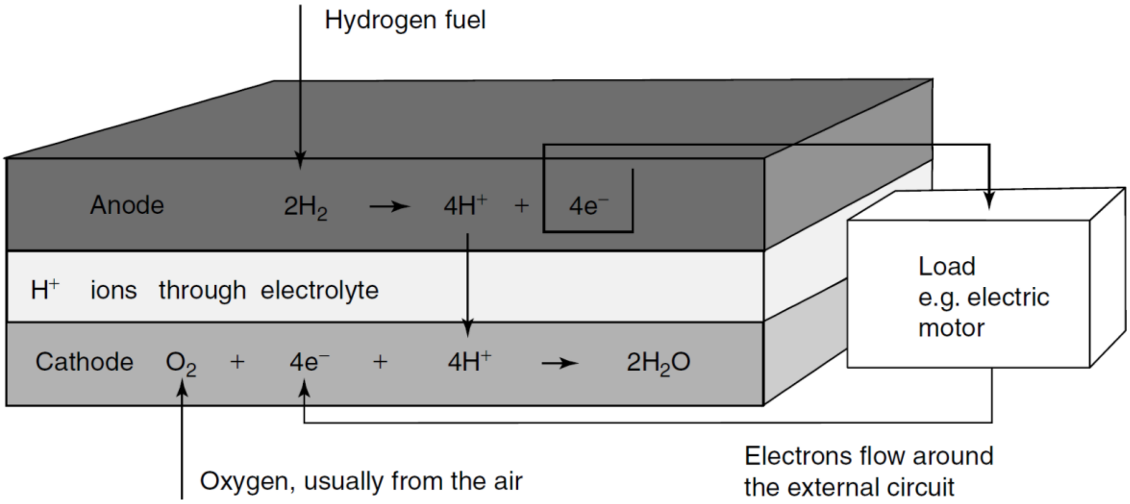

Figure 3 Schematic of a typical planar PEMFC

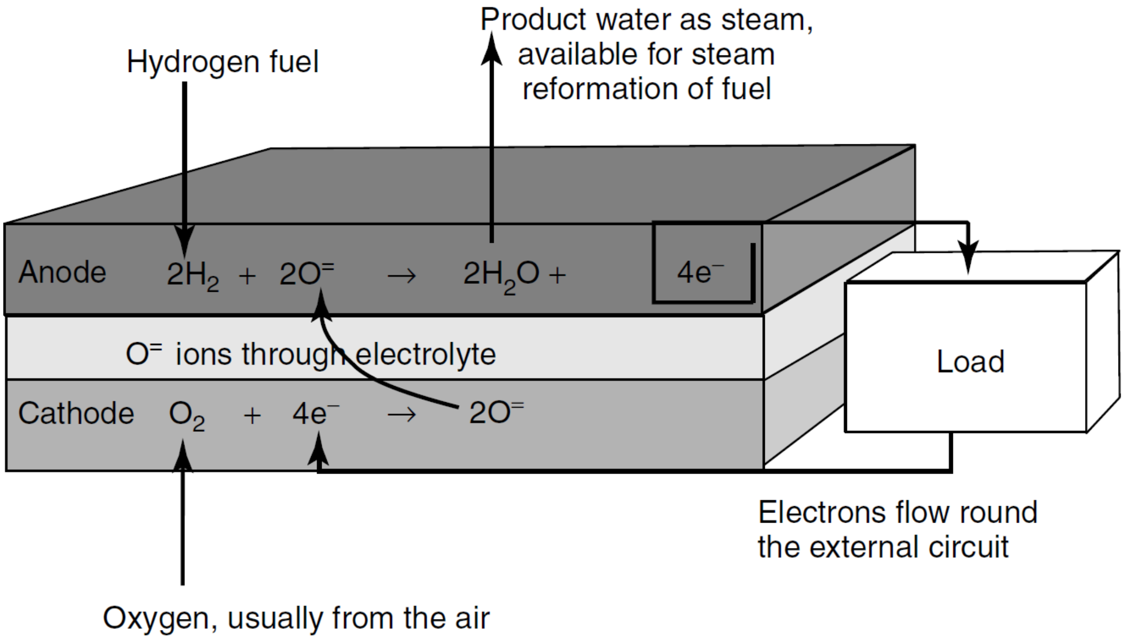

Figure 4 Schematic of a typical planar SOFC

Hydrogen is the most widely adopted fuel for the fuel cells, even if, as mentioned above, it is possible to feed these systems with hydrocarbons, such as natural gas, that directly available in the environment, and so less expensive. However, the presence of carbon monoxide (CO) in the mixture, due to chemical reactions in the mixture, is poisoning and detrimental for the electrodes of the fuel cells operating at low temperature. At high temperature, the kinetics of the reaction avoids the poisoning of the electrodes. In order to give a more general description of these systems, hydrogen will be considered as fuel for the fuel cells during this study.

The chemical reaction occurring in the cell is exothermic, in fact the difference between the chemical energy of the reaction and the electrical energy produced is released in form of heat. For this reason, a heat managing system is necessary in these systems in order to operate at constant temperature, for example exploiting the heat in excess to pre-heat the inlet reactants or in a cogeneration system.

The electrical power produced in a single cell is limited for thermodynamic and kinetic reasons and is not sufficient in typical practical applications. In order to enhance the overall voltage, avoiding excessive ohmic losses due to high currents produced, typical fuel cells plants are formed by a stack of several cells connected in series. The connection in series is obtained through conductive interconnectors, called bipolar plates, that are in contact with both the anode and the cathode of two different contiguous cells. The interconnectors act both as a straightforward electrical connection between the cells of the stack and as inlets for the feeding flows of the cells. The bipolar plates must be good electronic conductor, impermeable to avoid the crossover of different flows of chemicals, and easily machined to obtain the flow channels on their surface. Figure 5 shows a 3-cell stack, highlighting the double function as electronic conductor and as inlet of the gases of the interconnector.

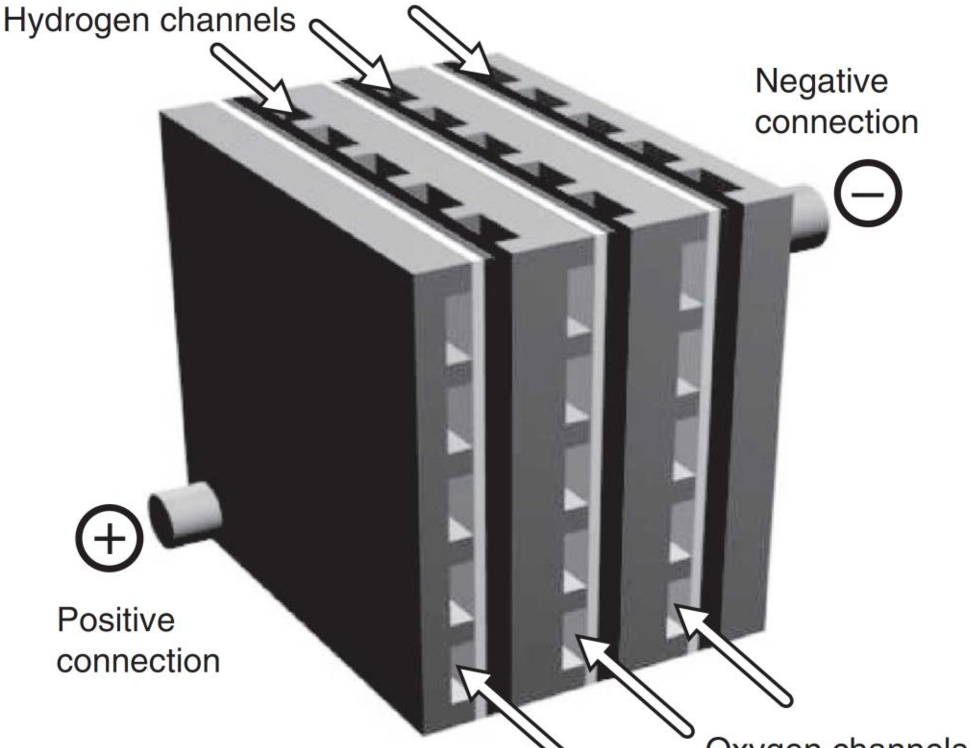

Figure 5 A 3D scheme of a stack composed by 3 cells connected in series

Typologies of fuel cell

Currently there are many typologies of fuel cells, with different levels of development and commercialization. The most common way of classification is to distinguish them according to the electrolyte material adopted. The type of electrolyte affects the ion transported and, thus, the reactions occurring at the electrodes, the operating temperature and the fuels that can be used. The most popular typologies of fuel cells are:

- Proton Exchange Membrane Fuel Cell (PEMFC)
- Alkaline Fuel Cell (AFC)
- Phosphoric Acid Fuel Cell (PAFC)
- Molten Carbonate Fuel Cell (MCFC)
- Solid Oxide Fuel Cell (SOFC)

In the Table 1, the main features of these typologies of fuel cell are illustrated[5].

	PEMFC	**AFC**	**PAFC**	**MCFC**	**SOFC**
Typical electrolyte	Solid Nafion®	KOH water solution	Concentrated liquid H_3PO_4 in silicon carbide	Molten salts (K_2CO_3)	Solid ceramic
Charge Carrier	H^+	OH^-	H^+	CO_3^{2-}	O^{2-}
Operating Temperature (°C)	60-80	50-230	160-220	600-700	800-1000
Electrical Efficiency (%)	40 -60	60-70	36-45	55-65	55-65
Typical fuel	Hydrogen	Hydrogen	Hydrogen	Methane, Hydrogen	Methane, Hydrogen
Main issues	• High power density • Rapid start-up • High sensitivity to contaminants • Expensive catalyst	• Wide range of operating temperature • Inexpensive catalyst • High sensitivity to contaminants • Pure hydrogen and oxygen required for operation	• Technologically mature and reliable • Good tolerance to contaminants • Low electrical efficiencies • Expensive catalyst	• High electrical efficiencies • High-grade heat • Inexpensive catalyst • Slow start-up • Higher cost of materials • Low power density	• High electrical efficiencies • High-grade heat • Inexpensive catalyst • Fuel flexibility • Slow start-up • Higher cost of materials • Durability issues • High thermal stresses

Table 1 Main features of different typologies of fuel cells

PEMFCs are suitable for many different applications thanks to their great flexibility and modularity, but the most promising field is the transportation, due to their high power density, low operating temperature, fast start-up time and easy handling. Nevertheless, the high cost of the system, especially because of the previous catalyst, is the main obstacle in the economic feasibility of these devices. AFCs work in a very large range of temperatures and can reach very high efficiencies. However, the great sensitivity of their performance on impurities (e.g. CO and CO_2) makes compulsory the utilization of extremely pure hydrogen as fuel, limiting the application in the space. Currently, PAFCs are probably the more commercially-developed and their application is limited to the stationary power production. MCFCs and SOFCs operate at high temperature and this feature allows to reach higher efficiencies and to be couple with CHP systems. The reforming of the fuel occurs internally the systems, widening the fuel flexibility of these devices. The slow start-up and the great stresses caused by thermal cycles make them suitable just for the stationary power production markets. Problems in durability and high costs limits the commercial development of these systems nowadays.

Performances of a fuel cell

The two half reactions (oxidation at the anode and reduction at the cathode), illustrated above, and the resulting charge separation occur even if the circuit is open. In this condition, the reactions are driven in perfect chemical equilibrium and this implies a thermodynamically reversible process. Thus, the system has no losses due to irreversibilities. To introduce the Nernst equation, a very important relationship in the electrochemistry, is necessary to recall some concept from the Thermodynamics, following how this argument is explained by F. O'hayre et al.[8].

Because of its definition and remembering the hypothesis of reversibility of this case, the Gibbs free energy G represents the exploitable energy potential, or work potential, of a system. It is defined by the expression

$$G = U - \left(\frac{dU}{dS}\right)_V S - \left(\frac{dU}{dV}\right)_S V = U - TS + pV = H - TS$$

Where U is the internal energy, S the entropy, H the enthalpy, V the volume and p the pressure of the system. The variation of G (dG) results in the equation

$$dG = dU - T\,dS - S\,dT + p\,dV + V\,dp$$

In the case of the fuel cell, the variation of the Gibbs free energy is negative, as it happens in the case of spontaneous reactions. Nevertheless, the reactants of the reaction must reach the activated complex condition (noted as 2 in Figure 6) with a supply of an amount of energy, called activation energy, before the formation of the hydrogen-oxygen bonds (noted as 3 and 4). To increase the probability of the molecules having enough energy and, in this way, to increase the rate of the reaction, the use of catalysts (e.g. in the case of Proton Exchange Membrane Fuel Cells) or the raise of the operating temperature (e.g. in the case of Solid Oxide Fuel Cells).

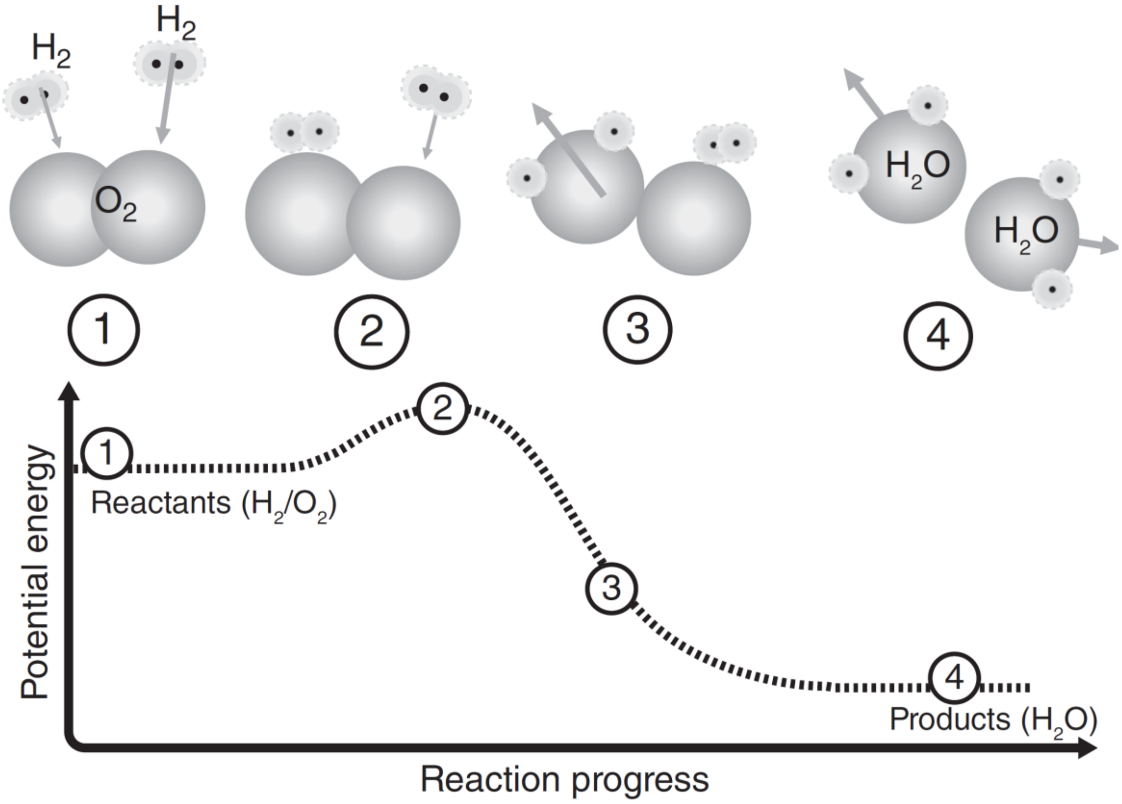

Figure 6 Schematic of the exothermic oxidation of Hydrogen

From the First and Second Law of Thermodynamics, it is possible to express the variation of the internal energy of the system in the case of a reversible transformation as

$$dU = T\,dS - dW = T\,dS - (p\,dV + dW_{el})$$

Where W is the total work and W_{el} the electric work exchange by the system. Including this expression in the previous and considering an isobaric and isothermal transformation (a reasonable hypothesis in the case of fuel cells), the variation of the Gibbs free energy results as

$$dG = -dW_{el}$$

Thus, the maximum electrical work that the electrochemical cell can exchange in reversible transformation at constant pressure and constant temperature is given by the negative variation of the Gibbs free energy occurred in the process.

It is useful to recall the Faraday Law, an electrochemical expression that calculates the total charge Q transferred with electrons in a fuel cell as

$$Q = n\,F$$

Where n is the number of moles of electrons transferred in the reaction and F the Faraday constant (96,485 C/electron-mole), equal to the product between the Avogadro number and the electric charge per mole of electrons.

In this way, defining the maximum electrical work of reversible transformation in open circuit condition as the product of the open circuit voltage OCV and the moving charge Q,

$$W_{el,r} = Q\,E$$

It is possible to determinate the OCV of the cell in function of the variation of the molar Gibbs free energy of the reaction $\Delta\hat{g}_{react}$, as

$$OCV = \frac{W_{el,r}}{\dot{n}_F\,\mathrm{Q}} = \frac{-\Delta\hat{g}_{react}}{z_F\,F}$$

Where $\dot{n}_F$ is the molar flow of the fuel and z_F the charge number of the fuel chemical species. Making explicit the dependence on the temperature and pressure and considering the reactants R and the products P as ideal gas, the open circuit voltage results as

$$OCV = \frac{-\Delta\hat{g}_{react}(T, p_0)}{z_F\,F} + \frac{RT}{z_F\,F}\ln\frac{\prod_{i=1}^{R}\left(\frac{p_i}{p_0}\right)^{\nu_i}}{\prod_{i=1}^{P}\left(\frac{p_i}{p_0}\right)^{\nu_i}}$$

Where $\Delta\hat{g}_{react}(T, p_0)$ is the variation of the Gibbs free energy of formation of the reaction at the temperature T and at the standard pressure p_0, while ν_i the stoichiometric coefficient of each chemical species participating i at the reaction. This expression is the Nernst Equation, one of the most important relationship in the electrochemistry and state that the voltage of the reversible reaction in the fuel cells depends just on the type of the reaction occurring (affecting $\Delta\hat{g}_{react}$) and on the thermodynamic condition (T and p_i) and not, from example, on the dimensions of the cell.

In the case of the oxidation of the hydrogen, the most common fuel for these devices, the OCV is around 1.2 V under 100 °C. Thus, in order to produce enough power for everyday applications from this very low ideal voltage, several cells must be connected in series in a stack. With the increase of the temperature, the OCV tends to decrease, suggesting that the reaction is thermodynamically favoured at lower temperatures.

However, when the electrical current is transferred during the fuel cell operation, the kinetics of the electrochemical reaction must be taken in account. The process is not more ideal and some irreversibilities take place, limiting the rate of the reaction. Since during the electrochemical reaction electrons are either produced or consumed, the current transferred is a direct measure of the rate of the reaction. To normalize the effect of the electrodes surface is useful taking into account the current density instead of the current.

To break the equilibrium between the forward and the backward reaction part of the initial voltage gradient (OCV), which is the driving force of the process, must be spent to lower the activation energy, enhancing the probability of the reactants to be in the activated complex state. This voltage lost in the polarization of the cell is called activation overvoltage η_{act}. It can be calculated from the its relationship with the current density output i described by the Butler-Volmer equation:

$$i = i_0 \left(e^{\left(\frac{\alpha F}{RT} \eta_{act}\right)} - e^{\left(\frac{-(1-\alpha) F}{RT} \eta_{act}\right)} \right)$$

Where the pre-exponential constant i_0 is called the exchange current density and α is the charge transfer coefficient, measuring how symmetric is the change of the activation barrier between the forward and the backward reaction due to the change of electrical potential (for “symmetric” reaction $\alpha = 0.5$). The exchange current density i_0 express the rate constant at perfect equilibrium of the forward and backward reaction and it is a quality parameter for the electrode. In fact, expressing the activation overvoltage in function of the current, it is evident how a higher i_0 determines a lower η_{act}

$$\eta_{act} = \frac{RT}{\alpha F} \sinh^{-1}\left(\frac{i}{2 i_0}\right)$$

Maximizing the exchange current density is possible in four different ways: increasing the reactant concentration, decreasing the activation energy barrier (e.g. adopting a catalyst), increasing the reaction temperature or increasing the active surface of the reaction (e.g. with a nanostructured electrode).

The activation overvoltage takes into account the contribution of both electrodes.

$$\eta_{act} = \eta_{act,an} + \eta_{act,cath} = \frac{RT}{\alpha_{an}F}\sinh^{-1}\left(\frac{i}{2i_{0,an}}\right) + \frac{RT}{\alpha_{cath}F}\sinh^{-1}\left(\frac{i}{2i_{0,cath}}\right)$$

In the case of solid oxide fuel cell, the activation overvoltage of the anode is negligible with respect to that of the cathode, because of the worse kinetics in the reduction of the oxygen (especially at low temperature). For this reason, the focus of the researchers is improving the cathode performance, for example maximizing the number of reaction sites per unit area (TPB).

Another important contribution to the irreversibilities losses occurring during the electrochemical process is given by the intrinsic resistance of the conductor materials of the cell to the flow of the charge species produced by the reaction, ions and electrons, mainly driven by the voltage gradients caused by their accumulation or depletion at the electrodes side, according the device is working in fuel cell mode or in electrolysis mode[8]. This resistance generates a further loss in the voltage of the ideal reaction, called ohmic overvoltage. In fact, the value of the overvoltage follows the Ohm's Law of conduction. The amount of the ohmic overvoltage can be divided in the contributions given by the conduction of ions and of electrons. In these way, the ohmic losses occurring in the cell can be calculated by the following expressions of the Ohm's Law

$$\eta_{ohm} = \eta_{ion} + \eta_{e^-} = \left[\left(\rho_{ion}\frac{L_{ion}}{S_{ion}}\right) + \left(\rho_{e^-}\frac{L_{e^-}}{S_{e^-}}\right)\right] i \cdot S_{cell}$$

where ρ is the resistivity of the material towards the given charged species, L and S are the length and the surface of the components crossed by the given charged species (electrodes, electrolyte and interconnectors). In fact, the ohmic resistance of the cell is a combination of resistances attributed to the different components of the cells, as shown in the schematic cell in Figure 7. The ohmic overvoltage is proportional to the current density by a constant called Area Specific Resistance (ASR), that becomes a quality parameter of the performance of the cell.

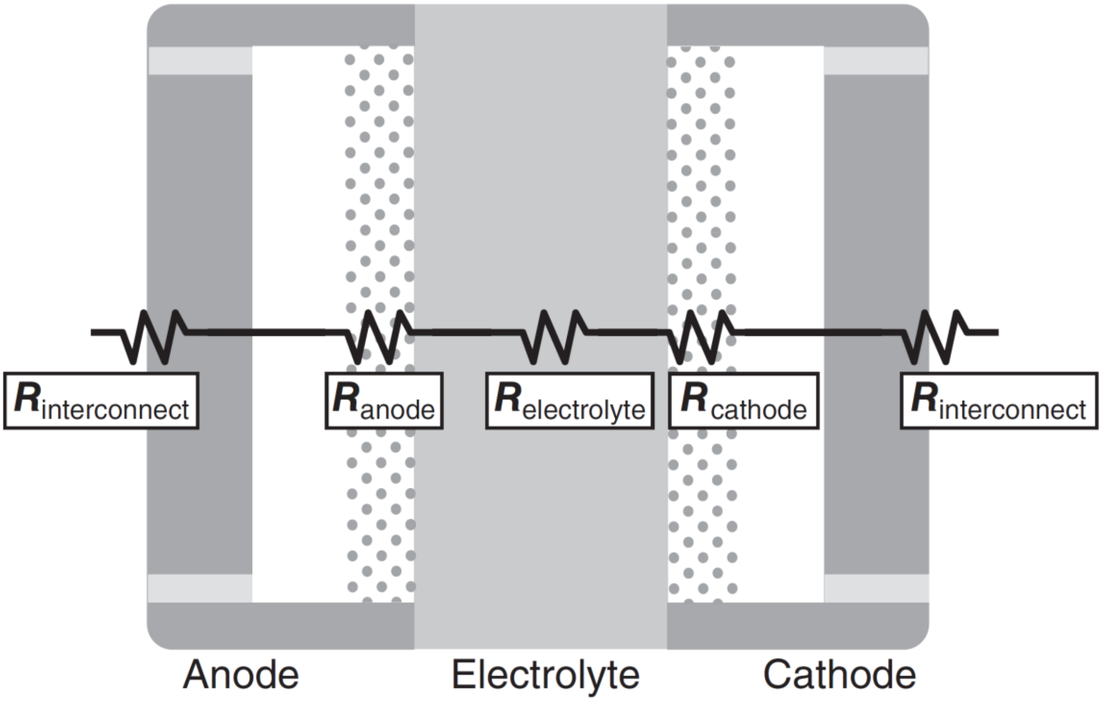

Figure 7 Schematic of the additive resistances attributed to the different components of the cell

In fuel cells characterized by a planar configuration, the length of the pathways of electrons and ions are comparable and, thus, the contributions to the total resistance of the conduction of electrons can be neglected, since usually the ionic conductivity (the reverse of the resistivity) of the electrolyte layer is sensibly lower than the electronic conductivity of the other components. Therefore, in the expression mentioned above, considering the surface of the cell equal to the surface of the electrolyte in this configuration, the ASR is given by the product of the ionic resistivity of the electrolyte and its thickness and is in function of the geometrical characteristic and the charge transport properties of the material and its thermodynamic state (i.e. the operating temperature). In order to decrease this parameter, the researcher focused on fabrication techniques that allows thinner electrolytes layer and on material with high conductivity at reduced temperature. However, also contact resistances associated to the interface between the different layers of the cell must be considered, making the total ohmic resistance difficult to predict and attributed just to the single components.

A further loss in the reversible potential of the cell is the diffusion overvoltage. The molecular diffusion of the reactants through the porous electrodes, a mechanical phenomenon driven by a gradient in the concentration, has a much higher time constant with respect to the charge separation of the gas molecules when one of the electrochemical half-reaction occurs, an electronic phenomenon. In case of high current, and thus a high reaction rate, the concentration of the fuel in the bulk of the electrode drops because of the faster charge separation of the molecules with respect to their diffusion, causing a fuel starvation at the interface between the anode and the electrolyte. This phenomenon causes a sensible drop in the voltage at high current densities. Actually, the limitation due to the diffusion is not a proper overvoltage, but it has a Nernstian effect, reducing the term of the expression of the OCV affected by the concentration of the reactants. It is useful to define as limiting current the theoretical value of the current that causes a null concentration of the fuel in the bulk of the electrode. Adopting the Fick Law as mass transport model to determine the molar flow of the fuel through the electrode and integrating it with the Faraday Law mentioned above, the limiting current i_l can be expressed as

$$i_l = z_F F D_{eff} \frac{C_B}{t_{el}}$$

where D_{eff} is the effective diffusion coefficient of the electrode material, $C_B$is the concentration of the fuel at the outer surface of the electrode and t_{el} the thickness of the electrode. In order to improve the value of the limiting current, maximizing the effective diffusion coefficient, improving the porosity of the electrode or decreasing the its tortuosity or the size of the particles of the material, or minimizing the thickness of the electrode are the most effective solutions.

The value of the diffusion overvoltage can be calculated through the Nernstian expression

$$\eta_{diff} = \left|\frac{RT}{z_F\, F} ln\left(1 - \frac{i}{i_l}\right)\right|$$

Finally, we can express the real output voltage of the cell making explicit the three terms of the overvoltage to subtract to the theoretical thermodynamically predicted OCV as

$$V = OCV - \eta_{act} - \eta_{ohm} - \eta_{diff}$$

The typical polarization curve of a fuel cell is shown in Figure 8[9] and it is possible to observe three different regions of the curve: at low current density there is a quick drop in the potential, dominated by the activation losses; then, the ohmic losses become dominant and the voltage curve is linear as function of the current density; finally, at high current densities, the fuel starvation phenomenon takes place and the voltage response is affected by a quick drop due to the diffusion overvoltage. Usually, in order to maximize the power density of the system, it is favourable to operates at relatively high current densities, just below that causes the voltage drop due to the mass transport problems.

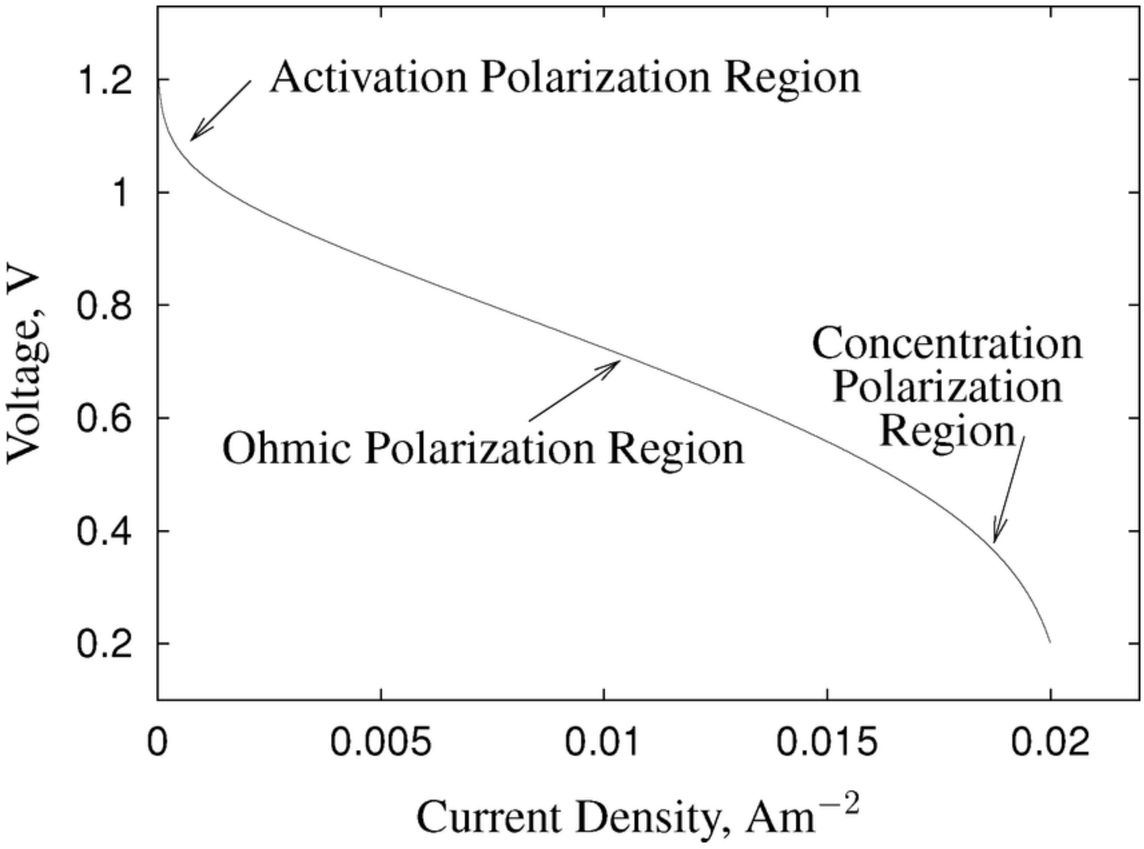

Figure 8 Theoretical polarization curve of a typical fuel cell

Electrolysers and reversible cells

Most of the fuel cells can works in the reversible way: they exploit an electric current to produce fuels and chemicals (e.g.H_2 and CO) starting from the resulting products of their oxidation (e.g. H_2O and CO_2 respectively). In the case of water electrolysis, hydrogen and oxygen are produced separately at the electrode side, producing a potential in the system. An electrolyser needs at least the same electromotive force from an external generator to produce hydrogen in a reversible way. As we have seen in the case of fuel cells, the process is not reversible and the same irreversibilities occurs, causing ohmic, activation and diffusion losses in the voltage, requiring more electrical energy for the reaction. The polarization response of a reversible cell operating in electrolysis mode is not symmetric as compared with the one obtained in fuel cell mode, since the two reactions have different kinetics. The high temperature cells possess higher efficiency (up to 65%) due to the improved kinetics in the reaction.

One of the main problem of these systems is their cost, due in major part to the electricity cost. In fact, nowadays, just a small fraction of the hydrogen commercialized in the world is produced with water electrolysis. However, this technology becomes very attractive when utilized as storage in form of chemicals (hydrogen) for the energy produced by Renewable Energy Sources (RES) (e.g. photovoltaics, wind). The low-cost surplus electrical energy from RES is used to feed the reversible cells and produced hydrogen, that can be easily stored and transported. Then, the electrical demand from the grid is higher than the RES production, the produced hydrogen can be used to feed fuel cells or gas turbine, with a global round-trip efficiency of 30-40%[10]. The hydrogen large-scale storage systems can reach very high volumetric energy density (up to 100 kWh/m^3 if pressurized), becoming a feasible alternative to other storage systems.

The main technical challenges that are requiring lot or R&D efforts are the systems costs, efficiency and reliability. In fact, the phenomenon of degradation due to the delamination of the electrodes is a big issue, especially for the high temperature reversible cells.

THE SOLID OXIDE CELL (SOC)

The main feature of the reversible solid oxide fuel cells is the presence of a solid and tight electrolyte, acting as O^{2-} ion conductor, between two porous electrodes. The materials adopted for the fabrication of the cell need to be ceramic in order to reach higher operating temperatures (from 600°C up to 1000 °C) to guarantee a sufficient high ion conductivity of the solid electrolyte and to improve the kinetics of the electrochemical reactions, since all transport process are enhanced at higher temperature (such as charge transfer, charge conduction, molecular diffusion)[11]. The main effect of the higher reaction kinetic is an improved real efficiency of the device, as highlighted in the previous comparison between the different typologies of fuel cells. Moreover, the improvement in the kinetics allows also to avoid the use of precious catalyst in the fabrication of the electrodes and this fact permits to widen the choice of the fuel also to hydrocarbon fuels (e.g. natural gas or biogas), giving some fuel flexibility to these systems.

Since is the oxygen ion the mobile conductor through the electrolyte, the water is formed at the anode side. Thus, considering pure hydrogen as fuel, the two half reactions occurring at the electrode side are[8]:

at anode side: $H_2 + O^{2-} \leftrightarrow H_2\mathrm{O} + 2e^-$

at cathode side: $\frac{1}{2}O_2 + 2e^- \leftrightarrow O^{2-}$

At the anode side, in case of operation with hydrocarbon fuel, the reduction of carbon monoxide CO occurs:

$$\mathrm{CO} + O^{2-} \leftrightarrow CO_2 + 2e^-$$

Considering only the reduction of the CO as fuel of the cell (neglecting methane CH_4) is accepted in literature since the kinetic of water shift reaction is faster in the reforming reaction of the fuel when water is the oxygen carrier[7]. Thanks to the high operational temperatures of the system, the reforming reaction can occur internally the cell, allowing the direct feeding of the cell with natural gas.

Another important feature is that the heat produced by the irreversibilities of the process is at high temperature, allowing its use to maintain the high operational temperatures, to preheat the inlet flows and to be recovered in a cogeneration configuration of the plant.

The cogeneration can enhance the total plant efficiency up to 90%, starting from an electrical efficiency of SOCF of 50-60%[8].

Nevertheless, the high temperature provides also some disadvantages and challenges to the development of the technology. In fact, the choice of proper materials is complicated by all the issues regarding mechanical, reliability and chemical stability concerns. The materials for the sealing, the interconnectors and the stack hardware capable to perform well at high temperature are expensive and this do not help the SOC technology to be competitive with other traditional energy supply technology.

Furthermore, the ceramic materials of the cell are not suitable to sustain many thermal cycles because of the limited mechanical strains they can stand. This fact, with a relatively slow start-up that characterize these systems, limits the application of SOC technology to the stationery power production with long periods of operation of the plant.

The cost is one of the most challenging issues for this technology. Even if the cost of the materials is reasonable (affecting about 7 USD – 15 USD/kW of the total cost), the fabrication processes of the cells components (e.g. high-temperature sintering or electrochemical vapour deposition) enhance the cost of the cell up to 700 USD/kW, with a total cost of the system of 6000 USD/kW. Different technological development scenarios forecast a decrease of the cost up to 800 USD- 1000 USD/kW, making the solid oxide fuel cell the most economically feasible between the fuel cells[12].

The following list summarizes the advantages and disadvantages of this type of fuel cell:

Pros

- Higher electrical efficiency (50-60%) thanks to the improved kinetics of the reaction.
- Fuel flexibility due to nonprecious catalyst adoption and direct feeding with natural gas thanks to the internal reforming.
- Lower degradation of the performances.
- Higher power density.
- Possibility of cogeneration.

Cons

- Higher cost of the components materials.
- Slower start-up.
- Sealing issues.
- Necessity to minimize the thermal cycle

Description of the components of the SOC

The electrolyte of the solid oxide fuel cells is a high demanding component and it must have many different properties to work properly. It must be a tight component, impermeable to the chemicals flowing in the cells, it must have a good ionic conductivity at the working temperature and a good chemical stability both in oxidizing and reducing environments, and it must have acceptable mechanical properties enough to be very thin, in order to keep low the ionic resistance, and to stand thermal stresses. The Yttria Stabilized Zirconia (YSZ) fulfils all these characteristic and it is the most used electrolyte material in SOFC. The starting zirconium oxide (ZrO_2) is doped with yttrium oxide (Y_2O_3) in a molar ratio in a range of 3-10%, to stabilize its cubic structure at high temperature and to create oxygen vacancy, enhancing the oxygen ion conductivity of the material. The success of YSZ as electrolyte material is due to its excellent chemical stability with the other cell's components, its low cost and toxicity and its high abundance in nature. However, its ionic conductivity drops to low values at temperatures lower than 650 °C, a serious obstacle to the aim of reducing the operating temperature of the fuel cells in order reduce the costs of the materials and simplify the functioning and the heat management. A valid alternative is the gadolinium-dope ceria (GDC) electrolyte, despite the lower chemical stability.

The material of the anode (fuel electrode) must be chemically stable in a reducing environment, a good electronic conductor and characterized by a porosity that allows the flowing of the fuel to the reaction sites at the interface with the electrolyte and of the products of the reaction away from the bulk of the electrode. The metallic nickel is the state-of-the-art material for anodes of SOFCs, but it possesses a much higher thermal expansion coefficient with respect to the YSZ and at high temperature it tends to agglomerate, decreasing the porosity of the cathode. In order to avoid these problems, a porous cermet material has been developed: the nickel particles are enveloped in a YSZ matrix. It inhibits the growth of nickel grains, keeping a proper porous structure of the electrode, makes mechanically compatible the two active layers, improving the adhesion between the anode and the electrolyte. Moreover, this layout allows to extend the active sites of the electrochemical reaction to all the electrode volume.

In the case of planar SOFC, the most popular geometrical configurations are the anode-supported cells and the electrolyte-supported cells. The former allows to reach higher performances, thanks to lower ohmic losses due to the reduced thickness of the electrolyte and lower diffusion losses due to a thinner cathode; the latter guarantees higher robustness to thermal cycles, a good property for systems working in big plants. Figure 9 shows the three most used geometrical configurations of a planar SOFC[13].

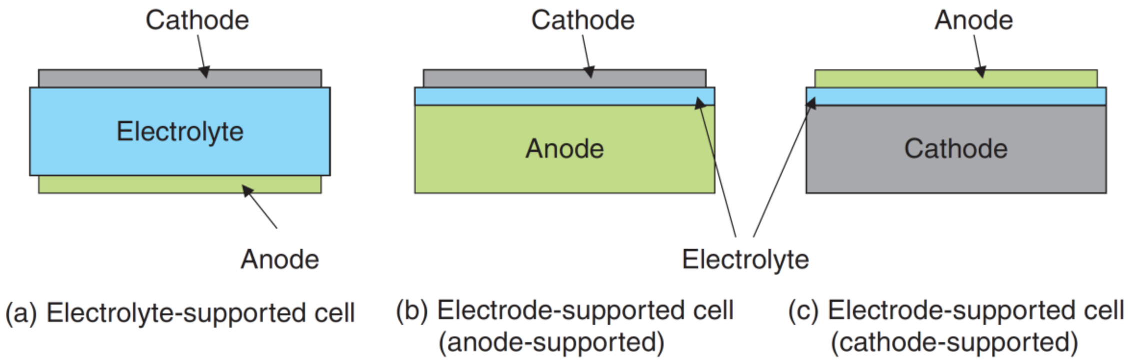

Figure 9 Schematic of the typical geometrical configurations of a SOFC

The cathode

The cathode, also known as air electrode, is the layer of the cell where the oxygen reduction reaction (ORR) takes place, combining electrons from an external circuit with oxygen in gaseous phase (pure or from air) and obtaining oxygen ions, through the following electrochemical reaction

$$O_2 + 2V_O^{\bullet\bullet} + 4e^- = 2O_O^X$$

where, according to the Kröger-Vink notation, $V_O^{\bullet\bullet}$ is an oxygen vacancy site and O_O^X is an oxygen ion on a regular oxygen lattice site in the electrolyte. The equation shows that to fully complete the oxygen reduction reaction, not only the presence of oxygen and electrons are necessary, but also the possibility for the generated products, the oxygen ions, to be transported away from the reaction site into the bulk of the electrolyte[14]. The reaction sites where the gas molecule can diffuse (pore phase) and react with incoming electrons (electronic phase) and the ion generated can migrate to the bulk of the electrolyte (ionic phase), is called Three Phase Boundary (TPB) and is an important feature of the cathode materials. The reaction sites can be limited to the interface between the electrode and the electrolyte if they possess only electronic and ionic conductivity, respectively, (such as LSM and YSZ) or can be extended to the bulk of the electrode if it possesses mixed electronic and ionic conductivity (MIEC) in the case of so-called MIEC materials (such as LSCF or BSCF) or composite cathodes, as shown in the schematic in Figure 10[15].

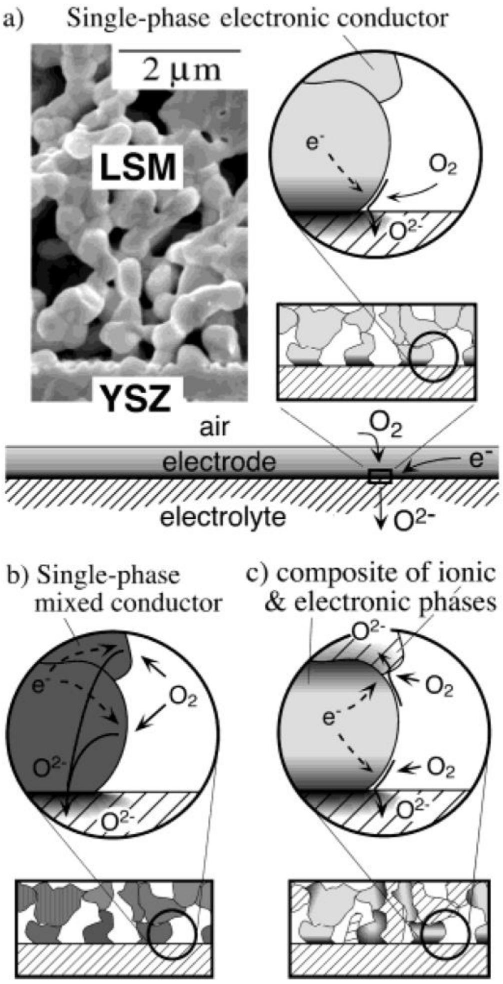

Figure 10 Schematic of the three strategies to create TPB in SOFC cathodes

The oxygen reduction reaction can follow three different pathways[16], showed in Figure 11, depending on the cathode material properties, including several steps in the evolution of the electrochemical reaction:

- The electrode surface path, in which oxygen gas diffuses in the cathode lattice and is adsorbed on the electrode surface and then diffused along the surface (possibly dissociated or partly ionized) towards the cathode/electrolyte surface where the complete ionization and the ionic transfer into the electrolyte occur.
- The bulk path, in which after the gas diffusion and the adsorption on the cathode surface, the oxygen is dissociated, ionized and incorporated in the cathode bulk and is transported and transferred into the electrolyte. This path is favoured in material characterized by high ionic conductivity.
- The electrolyte surface path, in which the adsorption of the oxygen occurs on the electrolyte surface and the ionization occurs due to the electrons coming from the electrode. Hence, due to the very low electronic conductivity of the electrolyte material, the active zone of this path is restricted to the region close to the TPB.

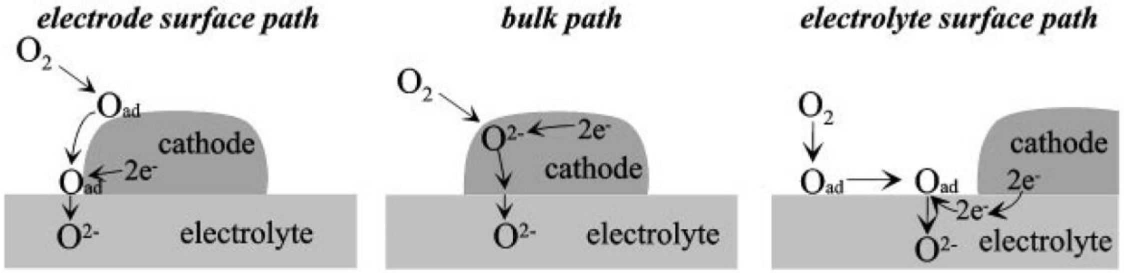

Figure 11 Schematic of the three possible reactions paths of ORR

The oxygen reduction reaction can simultaneously occur through the three pathways, and for each of them one or more elementary step of the reaction can determine the rate of the reaction. In order to optimize the cathode performance, it is very important to determine the rate-determining step of the reaction, depending not only to the material adopted, but also to the geometrical parameters of the cathode and operating thermodynamic conditions. In Table 2[17], the main possible reaction steps of ORR are ranked (in the case of poor ion conducting materials, the bulk transport of ions can be neglected).

Rank	**Reaction Step**
1	Diffusion of O_2 molecules in gas phase to the porous electrode
2	Adsorption of O_2 on the surface of the electrode
3	Dissociation of molecular into atomic oxygen species
4	Charge transfer from the electrode to the oxygen species before or after dissociation
5	Incorporation of oxide ions into vacancies in the crystal lattice of the electrode
6	Bulk transport of O^{2-} ions through the electrode to the electrode/electrolyte interface
7	Transfer of O^{2-} ions across the electrode/electrolyte interface

Table 2 Elementary reaction steps of the oxygen reduction reaction in the cathode

Steps from 2 to 5 are surface-related steps, while step 6 is related to the bulk diffusion of the electrode. These two phenomena can be quantitatively expressed with two properties of the materials: the former with *k*, the oxygen surface exchange rate constant; the latter with *D*, the oxygen bulk diffusion rate.

On summary, a cathode material suitable for the operation in a solid oxide fuel cell should possess the following main features:

- High electronic conductivity, to transport the electrons to the reaction sites.
- Sufficient porosity to permit a fast diffusion of the gas towards the reaction sites.
- Chemical stability in a highly oxidising environment during fabrication as well as operation. For this reason, semiconducting oxides have been adopted instead of base metals, excluding noble metals (such as platinum) because of their cost.

- A thermal expansion coefficient (TEC) compatible the one of the other components of the cell, to minimize the structural stresses caused by the thermal expansion during the operation.
- A good chemical compatibility with electrolyte and interconnector materials.
- High catalytic activity during ORR.
- Cost effective.

Table 3[18] compares the main properties at low temperatures of the three cathode materials analysed in this study. In this range of temperature, the MIEC material BSCF shows the best surface exchange and bulk diffusion properties, with values greater with orders of magnitude as compared with LSM and LSCF. However, the poor electronic conductivity and the great thermal expansion coefficient as compared to the one possessed by YSZ (around 10.3 x 10^{-6})[19] are still big issues to the choice of this material as cathode. A more detailed description of these materials continues in the following paragraphs.

Composition	TEC (K^{-1})	σ ($S\ cm^{-1}$)	D ($cm^2\ s^{-1}$)	k ($cm\ s^{-1}$)
		500–750 °C	600 °C	600 °C
$La_{0.8}Sr_{0.2}MnO_{3-\delta}$ (LSM)	12.0×10^{-6}	120–130	5.2×10^{-18}	1.5×10^{-11}
$La_{0.6}Sr_{0.4}Co_{0.2}Fe_{0.8}O_{3-\delta}$ (LSCF)	15.3×10^{-6}	300–330	1.7×10^{-10}	1.1×10^{-7}
$Ba_{0.5}Sr_{0.5}Co_{0.8}Fe_{0.2}O_{3-\delta}$ (BSCF)	24×10^{-6}	30–35	3.3×10^{-7}	1.4×10^{-5}

Table 3 Main properties of LSM, LSCF and BSCF materials for cathode in SOFC

LSM

One of the most popular and studied cathode material is the strontium-substituted lanthanum manganite ($La_{1-x}Sr_xMnO_3$), since its first application in 1973. Before the diffusion in the application of this material, the cathodes were mostly made by porous platinum electrode since the beginning of the XX century. The oxygen reduction reaction in this kind of cathodes is largely dependent on the active area at and close to TPB. The intent to extend the size of the active region, in order to improve the oxygen reduction kinetics at lower temperatures, and to minimize the cost avoiding the use of a precious metal brought the researchers to investigate the applicability of transition metal oxides (i.e. perovskites) as SOFC cathodes since the middle of the ‘60ies. These material, in facts, show good catalytic properties for ORR, chemical and thermal stability and good electronic and ionic conductivity.

The Sr-doped $LaMnO_3$ (LSM) is a p-type conductor and belongs to the ABO_3 perovskite oxide family, whom crystal structure is shown in the Figure 12.

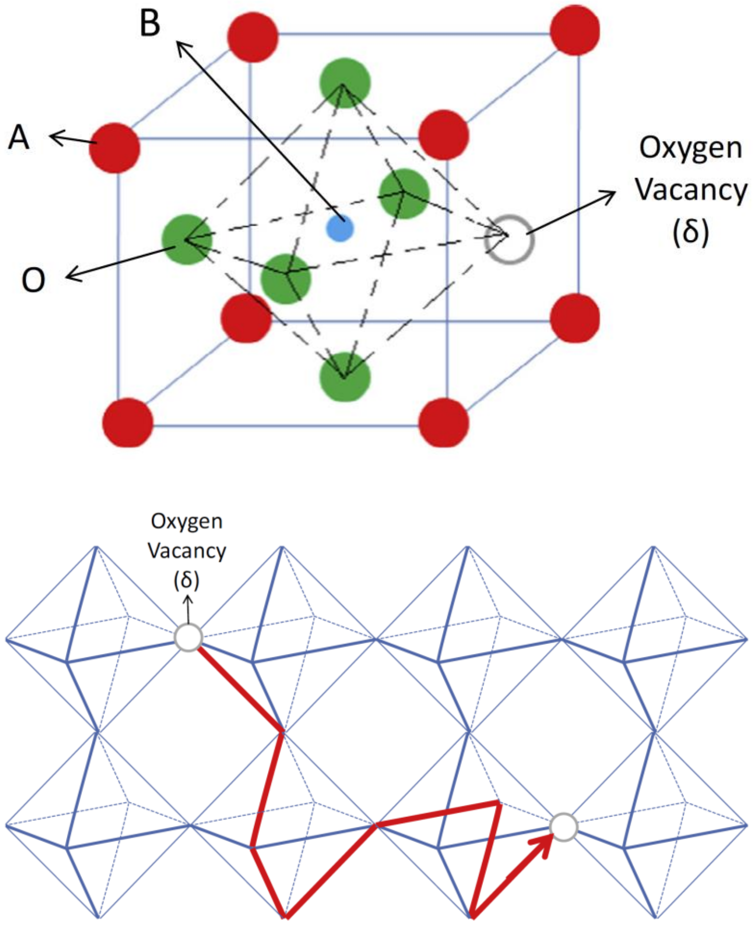

Figure 12 Oxygen deficient perovskite structure and diffusion of oxygen vacancies through the structure

The 12 coordinated A-site positions are occupied by rare and alkaline earths metals (such as La and Sr) cation, the lower valence cations with larger ionic radius, while the octahedral B-site cations are transition metal ions (in this case Mn), higher valence cation with lower ionic radius. The crystal structure of the stoichiometric lanthanum manganite $LaMnO_3$ is orthorhombic at ambient temperature and becomes rhombohedral at 600 °C. The substitution of lanthanum ions La^{3+} with strontium ions Sr^{2+} decreases this transition temperature because of the increasing of the concentration of Mn^{4+} due to the oxidation of Mn^{3+} to keep the electrical neutrality. The so-formed electric hole produce a sensible enhancement in the electrical conductivity and catalytic activity of the base material, the lanthanum manganite. Increasing the amount of Sr doping causes an improvement in the electrical conductivity of $LaMnO_3$ up to doping value of $x= 0.5$. However, that would increase the thermal expansion coefficient as well, causing mechanical stresses with other components during the thermal cycles. Doping values in the range of $x=\sim 0.1 - 0.2$ provides high electronic conductivity and, at the same time, maintains mechanical and chemical stability with YSZ[19].

In Figure 12 the oxygen vacancies δ are shown as well. In fact, lanthanum manganite can present both oxygen-excess and oxygen deficient nonstoichiometries and is generally denoted by $La_{1-x}Sr_xMnO_{3\pm\delta}$. Nevertheless, LSM is in usually oxygen-excess nonstoichiometry form under normal fuel cell condition, becoming oxygen deficient at very low partial pressure of oxygen. The nonstoichiometry of the material is caused by the cation vacancies on both La and Mn sites. This feature is very important in determining the behaviour of the cathode because it has been demonstrated in literature that higher vacancies concentration leads to faster ion transport and surface exchange, improving in this way the its performances. In fact, the more the vacancies there are, the faster the oxygen is absorbed and can move through the lattice, as shown in Figure 12. For these reason tailored LSM cathodes with A-site nonstoichiometric composition (e.g. A/B = 0.9) is preferred in the choice of the cathode material.

The main reason of the success of LSM as cathode material is the good electronic conductivity (300 S cm^{-1} at 900°C for $La_{0.8}Sr_{0.2}MnO_3$)[20], the high stability with YSZ electrolyte (up to 1200 °C), the high electrochemical activity for O2 reduction at high temperatures and compatible thermal expansion coefficient with respect to the one of the other components of the stack.

On the other hand, the main issues in the use of LSM as cathode material at reduced SOFC operating temperatures (<800 °C) are the high activation energy of the O_2 reduction reaction and the poor ionic conductivity, as already mentioned in Table 3, that cause the very high polarization losses of this cathode. This latter characteristic emphasizes the importance of the three-phase boundary in this kind of cathode and, therefore, of the interface, even if a parallel bulk transport path near the TPB in LSM has been suggested, especially at moderate to high overpotential[15].

LSCF

The work made by the researchers in looking for a good cathode for SOFCs during the years has brought to the synthesis of mixed ionic-electronic conductor (MIEC) single-phase porous oxides. Thanks to their properties explicated in their name, it is possible for the oxygen diffused in the pores of the cathode to be reduced at the surface of the electrode and transported through the bulk of the material towards the electrolyte/ cathode interface. If the bulk transportation become the dominating path, the active region for oxygen reduction reaction is extended through the bulk of the electrode[21], catalysing and improving the kinetics of the reaction at lower temperatures (<800 °C)[22].

For these reasons, in MIEC material the oxygen reduction reaction can be subdivided in the following steps, shown in Figure 13[21] that underlines how all the bulk of the electrode is involved in the electrochemical reaction:

a) Motion of the ionic defects in the electrolyte as pure migration, driven by the electrostatic potential
b) Electrochemical reaction occurring at the triple phase boundary at the electrode/electrolyte interface (TPB1)
c) Transfer of ionic defects, the oxygen vacancy, across the interface
d) Transport of ionic and electronic defects in the solid phase of the porous electrode
e) Transport of the oxygen gas in the pores of the electrode through diffusion and convection
f) Electrochemical reaction at the MIEC/gas interface
g) Electrochemical reaction occurring at the triple phase boundary at the current collector/electrode interface (TPB2)
h) Transfer of electrons at the current collector/electrode interface.

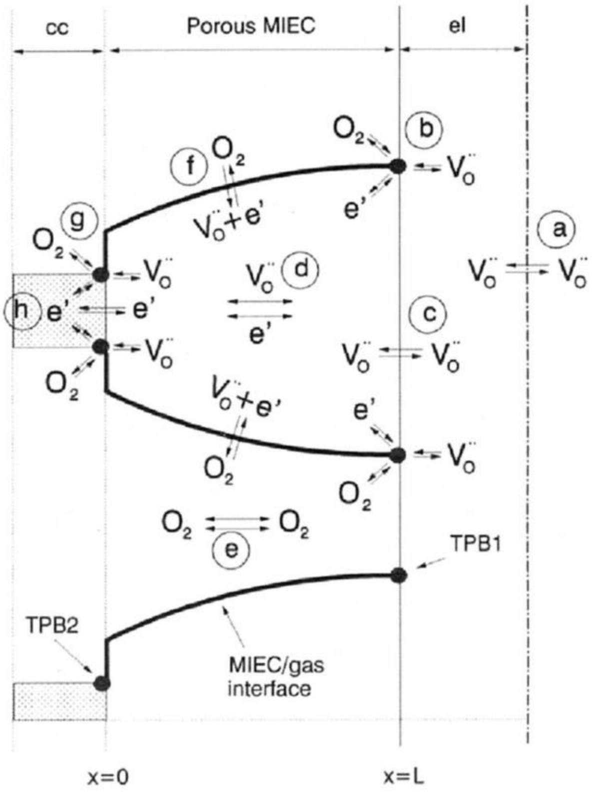

Figure 13 Schematic diagram showing the elementary steps in a MIEC material

The mixed ionic-electronic conductor materials that have gained more interest in the past years are the cobaltite-base perovskites (CBPs), such as $La_{0.6}Sr_{0.4}Co_{0.2}Fe_{0.8}O_{3-\delta}$ (LSCF) and $Ba_{0.5}Sr_{0.5}Co_{0.8}Fe_{0.2}O_{3-\delta}$ (BSCF), thanks to their excellent electrocatalytic activity for the oxygen reduction reaction.

Lanthanum strontium cobaltite ferrite (LSCF) shows very good electronic conductivity (230 S cm^{-1} at 900 °C)[20], comparable to the one possessed by LSM. Its structure is characterized by enhanced lattice oxygen vacancy formation thanks to the doping of the initial $LaCoO_3$. This high concentration of oxygen vacancies possesses relatively high mobility and, for this reason, LSCF exhibit a very high oxygen ion conductivity[14].

However, there are some issues that has slowed the diffusion of the application of this material as cathode for SOFCs. The most important is its high chemical activity with YSZ during the high temperature sintering, forming an insulating reaction phases such as $La_2Zr_2O_7$ and/or $SrZrO_3$ that causes a degradation in the performances of the cell, and for this reason LSCF cannot be directly applied on YSZ electrolyte. Thus, in order to avoid the detrimental interfacial reaction, a doped ceria (e.g. Gd-doped ceria GDC) barrier layer can be applied at the interface between the cathode and the electrolyte to prevent they get in direct contact[23]. However, this solution requires additional screen printing and sintering steps in the fabrication of the cell, increasing costs and complexity of the device, and increases the risk of degradation and delamination of the cell due to the incompatibility in the chemical and thermal properties between the electrolyte and the ceria layer.

In the past few years the researches made by Jiang et al. [24,25] showed that good cathode performances can be obtained from the direct application of the LSCF cathode on the electrolyte adopting the in situ approach, explained in detail further, and avoiding the additional fabrication steps and their issues mentioned above. This method prevents also a possible delamination between the cathode and the GDC layer due to sensibly different thermal expansion coefficients, 15.3 x 10^{-6} K^{-1} and 11.5 to 11.9 x 10^{-6} K^{-1} at 700 °C respectively for LSCF and GDC.

Further solutions to the high chemical activity between LSCF and YSZ are the adoption of Sr-free cobaltite perovskites (such as double perovskite oxides) or stabilizing the structure through doping (e.g. through Nb doping) in the B sites[26].

BSCF

One of the most promising mixed ionic-electronic conductor material suitable for the application in IT-SOFCs is $Ba_{0.5}Sr_{0.5}Co_{0.8}Fe_{0.2}O_{3-\delta}$ (BSCF). It possesses a cubic perovskite structure that can be obtained through combined citrate-EDTA method, calcining the BSCF gel at temperatures above 850 °C[27]. The A-site position in the structure is occupied by an alkaline-earth specie cation, rather than a rare-earth element, as in the classic material used as cathode in SOFCs.

BSCF cathodes showed excellent electrochemical performances, sensibly better than the typical cathode materials[28], especially in a range temperature between 500 – 600 °C. They can be explained by the high oxygen diffusion properties that BSCF possesses: its oxygen vacancy diffusion rate is higher by many orders of magnitude with respect to LSCF and LSM (1.3×10^{-4} cm^2 s^{-1} at 900 °C). This high value is caused by the high concentration of oxygen vacancies, formed as a result of the A-site doping to maintain the charge neutrality. This compensation mechanism is preferred in BSCF with respect the one consisting in the conversion of B-site ions to a higher valence state, as it happens in the case of LSCF[29].

In order to operate in a range of temperatures below 700 °C, the typical YSZ must be replaced with electrolyte materials that can provide a satisfactory ionic conductivity at relatively low temperature, such as doped ceria electrolyte (GDC or SDC)[28]. However, the diffused application of BSCF as cathode material must face some critical drawbacks: the high thermal expansion coefficient ($\sim 24 \times 10^{-6}$ K^{-1}), causing delamination problem with the electrolyte, and the low electronic conductivity (~25 S cm^{-1} at 800 °C), leading to significant contact resistance between the current collector and the electrode[30]. Moreover the presence of CO_2 in air deteriorates the cathode performances by absorbing on the BSCF surface and thus obstructing the oxygen surface exchange reaction[31]. Finally BSCF showed low thermal stability at reduced temperatures (<850 °C) with a phase transformation from cubic to a mixture of cubic and hexagonal phases, resulting in the degradation of electrochemical performances of the material[32].

Composite cathodes

It has been explained that reducing the operating temperature would cause a sensible decrease of the performances of the cathode, especially LSM due to its high activation energy and slow reaction kinetics for the oxygen reduction reaction[14]. These properties emphasize the importance of the length of the triple phase boundary in the behaviour of the cathode performances. The addition of an ion conducting material in the bulk of the electrode to form a well-tailored nanostructured composite cathode would improve this length, extending the TPBs from the cathode/electrolyte interface to the 3D porous cathode bulk, enhancing the effective reaction area[33], as already depicted in Figure 10.

The bismuth based oxides, such as erbium stabilized bismuth (ESB), have gained a lot of attention in the last years as material to incorporate in composite cathodes because they possess very high ionic conductivity and excellent surface exchange properties, as compared with other ionic conducting material such as YSZ and GDC (Figure 14)[34]. However, the application of ESB as an electrolyte for SOFCs has been limited due to its low melting temperature, high reactivity and instability under reducing fuel environment.

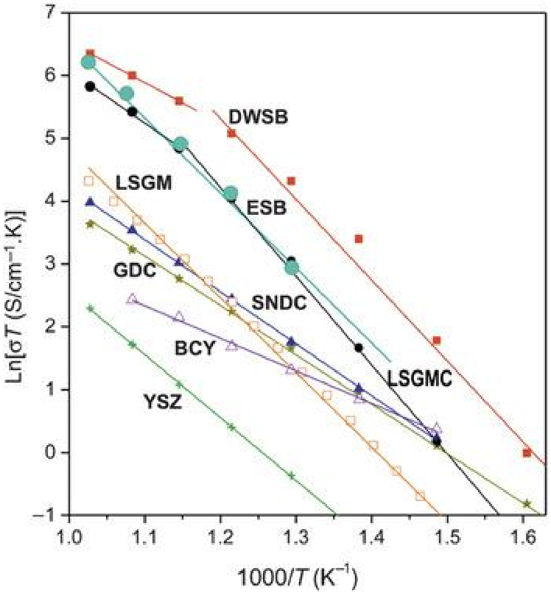

Figure 14 Ionic conductivity as function of the temperature of different solid oxide electrolytes

Since the two major rate-limiting step for the oxygen reduction reaction are the dissociated adsorption and the oxygen incorporation[35], the design of a nanostructured composite LSM-ESB cathode would improve the performance of a pristine LSM cathode, thanks to the integration of the excellent dissociative adsorption property of LSM surface with the superior oxygen incorporation and high conductivity of the stabilized bismuth oxide[36].

In situ approach: electrochemically induced electrode/electrolyte interface

As explained above, especially for a poor ion conducting material as LSM, the three phase boundaries (TPB) and thus the cathode/electrolyte interface play a critical role in the electrocatalytic activity for the oxygen reduction reaction in the SOFC. In fact, the formation of TPB at the interface provides a direct pathway for the oxygen ion migration, facilitating the electrochemical process. Thus, the performance and durability of these devices depend strongly on the microstructure of the interface.

The state of the art in the electrode fabrication process consists in the high temperature sintering (>1000 °C, according to the cathode material) of the screen-printed cathode ink on the electrolyte layer. The effective electrode/electrolyte interface is given by the intimate contact between the cathode particles and the electrolyte layer through nano-sized contact convex rings, formed during the high temperature sintering fabrication step. These contact rings are formed due to the cation interdiffusion between the cathode and electrolyte materials. The cation diffusion towards the edge of the contact convex rings, that become the TPB, occurs to reduce the free surface energy of the interface[37]. Moreover, some morphology and topography changes of the contact convex have been observed rings during the polarization, especially for the materials characterized by an ORR occurring predominantly at the TPB. This phenomenon is caused by the cation interdiffusion and the incorporation of oxygen occurring during the polarization. In the case of LSM, the higher concentration of manganese in the convex rings as compared to the flat boundary provides a short diffusion paths for the oxygen species[38].

Knowing the morphology change of the cathode during oxygen reduction reaction, Jiang et al. developed a new *in situ* fabrication method for the cathode: a proper electrode/electrolyte interface is electrochemically induced during the cathodic polarization of the cell, avoiding the high sintering fabrication step[24,25,39–43]. Before the polarization the electrolyte surface is clean, since the interface cannot be induced at the temperature of operation of the cell. The oxygen activity at the contact points produces nano-sized contact marks or clusters on the electrolyte surface that form an effective electrode/electrolyte interface. These marks are formed due to the mechanism of the incorporation of oxygen and cation interdiffusion between the electrode and the electrolyte[38]. The formation of the interface depends on the polarization, with an increased number and density of the marks with the increase of the current density. The contact marks are smaller as compared with the convex rings formed during the sintering because of the smaller non-sintered particles of the *in situ* cathode. Providing more contact points, the *in situ* assembled cathode showed electrocatalytic performances similar to the pre-sintered cathode, despite the relatively poor contacts between cathode particles and YSZ electrolytes[39]. A graphical representation of the interface, of the contact convex rings and the contact marks formed during the high sintering step and the cathodic polarization is shown in Figure 15.

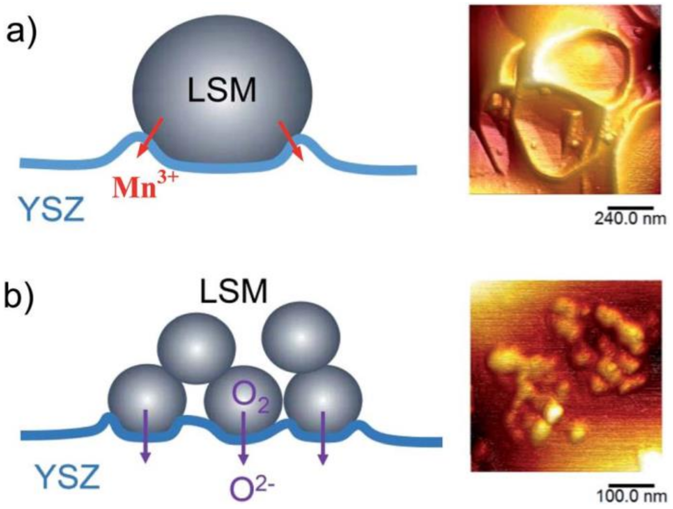

Figure 15 Scheme of the LSM electrode/YSZ electrolyte interface formation under the influence of (a) high temperature sintering, e.g., 1150 °C and (b) cathodic polarization at normal SOFC operation conditions, e.g. 800 °C.

It is important to note that the interface formation is very much dependent on the nature of the electrode materials: for example, in the case of LSCF electrode the contact cluster are much smaller because the ORR is extended in all the cathode bulk, due to the MIEC properties of the material, and thus the driving force for the oxygen incorporation and the cation interdiffusion at the interface is much smaller as compared to LSM. Despite the very different morphology of the interface between the pre-sintered and the *in situ* assembled cathode, the reaction mechanism for the ORR are almost identical, with very close activation energy for the reaction in the two cases (e.g. for LSM 150-171 kJ mol^{-1} and 170-199 kJ mol^{-1} respectively for *in situ* and pre-sintered cathode)[39].

In addition to the formation of an intimate contact and adhesion between the electrolyte and the cathode, the cathodic polarization flowing in the electrode is also responsible with the same phenomenon of the cation interdiffusion of the improved inner contact between the different particles of a composite cathode, causing the improvement of the cathode performances that in some cases can be seen during the polarization[42]. A schematic of the direct applied cathode and the formation of the interface and the self-assembly of the electrode is shown in Figure 16.

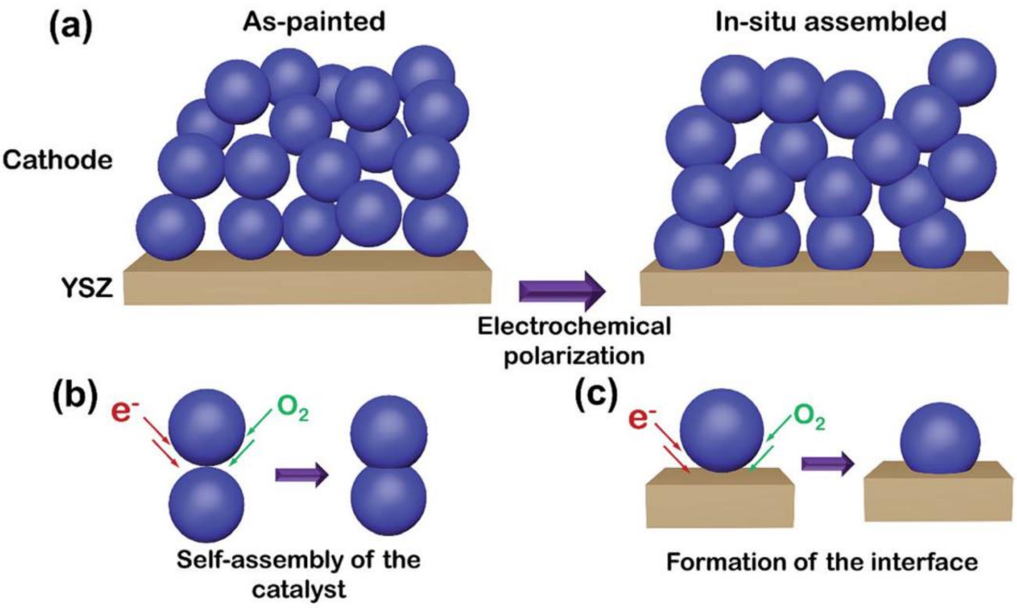

Figure 16 Scheme of the in situ cathode application *process*

Characterized by very similar performances as compared to the pre-sintered cathode, the *in situ* approach simplifies the fabrication steps, avoiding the high energy consumption of the high temperature sintering steps. Moreover, for this reason in the case of CBP cathodes, as mentioned above, it is possible to avoid the adoption of a doped ceria layer because the $La_2Zr_2O_7$ and $SrZrO_3$ insulating reaction phases does not occur without the high temperature sintering steps, as highlighted in Figure 17.

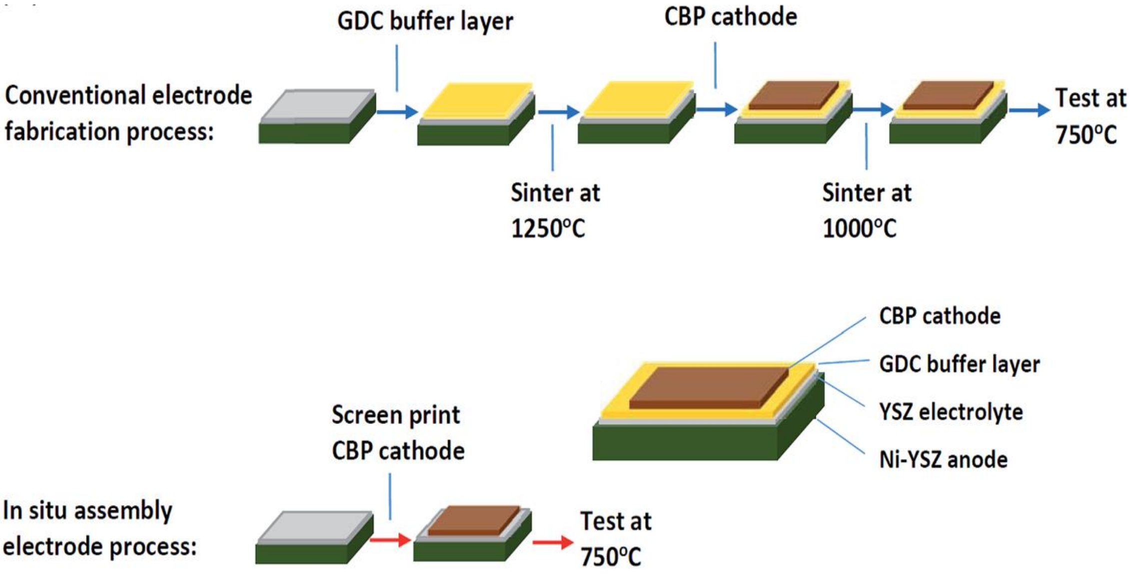

Figure 17 Fabrication steps for cells with a conventionally high temperature sintered LSCF and GDC interlayer process and with in situ assembled LSCF electrode

EXPERIMENTAL

Fabrication of the YSZ-supported half-cell and in Situ assembled cathode

The behaviour of the different composite cathodes has been studied adopting a half-cell configuration with a three-electrode set up during the electrochemical tests. The half-cell configuration consists in a dense YSZ layer upon which the composite cathode is applied with a screen printing technique. The cathode forms the proper interface with the electrolyte during the polarization, avoiding the sintering step, as expected by the in-situ assembly approach. Before the preparation of the cathode, on the other side of the electrolyte a platinum counter electrode and a platinum reference electrode were applied with the same method. The counter electrode, painted in correspondence of the cathode, closes the electrical circuit with the cathode, while the reference electrode, painted as an external ring on the edge of the electrolyte, is necessary as a 0 V reference for the measurement of the cathode overpotential. The distance between the reference and the current electrode was at least of 4 mm, while the surface of the counter electrode was of 0.5 cm^2. The schematic and the explained behaviour of the half-cell three electrode configuration is shown in Figure 18.

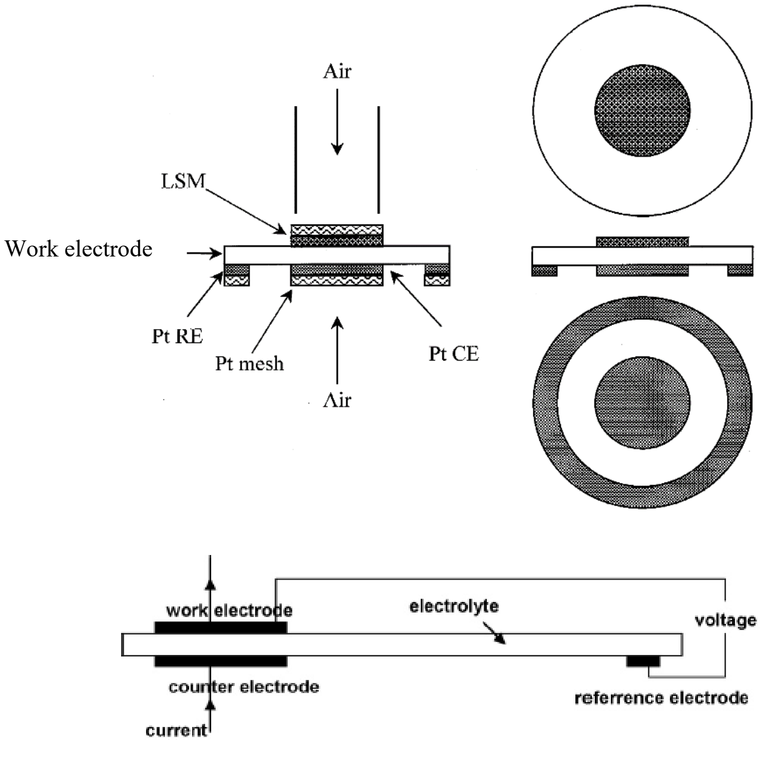

Figure 18 Schematic and behaviour of the three-electrode setup of the YSZ electrolyte supported half-cell

Each yttria-stabilized zirconia electrolyte disc is obtained pressing 1.50 g of 8 mol % Y_2O_3-ZrO_2 powders (C.I. CERAMICS PTY. LTD) in a mould by a pressing machine at 4 MPa for at least 30 seconds. The pressed samples are sintered in air at 1450 °C for 5 hours in a furnace. After being cooled down, the platinum electrodes were painted on a side of the electrolyte and, after that, the cell was sintered in air for 2 hours at 1100°C.

The ESB and BSCF powders were synthesized using the sol-gel method. This process consists in the settling of the nanosized particles from a colloidal suspension onto a pre-existing surface, resulting in a ceramic material. The desired solid particles are suspended in a liquid, forming the 'sol'. The particles in the sol are polymerised by partial evaporation of the solvent, or addition of an initiator, forming the 'gel', which is then heated at high temperature to give the final solid product[44]. The porosity and the particle size can be controlled by process conditions like the precursor concentration, the solvent adopted and the processing temperature[23]. The starting chemicals for $Er_{0.4}Bi_{1.6}O_3$ (ESB) were erbium nitrate pentahydrate $Er(NO_3)_3 \cdot 5H_2O$ (99.9%, Sigma-Aldrich Pty. Ltd) and bismuth nitrate pentahydrate $Bi(NO_3)_3 \cdot 5H_2O$ (>=98%, Sigma-Aldrich Pty. Ltd), while for $Ba_{0.5}Sr_{0.5}Co_{0.8}Fe_{0.2}O_3$ (BSCF) they were barium nitrate $Ba(NO_3)_2$ (>=99%, Alfa Aesar), strontium nitrate $Sr(NO_3)_2$ (99%, CHEM-SUPPLY PTY LTD), cobalt nitrate hexahydrate $Co(NO_3)_2 \cdot 6H_2O$ (>=98%, Alfa Aesar) and iron nitrate nonahydrate $Fe(NO_3)_3 \cdot 9H_2O$ (>=98%, Sigma-Aldrich). The metal nitrates that compose the final cathode powder were mixed with the proper amount of citric acid, Ethylenediaminetetraacetic acid (EDTA) and ammonia solution and then diluted with deionized water. The molar ratio of metal ions mole in ESB or BSCF formula, EDTA (Sigma-Aldrich) and citric acid (Sigma-Aldrich) were 1:1:1.5, while 60 ml of ammonia solution (28% concentration, MERCK PTY LIMITED) for each 0.1 metal ions mole were required. The obtained solution was heated and stirred until a dark gel were formed after the evaporation of the water and ammonia. The heating process was extended until the gel was completely burnt and became ash. The ash was therefore calcinated in air at 800 °C for 2 hours in the case of ESB powder, while the preparation of BSCF powder required a calcination at 1100°C for 4 hours. The formation of perovskite phases for the BSCF powder was examined through X-ray diffraction analysis. The sol-gel method permits to obtain a powder with enhanced porosity and characterized by an effective microcrystalline structure adopting a relatively simple preparation.

The so crystallized ESB powder were mixed with the electronic conductor material (LSM, LSCF and BSCF) by mechanical mixing in a mortar to obtain the composite material for the cathode fabrication. The weight ratio was 1:1 in all the cases (ESB-LSM, ESB-LSCF and ESB-BSCF composite cathode).

The synthesis of the ESB decorated LSM cathode power were performed via the gelation method: the ESB aqueous precursor solution was prepared as mentioned above, heated and stirred on the magnetic stirrer; when the solution started to become a gel, the industrial LSM powder was added at the solution and the mixture were completely stirred and dried until the formation of a dark ash. The obtained powder was calcined in air at 650 °C for 2 hours. The fabrication process of the *in situ* ESB decorated LSM cathode is summarized in Figure 19. The same method has been adopted for the preparation of the ESB decorated BSCF cathode.

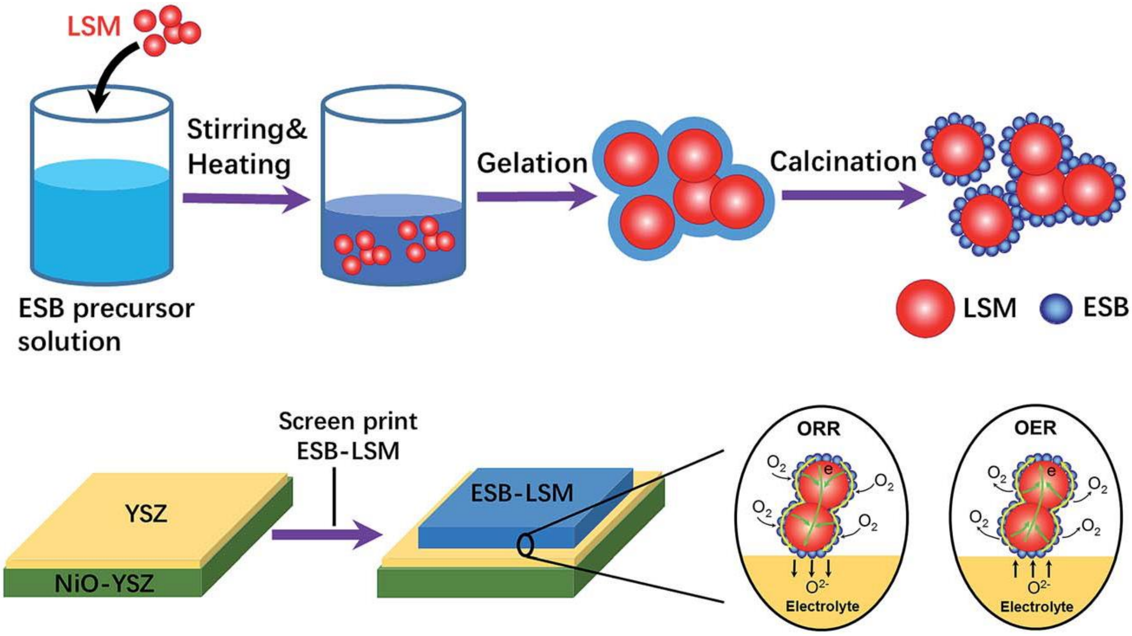

Figure 19 Schematic of the synthesis of nanostructured ESB decorated LSM powder via the gelation process and in situ direct assembly of the ESB-LSM electrode in a Ni-YSZ anode supported YSZ electrolyte cell

The different cathode pastes were obtained mixing the composite powders with an ink vehicle (NEXTECH MATERIALS LTD) in a mortar at a weight ratio of 7:3 for at least 45 minutes, until a homogeneous paste was formed. The cathode pastes were, then, screen-printed on the electrolyte and dried in a hoven for 2 hours at 150 °C. The surface of the cathode in contact with the electrolyte interface was 0.5 cm^2.

A further layer of the respective electronic conductor material (LSM, LSCF or BSCF dispersed in the ink vehicle adopting the same method explained above) was painted on the cathode as current collector. The objective of the current collector was to obtain, thanks to its excellent electronic conductivity, a homogeneous distribution of the electrical current, received by the external circuit and collected by the platinum mesh, in the porous composite cathode. The adoption of excellent electronic conductors, such as platinum, as current collector had been avoided after few tests. In fact, this cathode setup determined a relevant degradation in the performances of the cathode during the polarization, probably because the diffusion of the platinum particles in the bulk of the porous cathode during the operation of the cell inhibited the oxygen reduction reaction due to the platinum poor electrocatalytic properties for the oxygen reduction reaction.

Before being ready for the electrochemical testing, the as-prepared cells were dried in air at 150 °C for 2 hours.

The electrochemical test

The cells to be tested were placed in a furnace (OTF-1200 X by MTI Corporation): the air flows required to feed the working and the counter electrodes were provided by two different alumina tubes, upon which an external circuit linked the cell to the testing potentiostat (Gamry Reference 3000 Potentiostat). The connection between the external circuit and the three electrodes were guaranteed by three platinum grids. The cell was heated to 700 °C with a heating rate of 5 K/min.

Five different test conditions were chosen for each type of composite cathode:

- 12-hour cathodic polarization at constant 250 mA cm^{-2} current density;
- 12-hour cathodic polarization at constant 500 mA cm^{-2} current density;
- 12-hour anodic polarization at constant 250 mA cm^{-2} current density;
- 12-hour anodic polarization at constant 500 mA cm^{-2} current density;
- 12-hour open circuit condition.

The cathodic polarization of the electrode is the current flowing in the cell under the SOFC operation condition, while the anodic polarization is the one during the SOEC operation condition. The electrochemical impedance curves were measured before the polarization, after 30 minutes, 1 hour, 2 hours, 4 hours and 12 hours of polarization. These impedance spectra were measured over a frequency range of 100 kHz – 0.1 Hz with a signal amplitude of 10 mV under open circuit. From the Nyquist plot it is possible to evaluate the ohmic resistance R_Ω of the cell, as high-frequency intercept of the spectra with the real axis, and the overall electrode polarization resistance R_p, as the difference between the low-frequency and the high-frequency intercepts. R_Ω is comprehensive of the resistances caused by the YSZ electrolyte, the cathode and the contact between the two.

Microscopic characterization

The as-synthesized ESB powder were mixed with LSM, LSCF and BSCF respectively through mechanical mixing in a mortar in a weight ratio of 1:1 and the mixtures were heated in air for 2 hours at 700 °C, 750 °C, 800 °C and 850 °C in order to determine the thermo-compatibility of the compounds. Additional tests at 600 °C and 650 °C were required for the ESB-BSCF couple. The phase identification of the composite powders was performing by X-ray diffraction (XRD, Bruker D8 Advance) with a Cu Kα radiation.

The microstructure of the cathode/ electrolyte interface was examined using a scanning electron microscopy (SEM, Zeiss Neon 40EsB). For each cell that was analysed, two different samples were prepared: in the first one most part of the *in situ* cathode was removed by adhesive tape; in the second case, it was removed from the YSZ electrolyte after being immersed in 32% hydrochloric acid solution, treated in the ultrasonic cleaner for one hour and left in the acid overnight. Then a cross-sectional lamella of each sample treated with the adhesive tape was prepared in a Tescan Lyra focused ion beam-SEM (FIB-SEM). The microstructure and elemental mapping analyses of the lamella were performed by a high angle annular dark field scanning transmission electron microscopy (HAADF-STEM, FEI Titan G2 80-200 TEM/STEM with ChemiSTEM Technology) at 200kV.

RESULTS AND DISCUSSION

LSM-ESB

Thermo-compatibility tests

The mechanical mixed LSM and ESB was the first couple of materials to be tested. Figure 20 shows the XRD analysis of the mixed powders heated for 2 hours at different temperatures. The curves related to different test temperatures presents many peaks, which indicate the presence of one or more phases related to materials forming the composite powder. From a qualitative analysis of these data, LSM and ESB possess a good chemical compatibility at the temperatures chosen, since the curves do not show additional peaks apart from the ones expected by the rhombohedral perovskite of LSM and the cubic fluorite of ESB, apart from minor negligible peaks caused by errors in the measurement. In other words, the formation of impurity phases had been avoided during the test, according to these data.

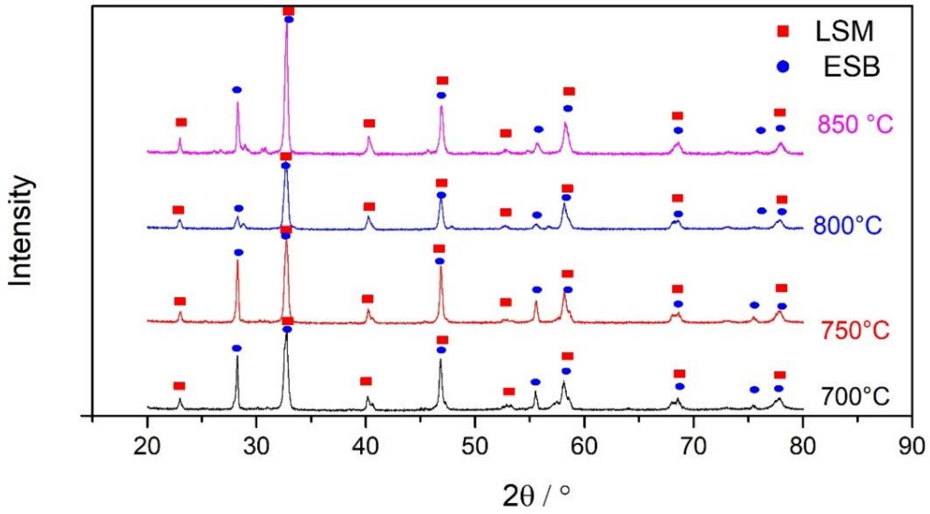

Figure 20 XRD patterns of the mixed LSM-ESB powder

Thus, in order to be sure of the chemical stability of the composite cathodes during the operation and to have the possibility to compare the results with the one obtained by the LSCF-ESB cathode at the same temperature, the electrochemical tests of the mixed LSM-ESB composite cathode were performed at 700 °C.

Electrochemical performances

In Figure 21 and Figure 22, the polarization curves and the impedance spectra of the electrochemical tests under cathodic polarization are represented. The initial value of R_Ω was 4.46 Ω cm^2 and 5.40 Ω cm^2 for the 250 mA cm^{-2} and 500 mA cm^{-2} current densities respectively. These high values are mainly due to the poor electronic conducting electrolyte and the electrical contacts between the *in situ*-applied cathode and the electrolyte and between the electrodes and the platinum meshes of the external circuit. It is possible to see a sensible decrease of the ohmic resistances during polarization in both cases, ending with a value of 3.52 Ω cm^2 for the low-current test (-21% of the initial value) and of 3.75 Ω cm^2 for the high-current test (-31% of the initial value). Since the resistance of the electrolyte is not expected to change during the test, these facts highlight the improvement in the charge conduction that can be explained with the formation of a proper cathode/electrolyte interface. Under the 250 mA cm^{-2} current polarization, the cathode polarization resistance R_p increased from an initial value of around 0.1 Ω cm^2 to a value around 0.4 Ω cm^2, kept constant during the test, but the decrease of the overall resistance (R_Ω+R_p) determined the decrease of the overvoltage of the cell, showing a constant behaviour after 4 hours of polarization until the end of the experiment (around -0.93 V). Under higher current densities, the behaviour was similar, with a further improvement in the final R_p (0.3 Ω cm^2 and 0.25 Ω cm^2), determining a more sensible reduction in the overvoltage.

The curves representing the impedance spectra measured during the cathodic polarization showed that the low-frequency suppressed arc, related to the gas diffusion process, overlapped the high-frequency arc, related to oxygen ion transfer from TPB to the YSZ electrolyte lattice or grain boundary resistance of YSZ. The low frequencies arc is dominant, as expected at relatively low temperatures[20], so we can say that the rate determining step of the reaction is the gas phase diffusion. The high ion conducting ESB material improved the ion transfer in the cathode bulk, decreasing the magnitude of the high-frequency arc.

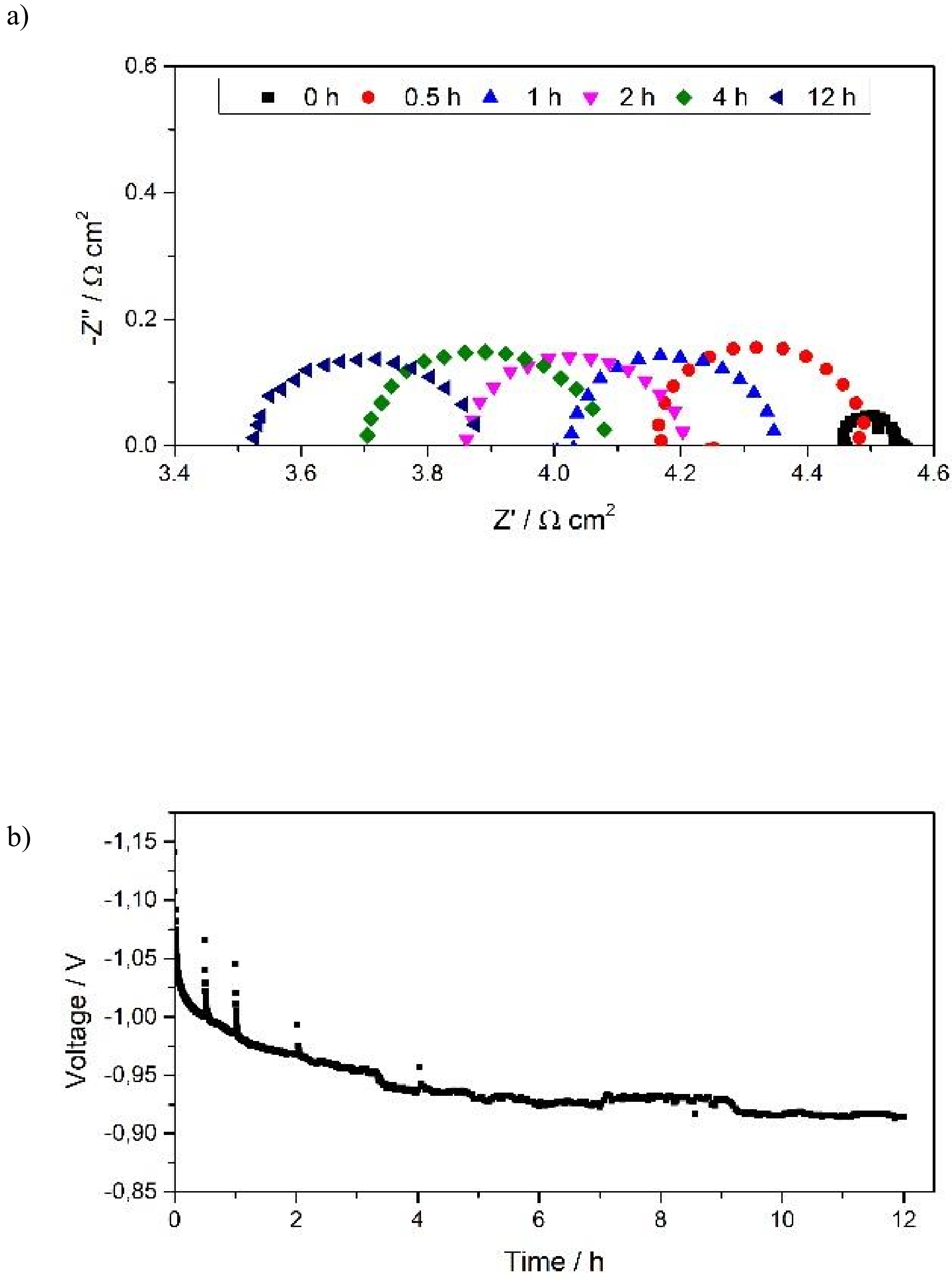

Figure 21 a) Impedance spectra and b) polarization response of direct assembled mixed LSM-ESB cathode under cathodic polarization at 250 mA cm^{-2} and at 700 °C

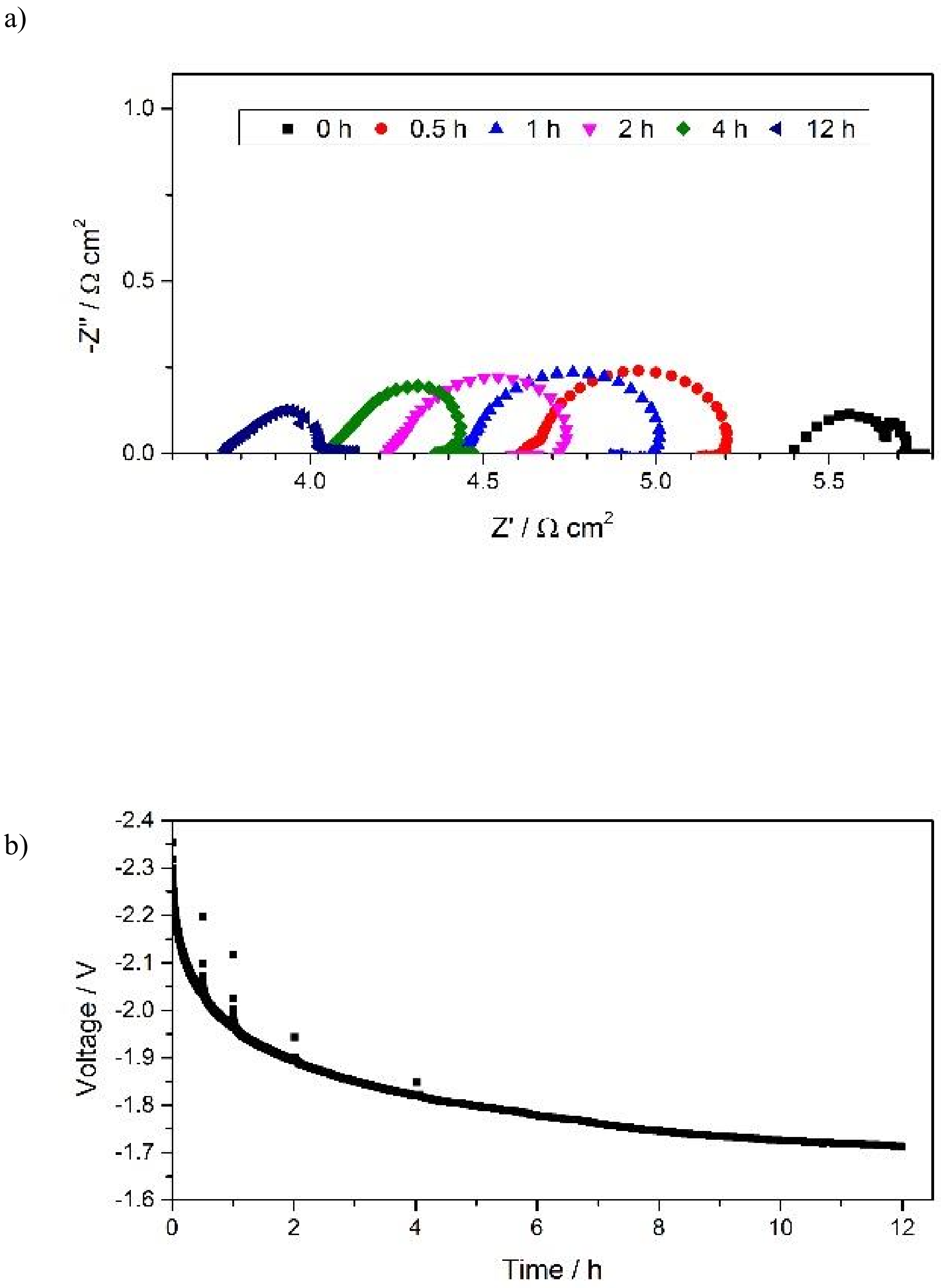

Figure 22 a) Impedance spectra and b) polarization response of direct assembled mixed LSM-ESB cathode under cathodic polarization at 500 mA cm^{-2} and at 700 °C

The behaviour of the electrochemical performances of the cells under anodic polarization was not characterized by the dramatic improvement that the ones under cathodic polarization had shown, as Figure 23 Figure 24 demonstrate. For the cell subjected at 250 mA cm^{-2} polarization, after an initial rise of the resistances and of the overvoltage, the slightly decrease R_{Ω} (from 5.12 Ω cm^2 to 4.86 Ω cm^2, -5%) and of the overvoltage suggested the formation of an effective interface, with a constant electrode polarization resistance (0.4 Ω cm^2). Under 500 mA cm^{-2} polarization, the improvement in the ohmic resistance R_{Ω} was more consistent (from 4.26 Ω cm^2 to 3.75 Ω cm^2, -12%), however, the overvoltage reduction was restrained by the increase in the polarization resistance R_p (from 0.05 Ω cm^2 to 0.4 Ω cm^2).

In contrast to the previous case, the high-frequency suppressed arc is clearly visible in the curves representing the impedance spectra measured during the anodic polarization, indicating a more sensible contribution of the charge transfer process to the polarization resistance of the cell, confirming the difficulties to form a good cathode/electrolyte interface by an anodic polarization. The low frequencies arc is still dominant and, thus, the gas diffusion process is the rate determining step of the reaction.

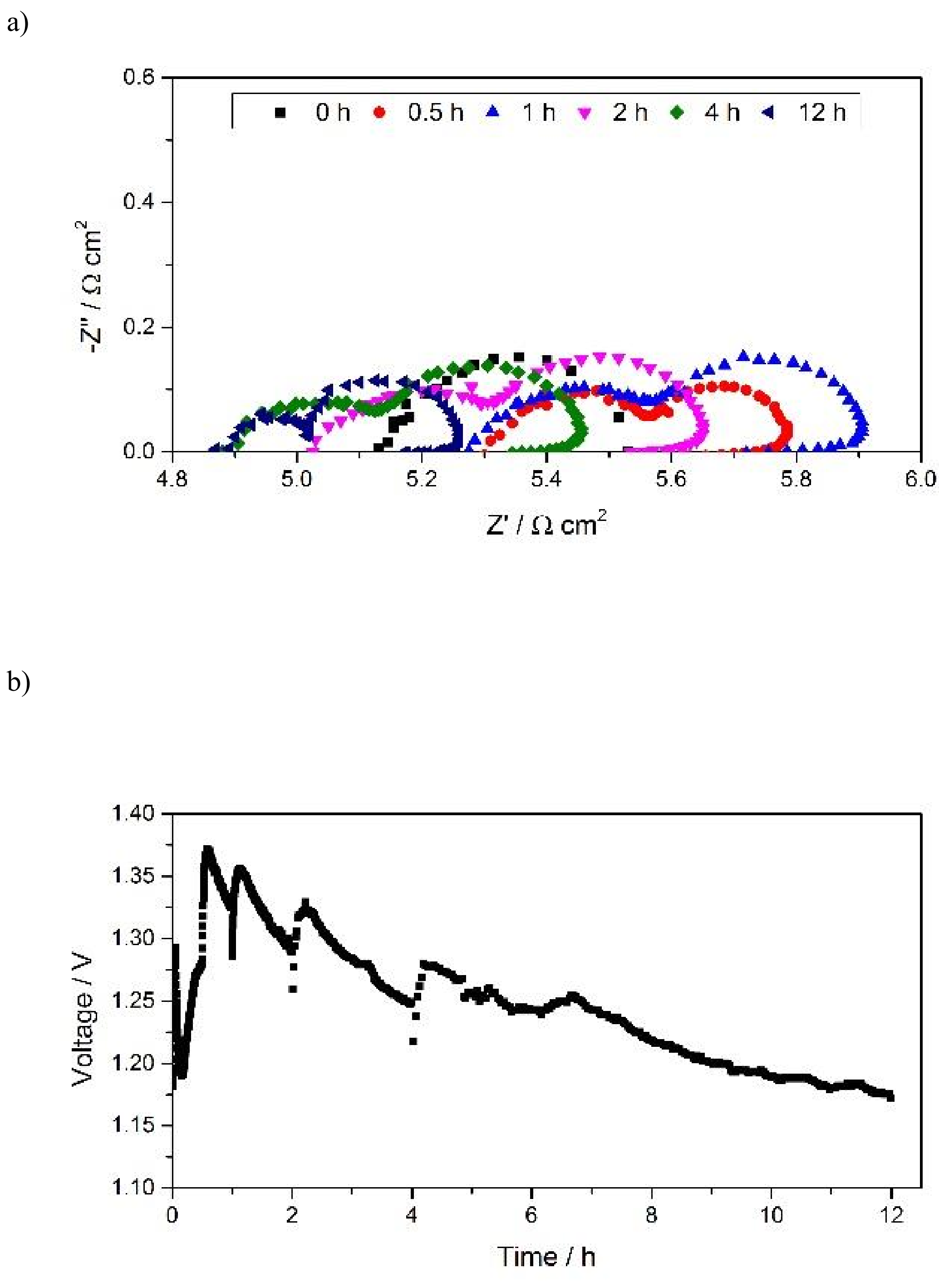

Figure 23 a) Impedance spectra and b) polarization response of direct assembled mixed LSM-ESB cathode under anodic polarization at 250 mA cm-2 and at 700 °C

a)

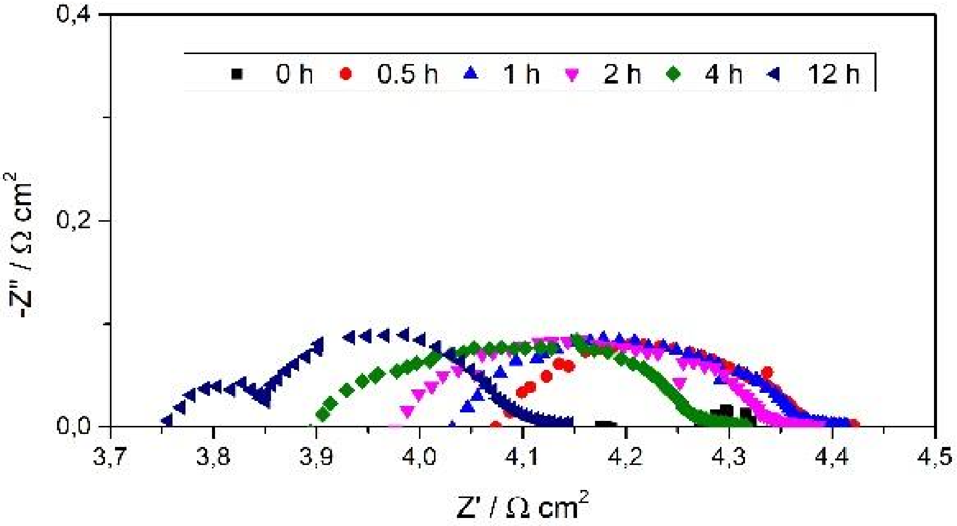

b)

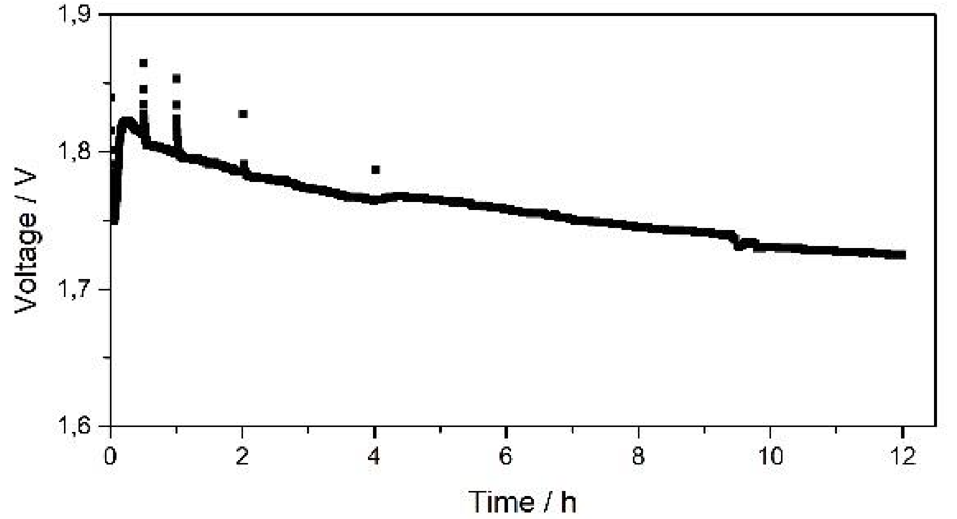

Figure 24 a) Impedance spectra and b) polarization response of direct assembled mixed LSM-ESB cathode under anodic polarization at 500 mA cm-2 and at 700 °C

Comparing the different polarizations, it results that the cathodic polarization was more effective in the formation of a good cathode/electrolyte interface in the first 12 hours of polarization of the cell. The mixed LSM-ESB cathode showed a good stability during the operation, keeping the polarization resistance R_P quite constant.

From the impedance spectra obtained from the test on a cell under open circuit condition, we can see the positive effects of the temperature especially on the performance of the LSM-ESB composite cathode, while it had much minor effects on the ohmic resistance of the cell: in fact the final reduction of R_Ω (-6% of the initial value, from 4.70 Ω cm^2 to 4.44 Ω cm^2) was negligible with respect the one occurred to R_P, decreased from 0.60 Ω cm^2 to 0.20 Ω cm^2 (-67%). This issue was not a surprise since the sintering temperature to form a thermally induced interface is much higher (around 1200 °C) than the test temperature[38]. The condition of the test allowed a better sintering and the formation of a more effective composite cathode.

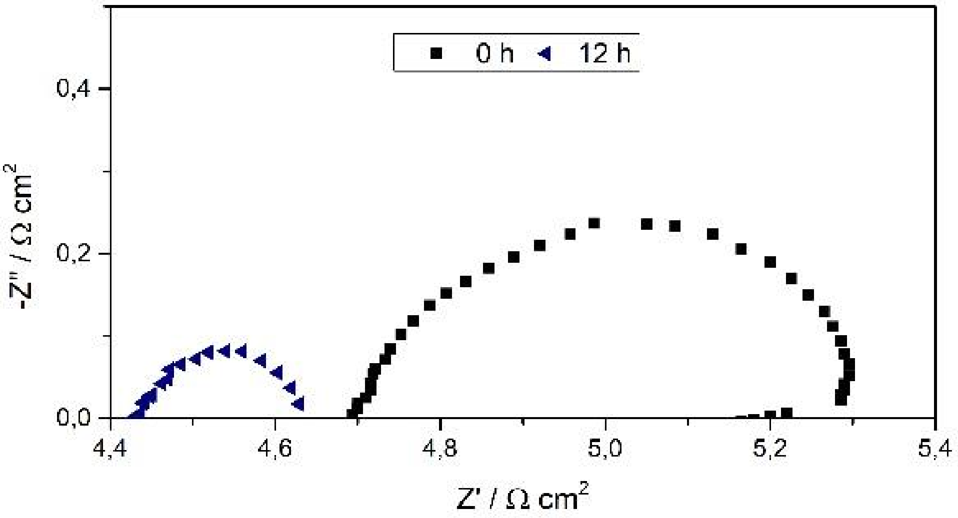

Figure 25 Impedance spectra of direct assembled mixed LSM-ESB cathode under open circuit condition at 700 °C

The value of the polarization resistances were much lower to those obtained by *in situ* direct applied pristine LSM cathode with the same configuration at 800 °C (1.41 Ω cm^2 at the end of the electrochemical test)[39]. The incorporation of ESB phase in the bulk of the cathode allowed to reach dramatically improved performances at lower temperature.

Microstructural analysis

The LSM-ESB cathode/YSZ electrolyte interface of the half-cells tested was analysed firstly using a scanning electron microscopy (SEM). The samples prepared were taken from the cell polarized with the 250 mA cm^{-2} current density because they showed a more stable behaviour during the electrochemical tests. Figure 26 shows the YSZ interface in contact with the cathode of the cell underwent the 12-hour cathodic polarization, after the electrode had been removed by the hydrochloric acid. The non-smooth surface and the grain boundaries characterizing the YSZ layer are characteristic of the dry pressing method chosen to prepare the electrolyte. Apart from some particles derived probably from the preparation of the sample, the surface is quite clean and some circular contact marks, pointed by the red arrows, with a size of the order of around 300 nm are clearly visible on the grain of YSZ electrolyte. The fact that they are not present on the free YSZ surface in Figure 27 representing the sample treated with the adhesive tape suggest that they are the contact marks of the cathode particles and the electrolyte. In the case of *in situ* assembled pristine LSM cathode studied by Jiang et al.[41] the surface of the electrolyte after the polarization was completely clean, so we can say that the marks observed were caused by the ESB phase and they provided a more intimate contact between the cathode bulk and the electrolyte, testified by the improvement in the ohmic resistance during the test. The marks are formed by the cathodic polarization, since they are not visible on the surface of the electrolyte of the cell tested under anodic polarization, as we can see in Figure 28.

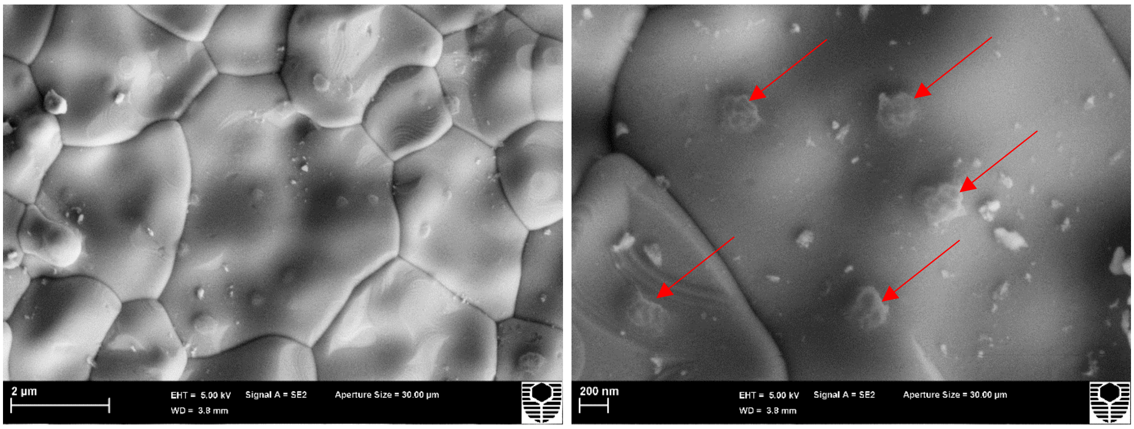

Figure 26 SEM images at different resolution of the YSZ surface after 12-hour cathodic polarization at 250 mA cm^{-2} and removal of the direct applied mixed LSM-ESB cathode by acid treatment

In Figure 27, the irregular grain-shaped porous structure of the cathode can be observed from the electrolyte not peeled away by the adhesive tape. The bigger particles with dimensions of the order of 1 µm pointed by the arrows are ESB particles, synthetized by the sol-gel method. Probably the high wettability and the lower melting temperature of the ESB[45] caused the agglomeration of the particles at the testing temperature, helped by the fact that the composite cathode was prepared with a not sophisticated method such as the mechanical mixing, in which the two phases are quite separated and distinguishable. This great discrepancy in dimensions of the particles can be reduced with the synthesis of nanoscale engineered composite cathode or even with very simple techniques for the particle size reduction (e.g. ball milling) in order to obtain a more uniform structure to increase the number of TPB sites in the cathode, with a consequent improvement in the performances of it. Any plat-like or layer-shaped large particles or thin layers are evident on the surface, confirming the chemical stability between the materials of the half-cell tested.

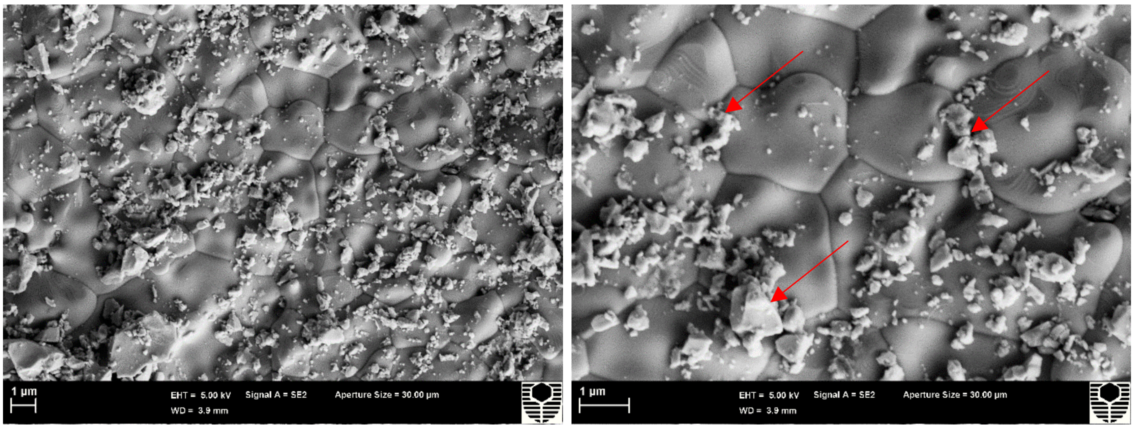

Figure 27 SEM images at different resolution of the YSZ surface after 12-hour cathodic polarization at 250 mA cm-2 and removal of the directly assembled mixed LSM-ESB cathode by adhesive tape

The samples were then cut and lamella for the FIB-SEM analysis were prepared to obtain the elemental EDS maps shown in Figure 30 and in more detail in Figure 31. The EDS maps display a substantial distinction in the LSM and ESB phases in relatively large-dimension particles, in fact they had dimensions in the order of µm. It is interesting to notice the tendency of ESB to occupy the space near the cathode/electrolyte interface. In particular in Figure 31 a layer of ESB phases can be noted connecting LSM particles to the YSZ dense layer, not overlapping it. The high wettability and the greater mobility by surface or lattice diffusion thanks to the lower melting temperature of the bismuth oxide with respect to the LSM and YSZ (827 °C and >2000 °C respectively) can explain the formation of a ESB layer at the interface[36]. ESB, characterized by a higher ion conductivity with respect to LSM, facilitates a faster oxygen migration through the electrolyte and enhances the electrocatalytic activity of the cathode[46].

The presence of manganese outside the LSM particles, that can be observed in Figure 30, does not imply a segregation of the element, since it was observed locally in some sites of the cathode.

The surface of the anodic polarized sample treated with acid is very clean and any thin layers are present, as it can be seen in Figure 28. However, some irregular shaped contact marks, indicated by red arrows, are present on the surface of the interface, but different in shape and dimensions from the one observed in the previous case. They were caused by the electrode particles, since they are not visible in Figure 29, related to the sample treated with the adhesive tape.

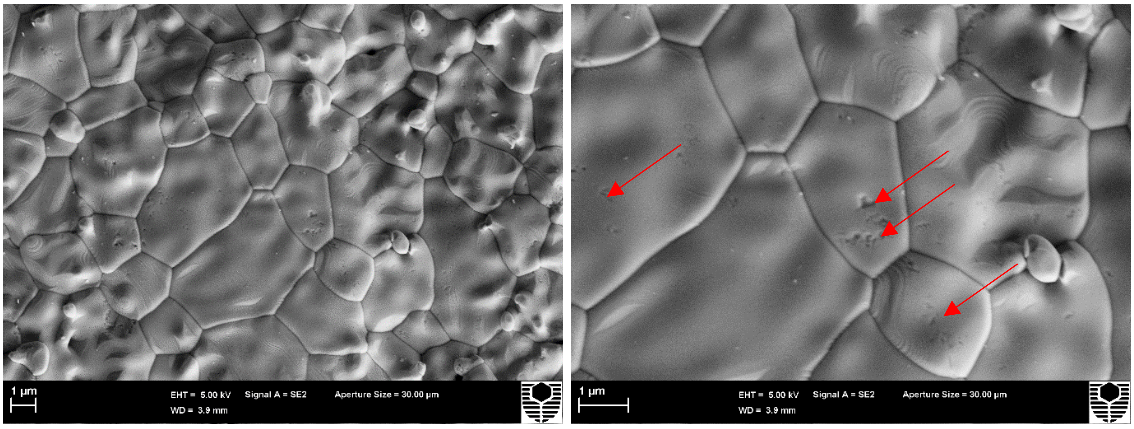

Figure 28 SEM images at different resolution of the YSZ surface after 12-hour anodic polarization at 250 mA cm-2 and removal of the direct applied mixed LSM-ESB cathode by acid treatment

The shape and dimensions of the particles are similar to the one observed on the cathodic polarized sample, because the different polarization cannot modify sensibly the microstructure of the cell in 12 hours of application.

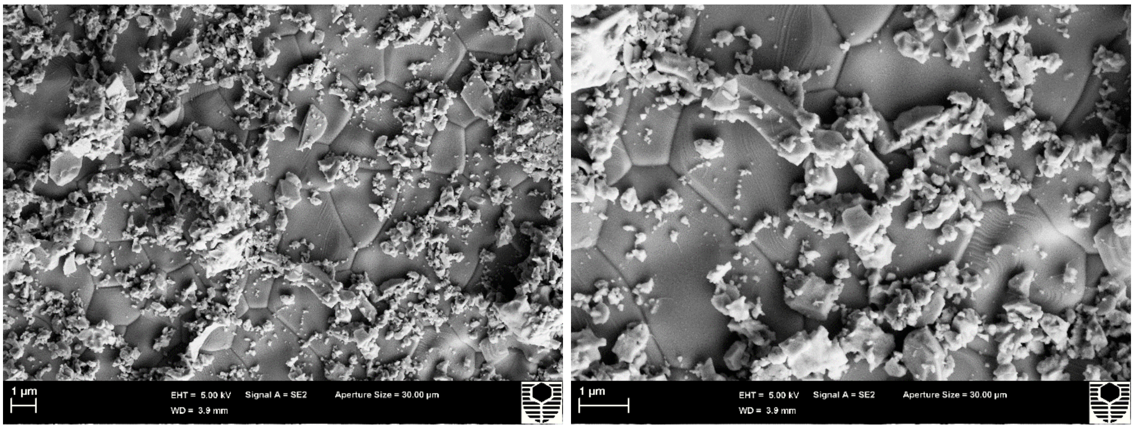

Figure 29 SEM images at different resolution of the YSZ surface after 12-hour anodic polarization at 250 mA cm-2 and removal of the direct applied mixed LSM-ESB cathode by adhesive tape

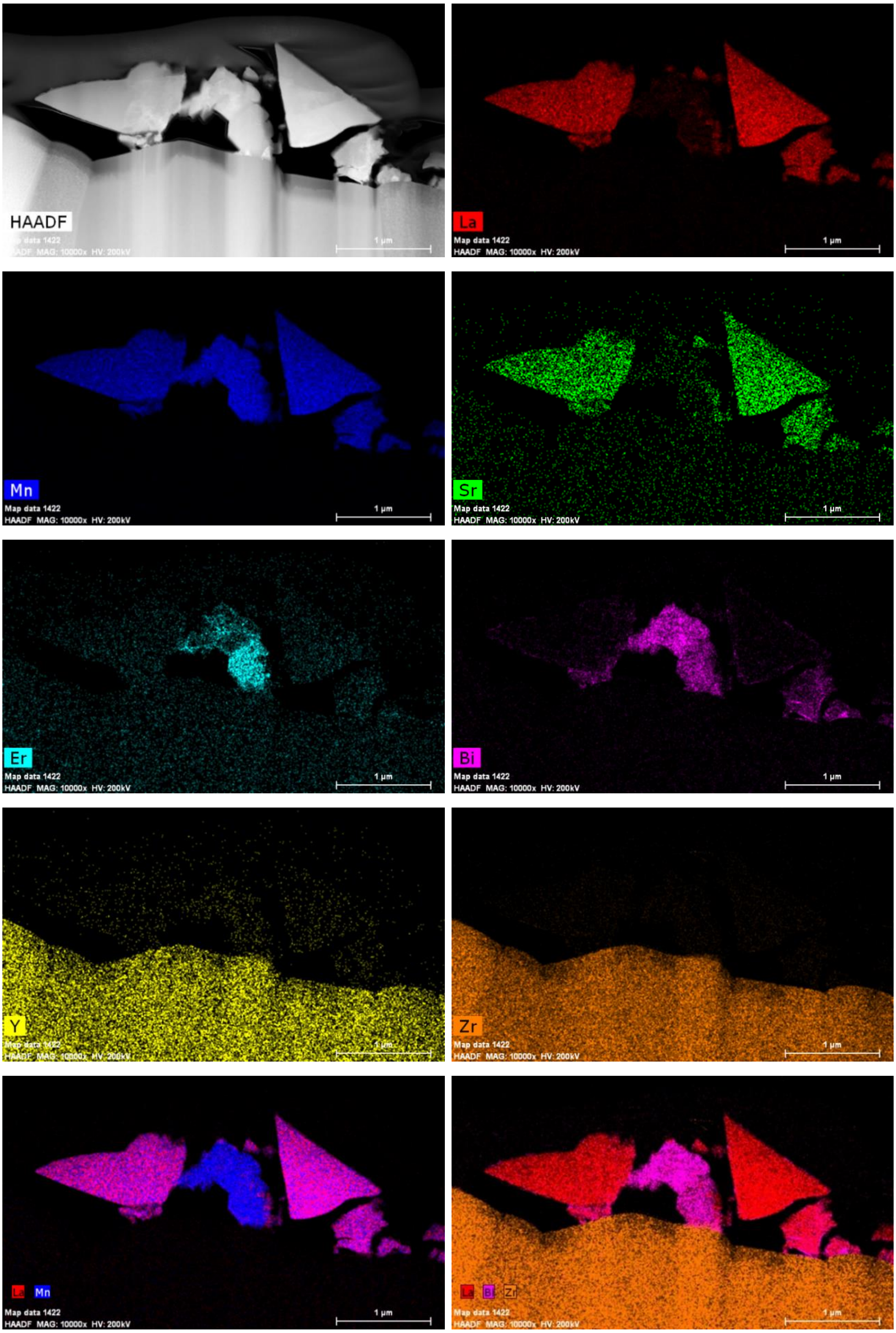

Figure 30 STEM-EDS maps of electrode/electrolyte interface after the directly assembled mixed LSM-ESB cathode was polarized at 250 mA cm^{-2} and 700 °C for 20 h under fuel cell mode

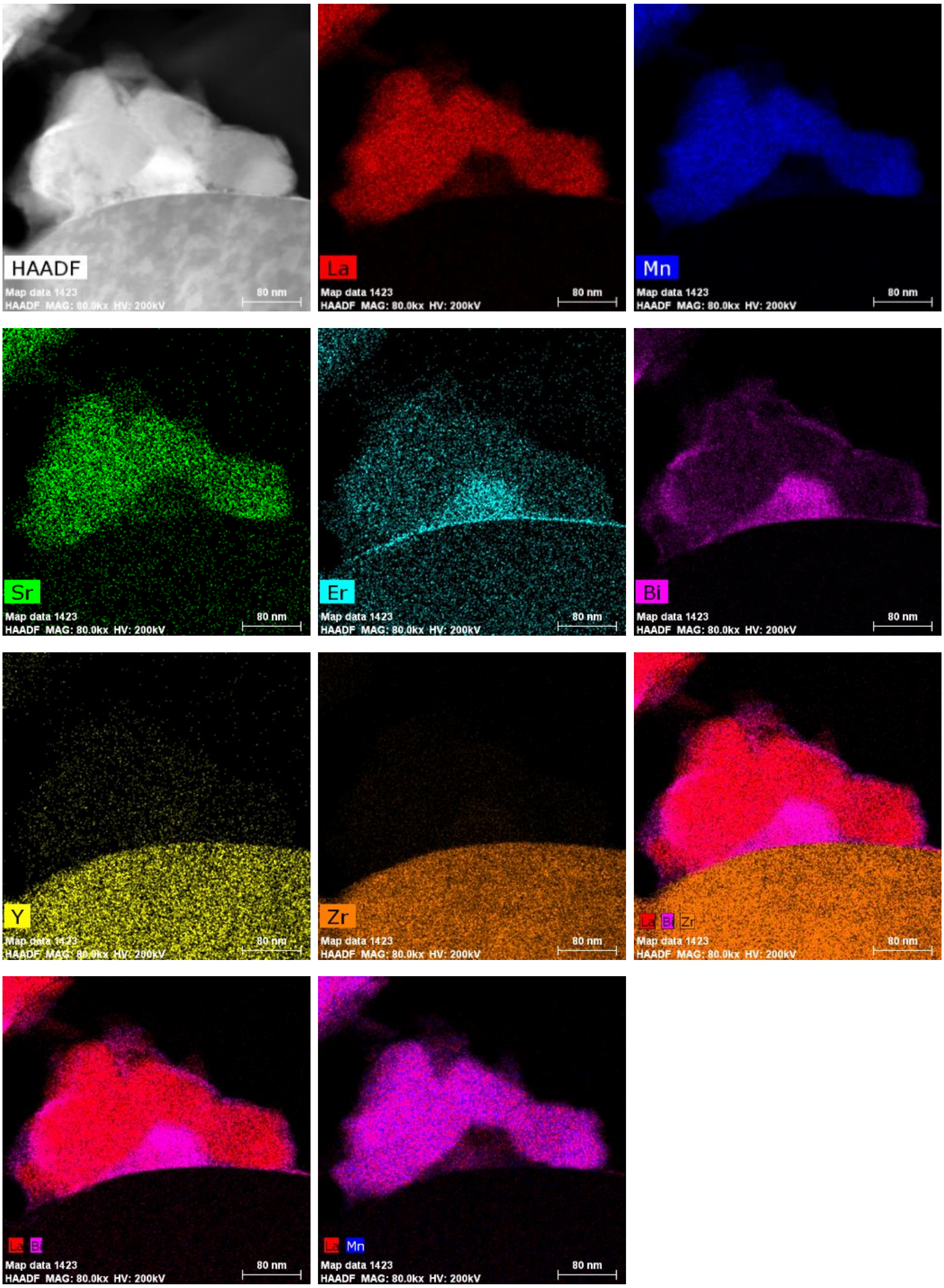

Figure 31 Detail of FIB-STEM elemental mapping of directly assembled mixed LSM-ESB cathode after 12-hour 250 mA cm^{-2} *cathodic polarization, showing ESB and LSM particles incorporated at the interface*

The elemental mapping of the lamella prepared from the sampled underwent the anodic polarization still shows the separation between the phases in relatively big particles, as shown in Figure 32.

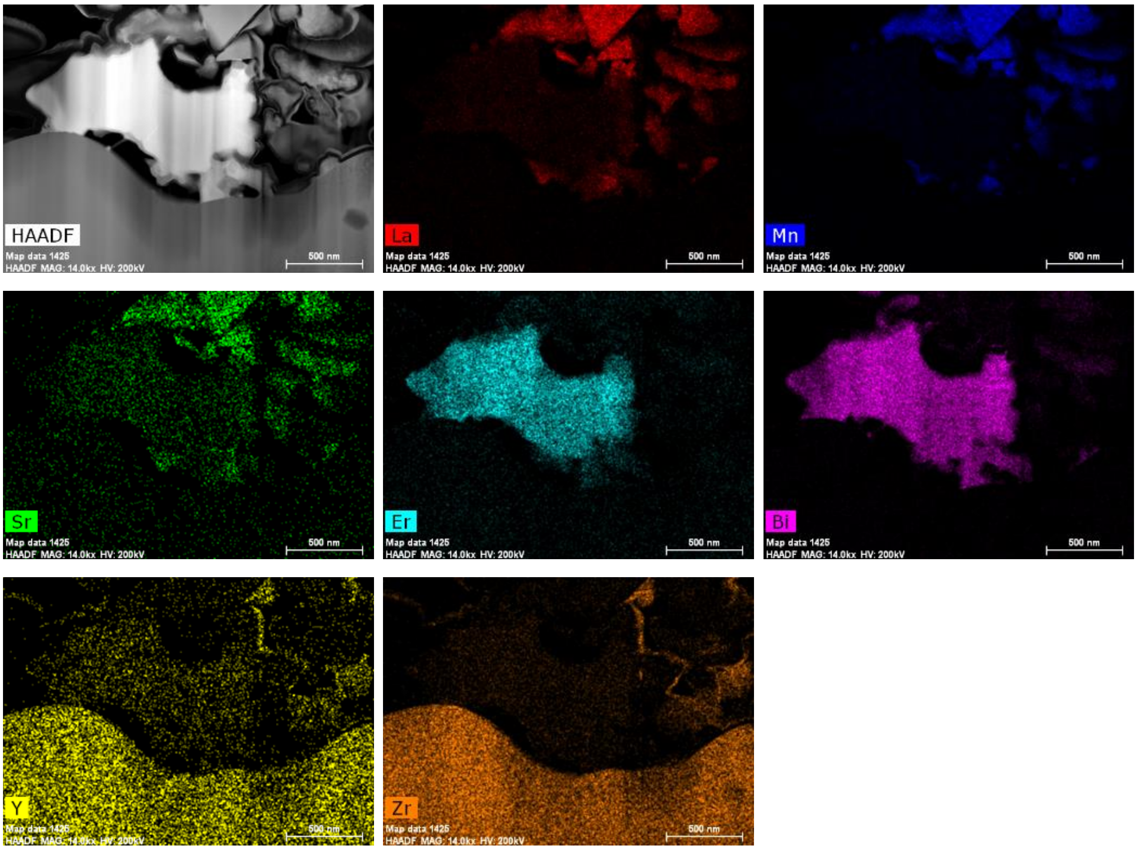

Figure 32 STEM-EDS maps of electrode/electrolyte interface after the directly assembled mixed LSM-ESB cathode was polarized at 250 mA cm−2 and 700 °C for 20 h under electrolysis mode

Enhancing the resolution of the mapping, we can see that is the ESB phase that predominantly tends to be in direct contact with YSZ electrolyte with respect to the LSM phase, as observed in the previous case. However, it is not visible a distinctive ESB layer. The formation of an ESB phase in direct contact with YSZ electrolyte is probably formed during the polarization and it can explain the improvement in the electrochemical performances of the cell seen in the previous analysis, thanks to a faster ionic migration guaranteed by such a good ionic conductor as ESB.

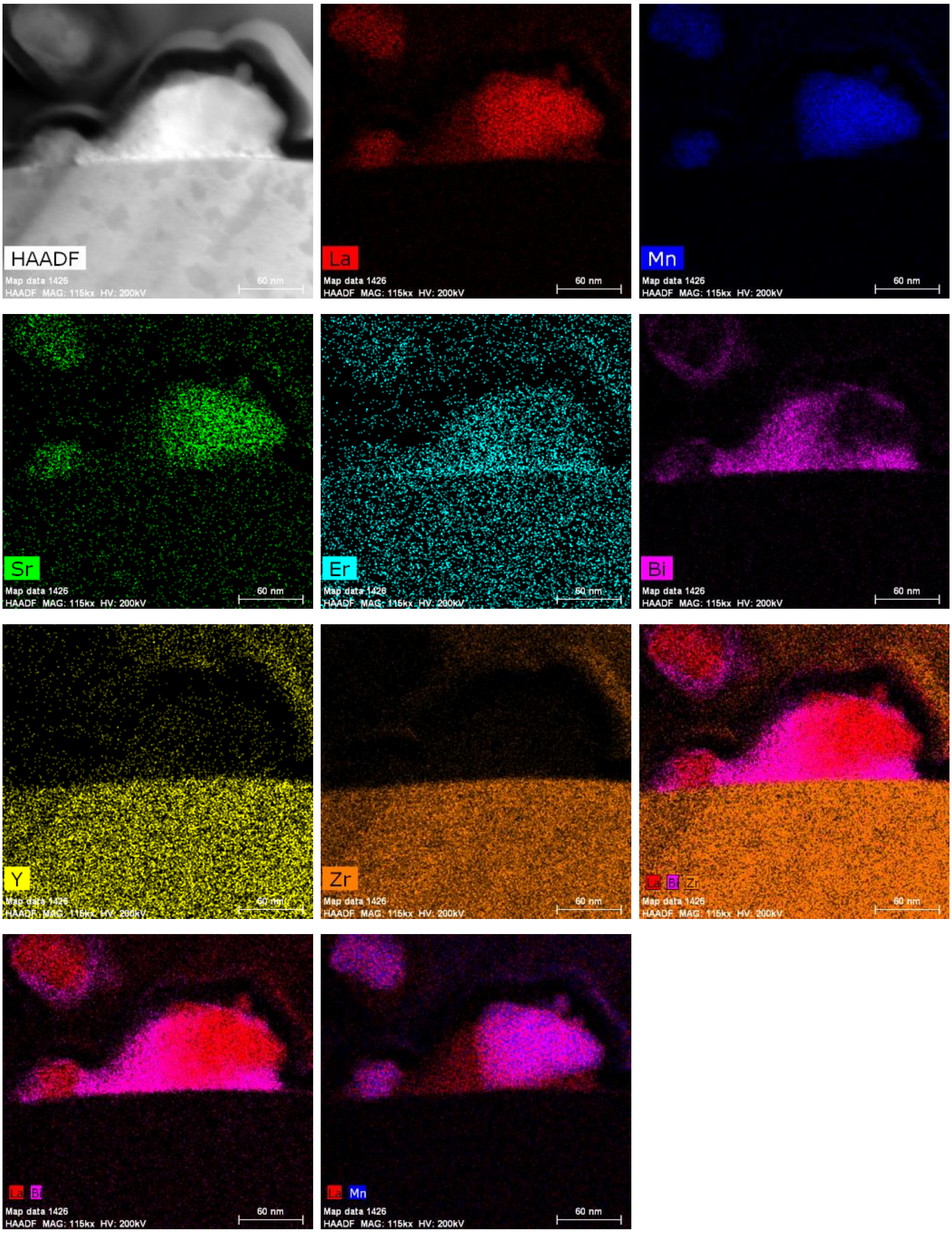

Figure 33 Detail of FIB-STEM elemental mapping of directly assembled mixed LSM-ESB cathode after 12-hour 250 mA cm-2 anodic polarization, showing ESB and LSM particles incorporated at the interface

ESB decorated LSM

We proved that the incorporation of an ionic conductive phase in the LSM bulk through a very simple mechanical mixing in a mortar improved sensibly the performance of the cathode, allowing to reduce the operating temperature of an LSM cathode at 700 °C. Nevertheless, we have seen that the microstructure of the composite electrode was not optimized and that the two phases were clearly separated. A decoration process of the surface of LSM bulk with the ESB phase can enhance considerably the TPB length from that restricted to the cathode/electrolyte interface of the pristine LSM electrode and the not-optimized one of the mixed LSM-ESB cathode. For this reason, a nanostructured LSM-ESB composite powder was synthetized with the gelation method and then sintered at 650 °C for 2 hours. After that, it was mixed with the ink vehicle in a weight ratio of 7:3 and directly applied on the electrolyte surface. The electrochemical tests were run at 700 °C.

Electrochemical tests

From the behaviour of the impedance spectra of the cells tested under 12-hour constant cathodic polarization showed in Figure 34a and Figure 35a, we can immediately see the improvement in the electrocatalytic activity of the oxygen reduction reaction that a nanoscale engineered cathode can cause with respect to one obtained by simple mechanical mixing of the two materials. The final cathode polarization resistances R_p were 0.06 Ω cm^2 and 0.21 Ω cm^2 in the case of 250 mA cm^{-2} and 500 mA cm^{-2} current density respectively. The cathodic polarization had a beneficial effect both in the cathode performance (the final R_p showed a -90% and -70% decrease respectively compared to the initial ones) and on the contact resistance between the cathode and the electrolyte (-42% and -38% of decrease of the ohmic resistance R_Ω during the tests). It has been proved that the passage of current in the cathode produce an activation effect on LSM[38]: in fact the polarization enables the incorporation of passive species such as SrO, placed on the surface of LSM bulk, into the perovskite structure[19]. The activation effect probably plays a role in the decreasing of the polarization resistance. Moreover, the passage of the current acts as a driving force that improves the contacts between the particles of the composite cathode, forming passages for ionic and electronic transfer, as proved by Jiang et al.[42] in recent works. As a consequence, the polarization responses showed a sensible decrease and a stable behaviour, as shown in Figure 34b and Figure 35b.

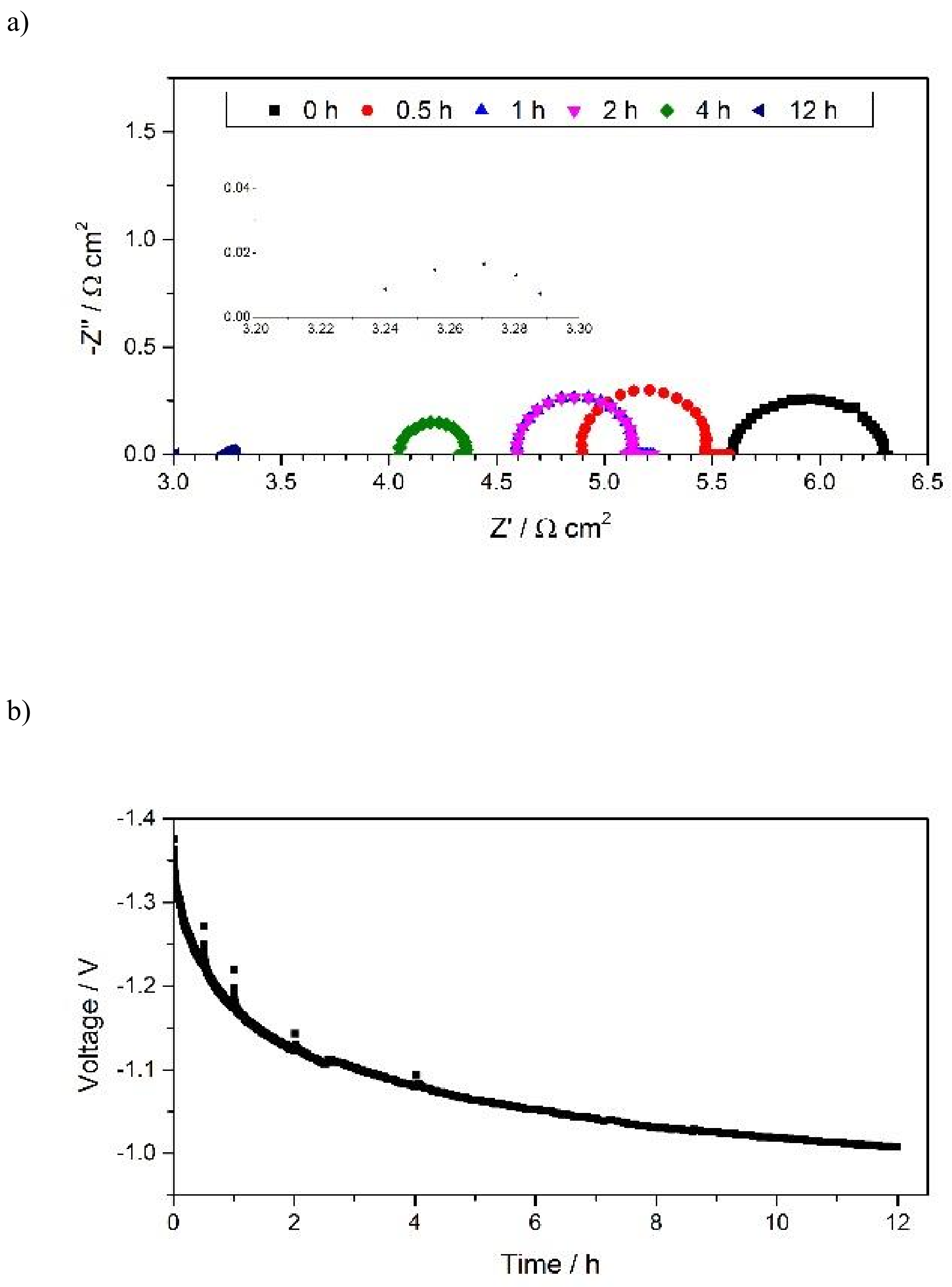

Figure 34 a) Impedance spectra and b) polarization response of direct assembled ESB decorated LSM cathode under cathodic polarization at 250 mA cm-2 and at 700 °C

a)

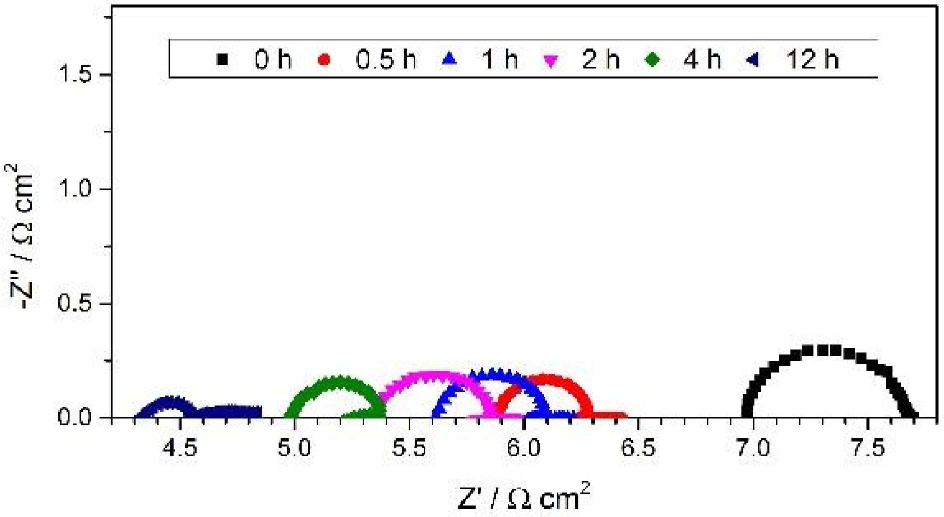

b)

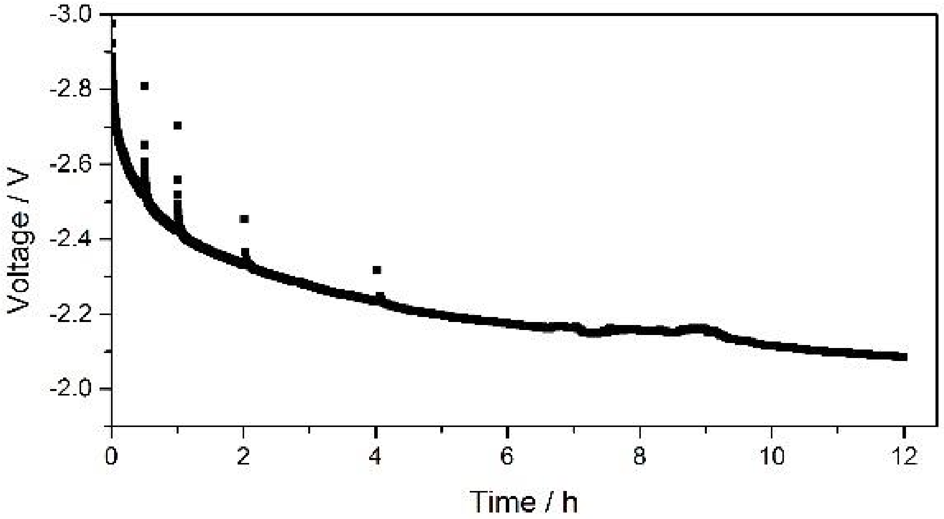

Figure 35 a) Impedance spectra and b) polarization response of direct assembled ESB decorated LSM cathode under cathodic polarization at 500 mA cm-2 and at 700 °C

The decoration method allowed the cathode to show more stable performances under anodic polarization as compared to the mixed composite cathode. As shown in Figure 36a and Figure 37a, R_p remained very stable and constant during the test (it had a decrease of 67% after 30 minutes under the 250 mA cm^{-2}) with final value of 0.49 Ω cm^2 and 0.72 Ω cm^2 in the case of 250 mA cm^{-2} and 500 mA cm^{-2} current density respectively. The contact resistance between cathode and electrolyte showed a more consistent improvement as compared to the previous case as well, as proved by the decrease of the 29% and of the 17% of R_Ω in the two cases, even if it did not reach the low values registered in the fuel cell mode, indicating that the anodic polarization does not allow the formation of a perfect electrode/electrolyte interface. The polarization response of the half-cell decreased and remained very stable during the test.

a)

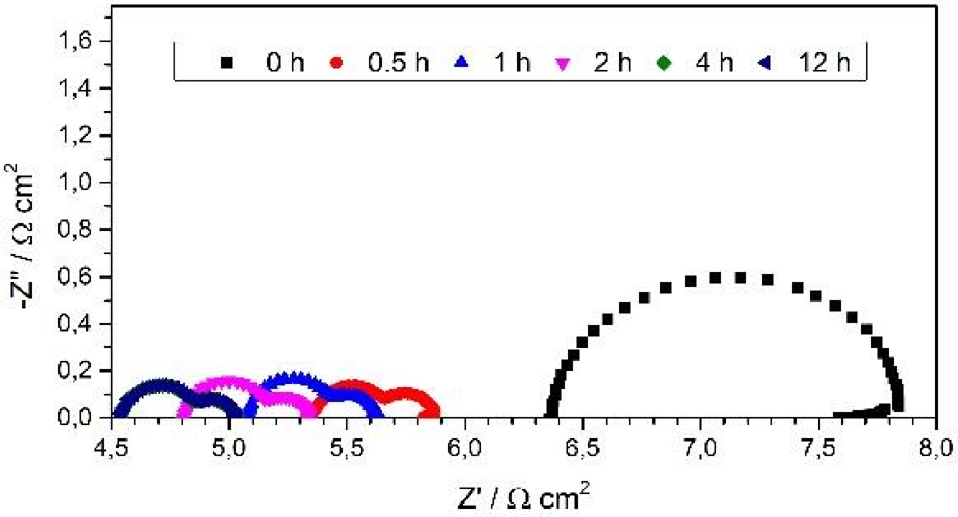

b)

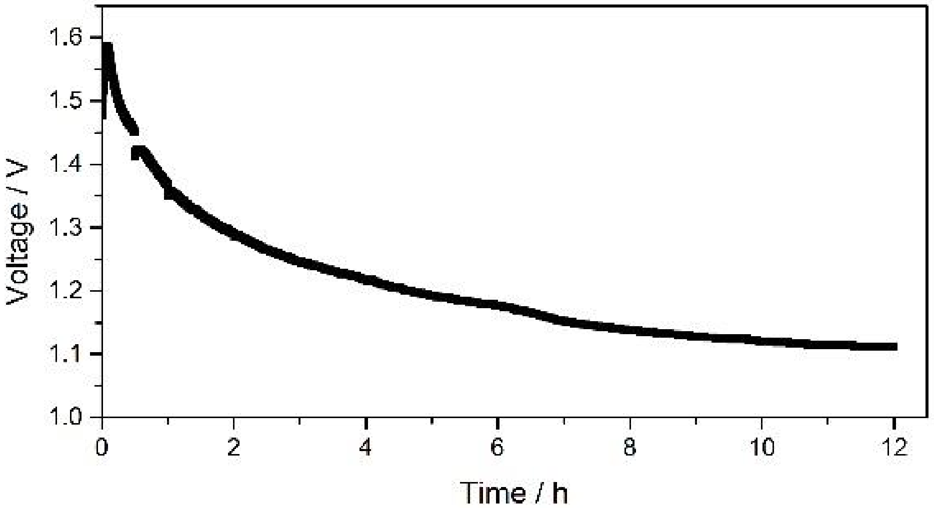

Figure 36 a) Impedance spectra and b) polarization response of direct assembled ESB decorated LSM cathode under anodic polarization at 250 mA cm-2 and at 700 °C

a)

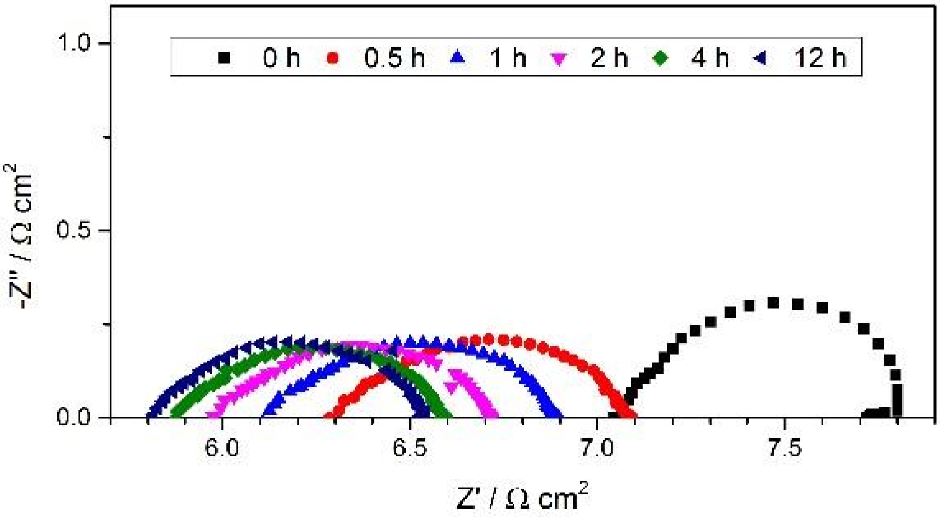

b)

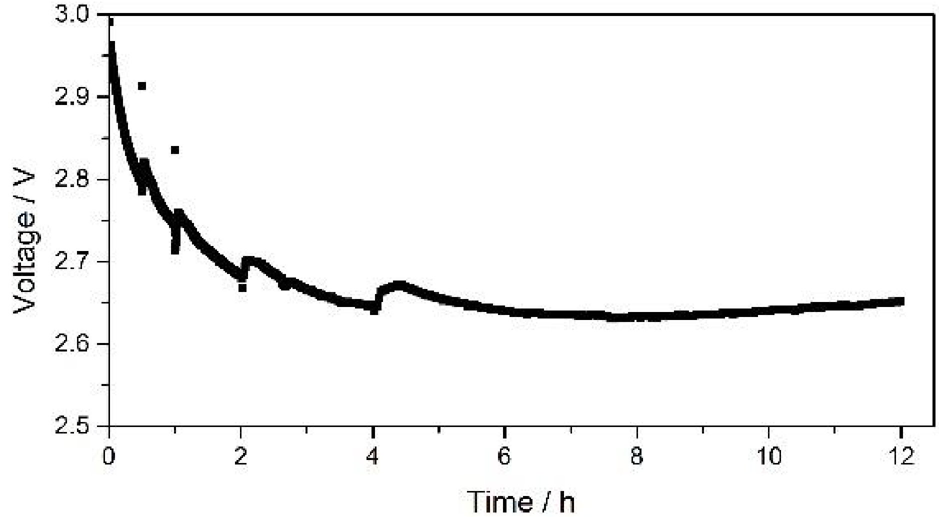

Figure 37 a) Impedance spectra and b) polarization response of direct assembled ESB decorated LSM cathode under anodic polarization at 500 mA cm-2 and at 700 °C

Observing the impedance spectra showed in Figure 38, during the test the positive effect of the temperature allowed an improvement in the structure of the cathode and a consequent improvement in the performance, with a decrease of the 46% for R_p and of 20% for R_Ω, due to the sintering effect of the testing at 700 °C for 12 hours.

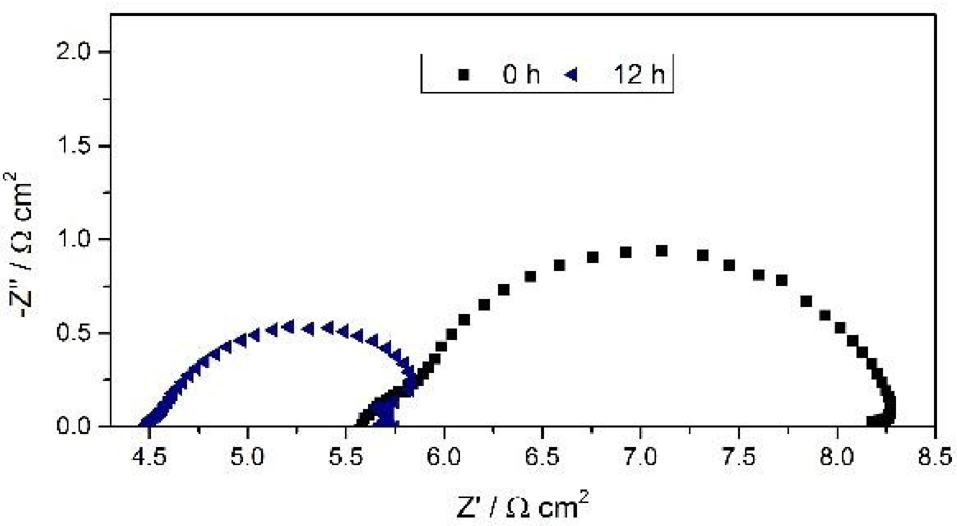

Figure 38 Impedance spectra of direct assembled ESB decorated LSM cathode under open circuit condition at 700 °C

Microstructural analysis

At first, the outer surface of the YSZ electrolyte layer of the cells tested was observed with the scanning electron microscope, removing the applied ESB decorated LSM cathode with the hydrochloric acid treatment or with an adhesive tape. It was not possible to analyse the cell tested under cathodic polarization, since the YSZ supporting pellet had been reused from previous tests after been properly polished and its surface was too rough to be analysed. Observing the electrolyte surface after 250 mA cm^{-2} anodic polarization and the removal of the cathode by adhesive tape shown in the SEM images of Figure 39, it is possible to immediately note a finer structure of the cathode not peeled away from the adhesive tape with respect to the case of the mixed LSM-ESB one, with a fewer number of particles bigger than 1 µm. The decoration method allowed the formation of smaller and more homogeneous particles, enhancing in this way the active surface of the cathode and thus contributing to the improvement of its performances.

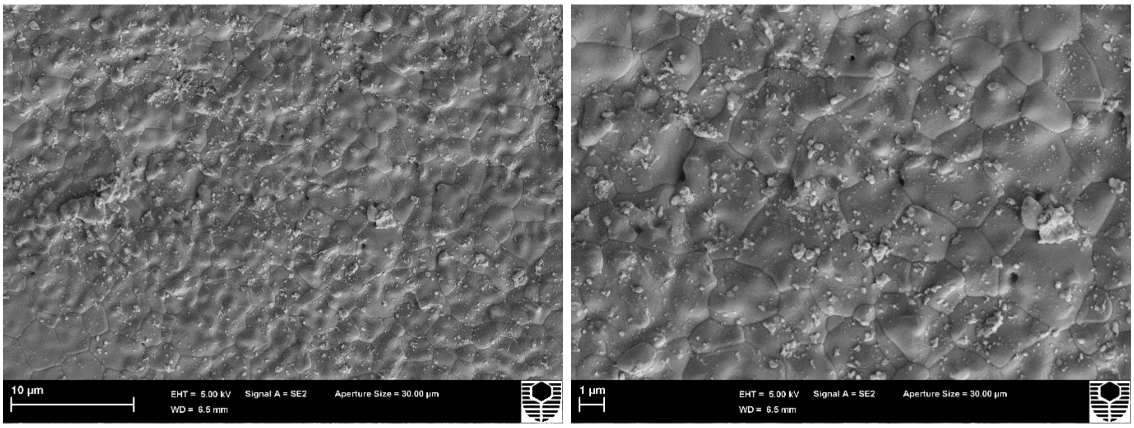

Figure 39 SEM images at different resolution of the YSZ surface after 12-hour anodic polarization at 250 mA cm^{-2} *and removal of the direct applied ESB decorated LSM cathode by adhesive tape*

After the removal of the cathode by the hydrochloric acid treatment, the YSZ surface showed the contact marks caused by the polarization as in the previous case, as it can be seen in Figure 40. Due to the finer microscopic structure described above, the contact marks are smaller and well dispersed on all over the grained surface of the electrolyte, enhancing the number of the contact points between the electrode and the electrolyte and improving the effectiveness and stability of the interface.

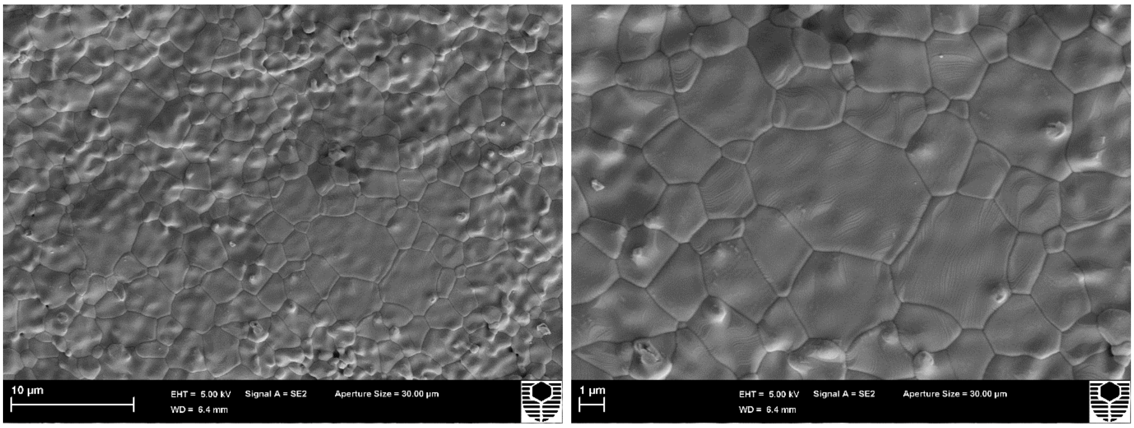

Figure 40 SEM images at different resolution of the YSZ surface after 12-hour anodic polarization at 250 mA cm^{-2} *and removal of the direct applied ESB decorated LSM cathode by acid treatment*

Figure 41 shows the YSZ surface of the half-cell tested for 12 hours in open circuit condition after the removal of the cathode by adhesive tape. The grain boundaries of the YSZ are clearly visible due to the dry-pressing fabrication method of the pellet, the surface is relatively flat and smooth, and no contact marks or layers are present, thanks to the great thermal stability of the materials, as the very stable performance of the respective cathode can also testify.

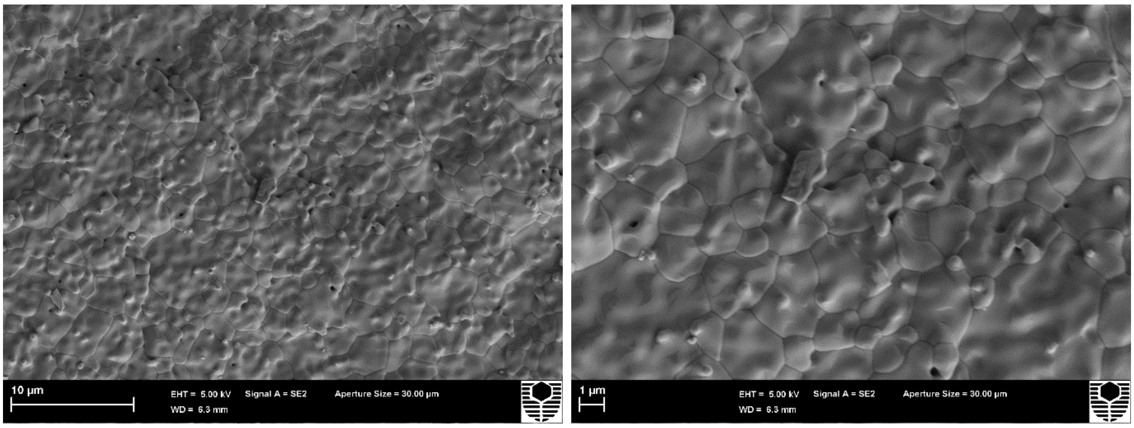

Figure 41 SEM images at different resolution of the YSZ surface after 12-hour open circuit condition at 700 °C and removal of the direct applied ESB decorated LSM cathode by acid treatment

Then, two lamellae from the half-cells tested under 250 mA cm^{-2} cathodic and anodic polarization were prepared using the FIB-SEM, in order to characterize the elemental distribution of the particles at the interface. Figure 42 highlights the elemental distribution of the cathode particles at the interface of the cell after the polarization of the cathodic current. The structure is completely different as compared to that observed in the mixed composite cathode, since no phase separation is visible from these images. The structure is uniform and highly porous, producing a larger ESB/LSM surface and, as a consequence, a larger active area for the electrochemical reactions and a larger TPB length. Moreover, the resulting structure by the decoration method allows a more direct ESB ion-conducting network to the LSM bulk. The observed structure suggests that the decoration method has an excellent stability during the test, showed also by the good performance under open circuit condition.

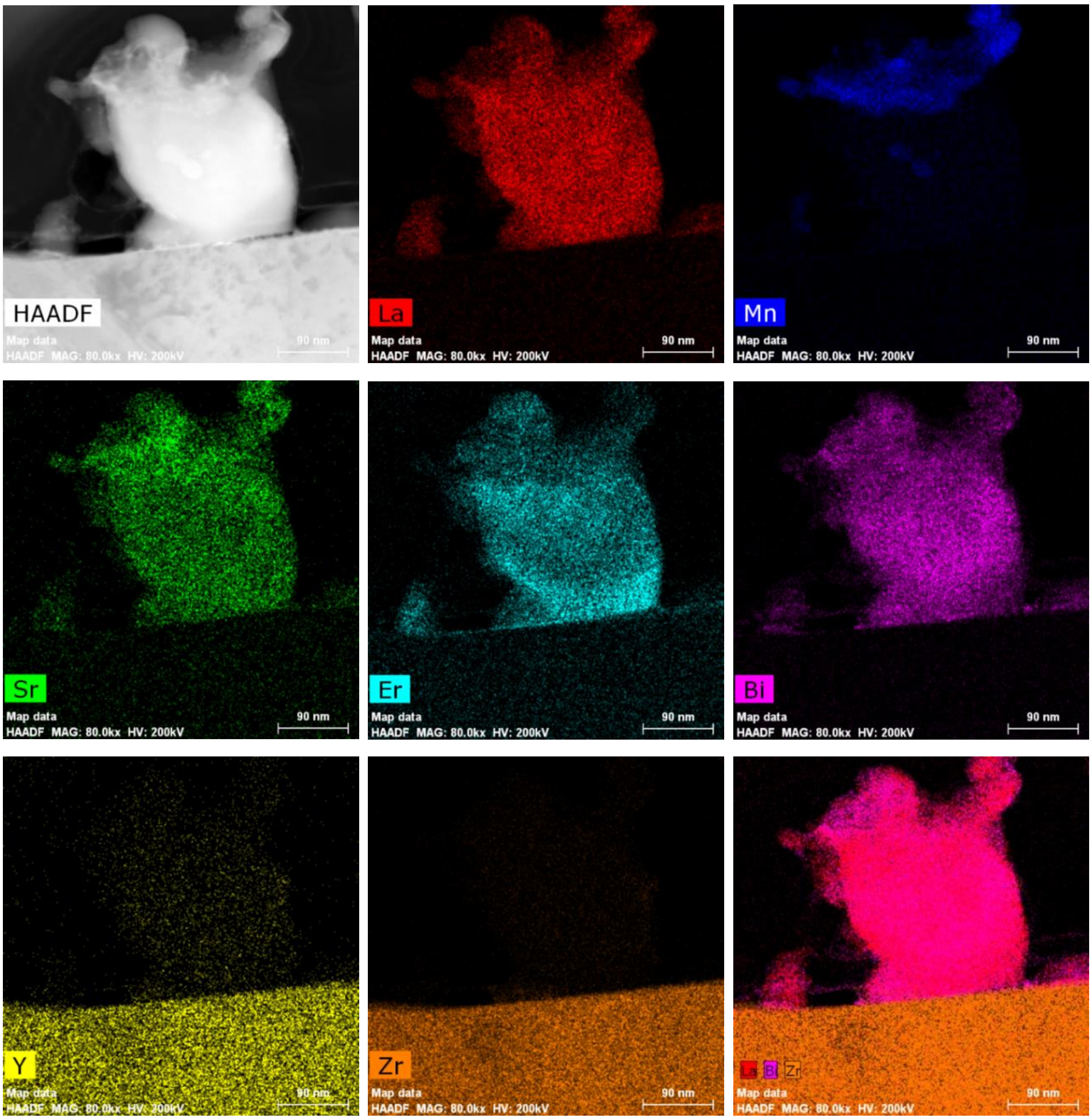

Figure 42 STEM-EDS maps of electrode/electrolyte interface after the directly assembled ESB decorated LSM cathode was polarized at 250 mA cm^{-2} and 700 °C for 20 h under fuel cell mode

The LSM particles are encapsulated in an ESB network, with the ESB phase occupying the voids in the LSM porous structure, as it can be seen in Figure 43, showing the STEM-EDS elemental mapping of the FIB-STEM prepared lamella of the cathode polarized with an anodic current for 12 hours at 700 °C. The structure is more porous and finer as compared to the mixed composite cathode. As observed in the previous case, the ESB phase predominantly occupies the cathode/electrolyte interface, due to the great wettability and the low melting temperature of the material, showing a better adhesion with a greater contact area between the electrode and the YSZ layer, acting as a bridge for the ion migration from the electrolyte to the cathode. The separation between the YSZ phase and the cathode phases suggests that the materials were chemical stable and no chemical reaction occurred.

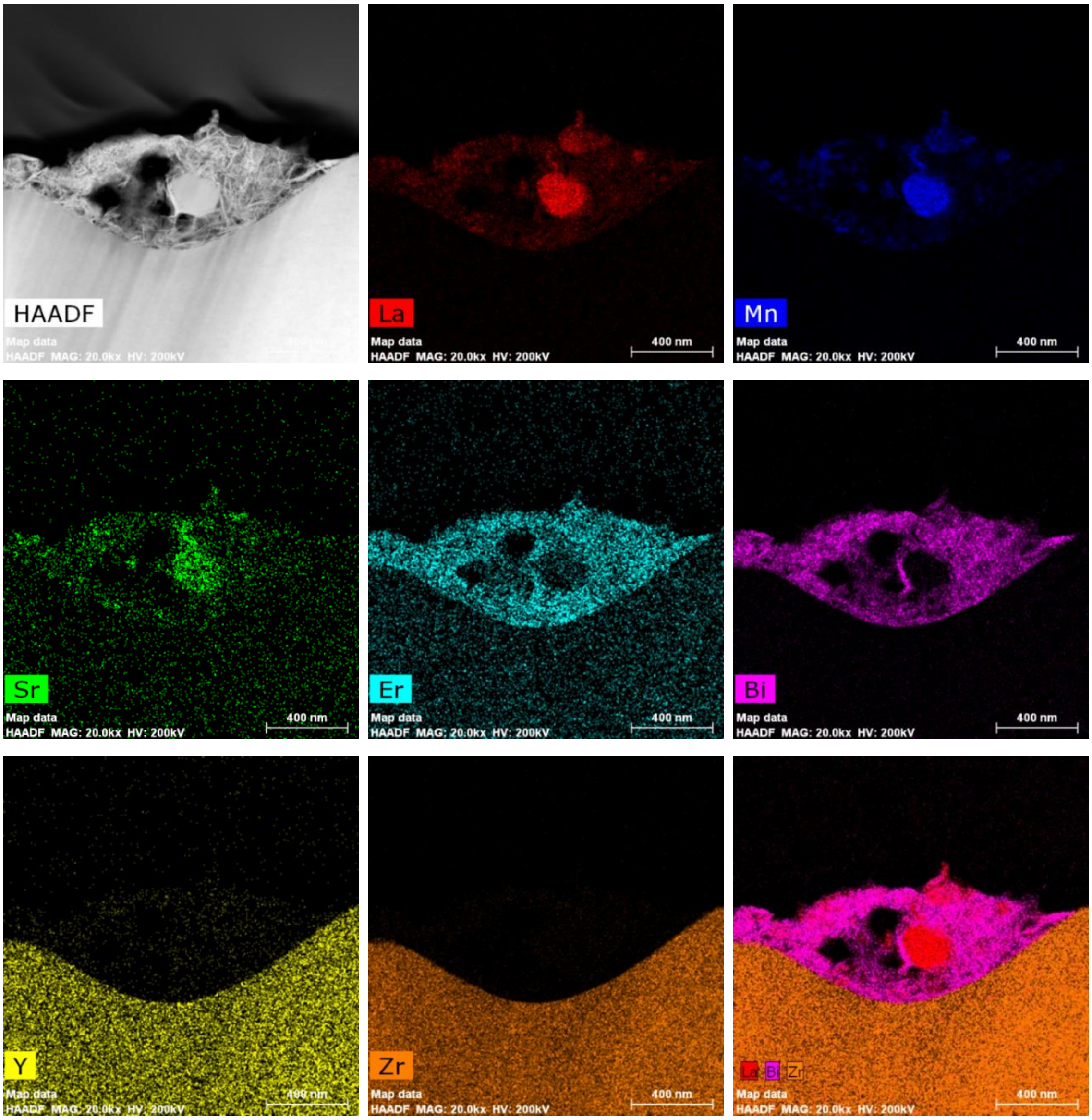

Figure 43 STEM-EDS maps of electrode/electrolyte interface after the directly assembled ESB decorated LSM cathode was polarized at 250 mA cm^{-2} and 700 °C for 20 h under electrolysis mode

In previous works[41], it is suggested that the gelation method tends to inhibit the agglomeration and growth of the cathode particles, avoiding the decrease of the active surface area that can be observed after the sintering of the separately synthetized ESB and LSM powders. From the images analysed, the cathode particles are smaller to the one of the previous case. As it was supposed, the observed enhancement of the electrocatalytic activity can be explained by the optimization of the microstructure of the composite cathode analysed in this section.

LSCF-ESB

Thermo-compatibility tests

After the test on LSM, it has been decided to focus on one of the most promising and studied perovskite material of the past years: LSCF. The LSCF and ESB powders were mixed mechanically in a mortar. The same thermo-compatibility test performed in the case of mixed LSM-ESB powder had been run for the LSCF-ESB couple of materials. The results of XRD analysis are shown in Figure 44. It is immediate to see that the two materials start reacting at 750 °C, showing peaks in the curves not expected by the crystal structure of LSCF and ESB. To avoid the formation of secondary phases formed by the reaction of the starting compounds, potentially detrimental for the performances of the cell, the electrochemical tests had been decided to be run at 700 °C.

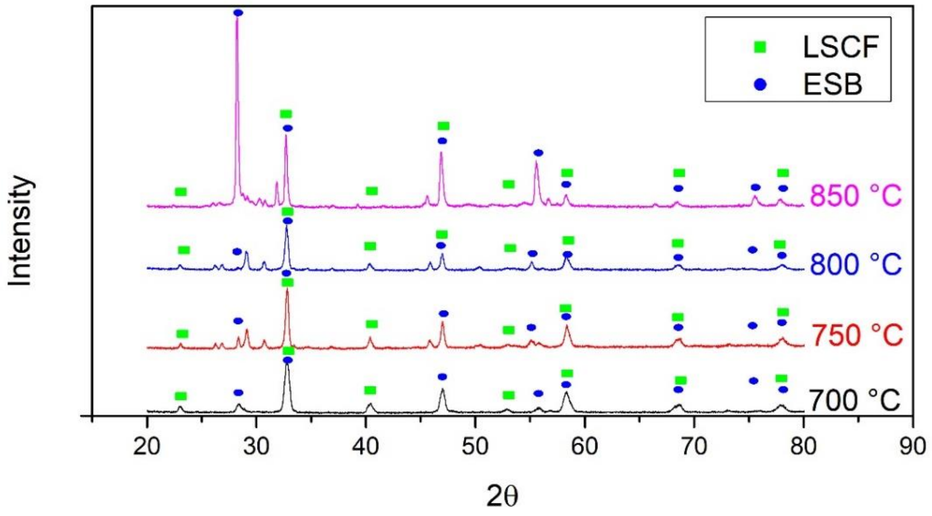

Figure 44 XRD patterns of the mixed LSCF-ESB powder

Electrochemical tests

The initial value of the overpotential and of the ohmic and polarization resistances of the LSCF-ESB composite cathode were lower than the one registered from the LSM-ESB composite cathode tests, confirming the better electrocatalytic properties of cobaltite-based material. However, the electrochemical tests gave not satisfactory results regarding the stability of the cathode performances during the operation. The Figure 45 and Figure 46 show the spectroscopic impedance curves and the polarization response of the LSCF-ESB composite cathode under 250 mA cm^{-2} and 500 mA cm^{-2} cathodic polarization. After an initial improvement, the performances of the cell worsened in both the ohmic resistance and the overpotential of the cathode. The higher current density caused a faster degradation, with the increase of the overpotential occurred before the first hour of polarization, while at lower current densities it decreased for the first 4 hours before degrading.

a)

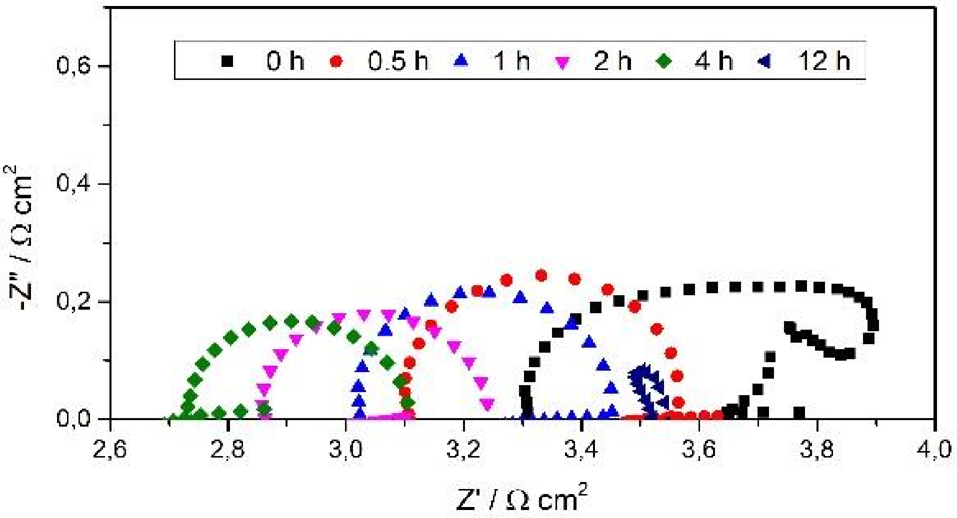

b)

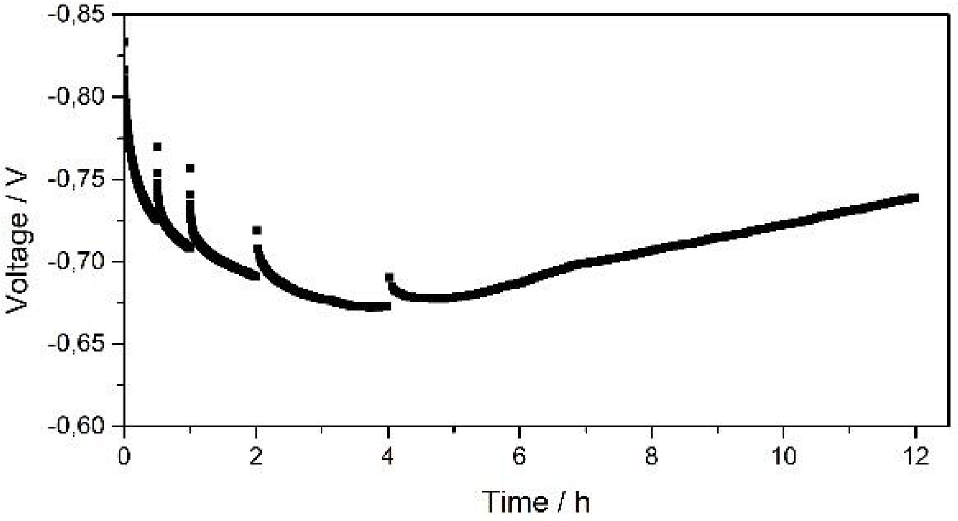

Figure 45 a) Impedance spectra and b) polarization response of direct assembled mixed LSCF-ESB cathode under cathodic polarization at 250 mA cm^{-2} and at 700 °C

a)

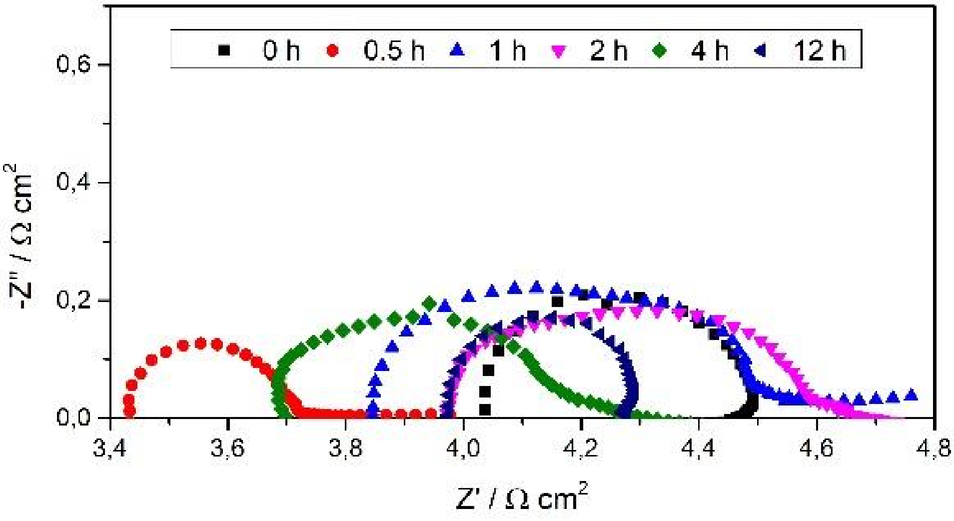

b)

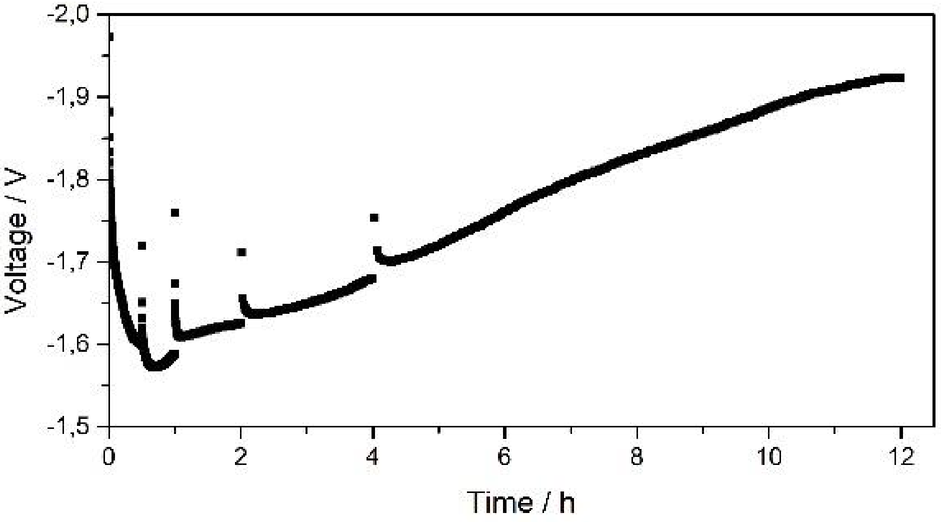

Figure 46 a) Impedance spectra and b) polarization response of direct assembled mixed LSCF-ESB cathode under cathodic polarization at 250 mA cm^{-2} and at 700 °C

The anodic polarization caused instead, right from the beginning of the test, a detrimental effect on the electrochemical behaviour of the cell. The ohmic resistances increased of the 29% and 35% respectively in the case of 250 mA cm^{-2} and 500 mA cm^{-2} current densities, while for the overpotential the increases were equal to around 20% and 27% respectively. The polarization resistances did not suffer such a dramatic degradation.

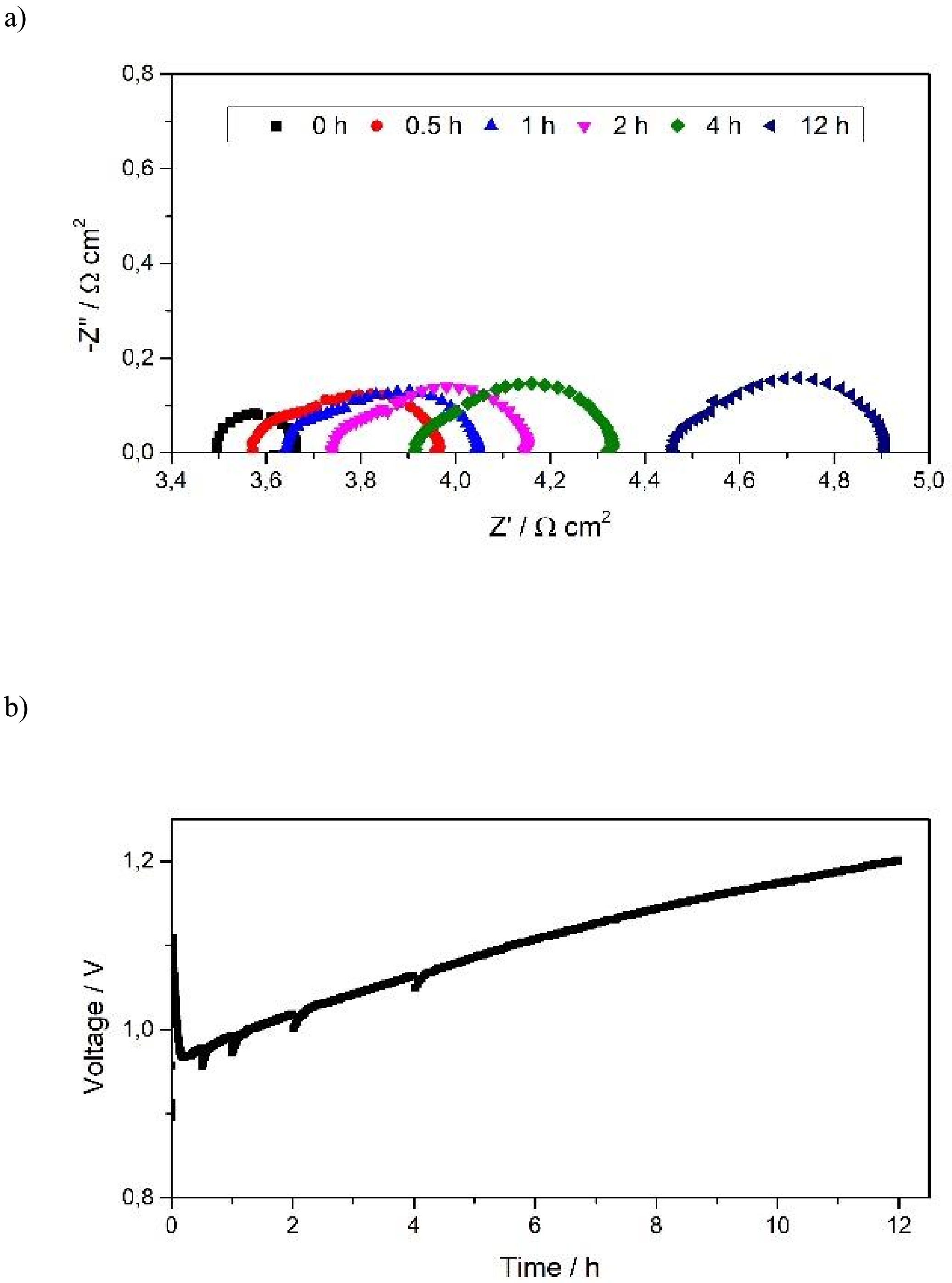

Figure 47 Impedance spectra and polarization response of direct assembled mixed LSCF-ESB cathode under anodic polarization at 250 mA cm^{-2} and at 700 °C

a)

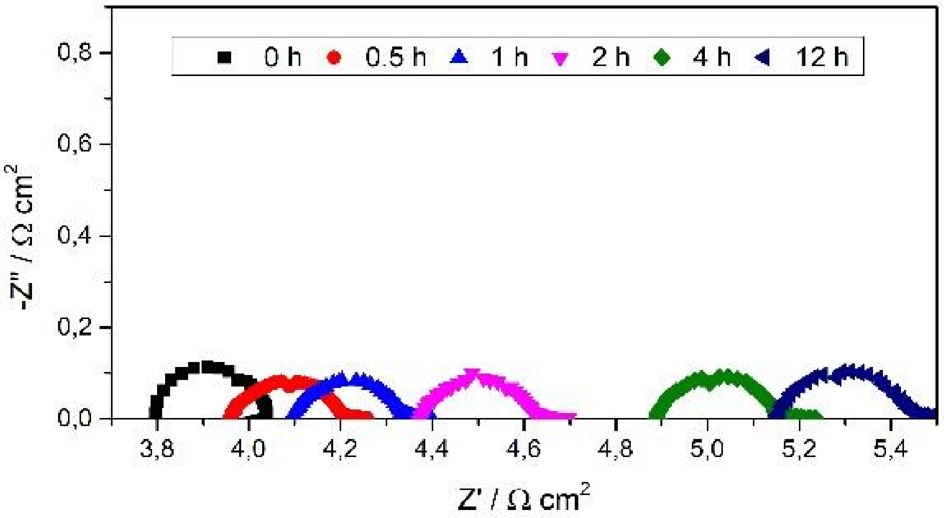

b)

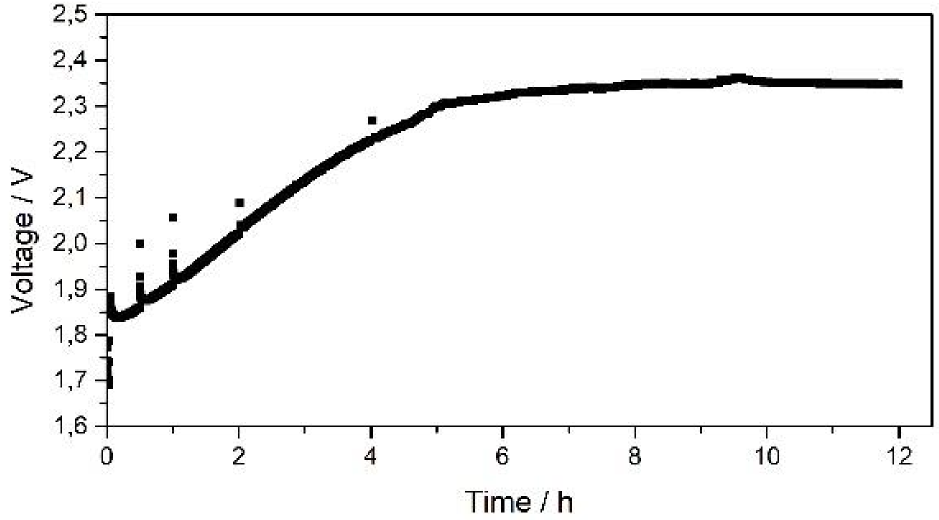

Figure 48 Impedance spectra and polarization response of direct assembled mixed LSCF-ESB cathode under anodic polarization at 500 mA cm^{-2} and at 700 °C

Observing the impedance response of the test under open circuit condition, the larger increase occurred to the ohmic resistance (+40% of the final R_Ω with respect to the one measured before the test) suggest that the more detrimental factor during the operation is the temperature, with the polarization, especially the cathodic one, playing a positive role in limiting the degradation of the resistances. In fact, the high difference in the value of the thermal expansion coefficient between the LSCF-ESB composite cathode and the YSZ pellet probably had cause the delamination between the applied electrode and the electrolyte, making the conduction of the ions through the electrolyte more difficult.

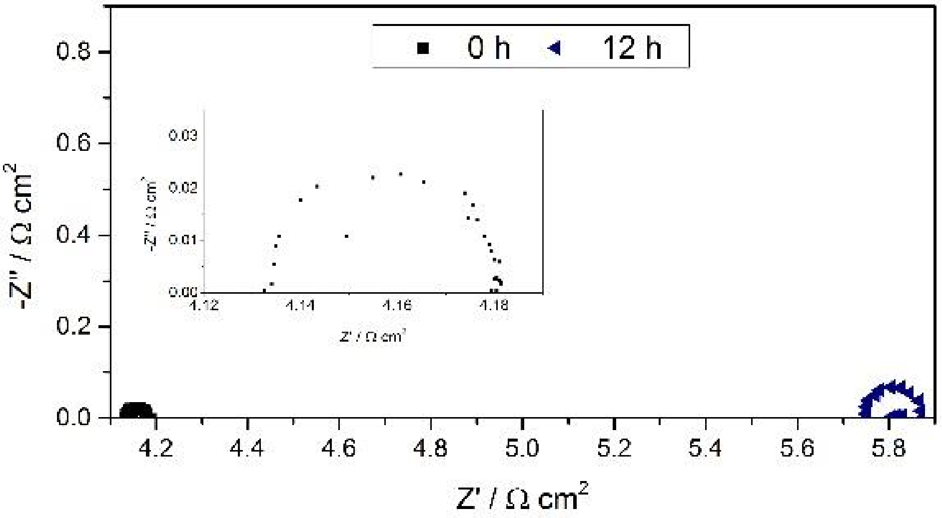

Figure 49 Impedance spectra of direct assembled mixed LSCF-ESB cathode under open circuit at 700 °C

Literature suggests that the worsening in the performances of the cathode, consisting the increase of the polarization resistance and of the overvoltage, is probably due to the thermally activated strontium segregation and its migration to the interface[43], forming a SrO layer detrimental for the performance of the cell. In fact, no chemical reactions are expected between LSCF and ESB at the testing temperature, as proved by the thermo-compatibility tests, and the strontium segregation due to the cell polarization has been observed also in *in situ* assembled cathode-cells[24]. An interesting development of this research can be the decoration of the LSCF bulk to see if a cover on the cathode can prevent the detrimental Sr segregation at the interface or adopting a B-sites doped LSCF, that does not suffer of the Sr segregation.

BSCF-ESB

Thermo-compatibility tests

The last couple of material to be tested was BSCF and ESB. The thermo-compatibility tests between the mixed powders, synthesized with the sol-gel method, were performed keeping the temperature at 600 °C, 650 °C and 700 °C for 2 hours. Figure 50 shows the XRD patterns of the composite powder after the test. The peaks of the curves representing the tests at 600 °C and at 650 °C show a good agreement with those of the pristine materials, indicating that ESB and BSCF are chemically stable at temperature below 650 °C. The two materials started to react at 700 °C, as can be observed from the additional peaks of the relative curve. To avoid the formation of secondary phases during the electrochemical tests, the half-cells with the BSCF-ESB directly assembled cathode were tested at 650 °C.

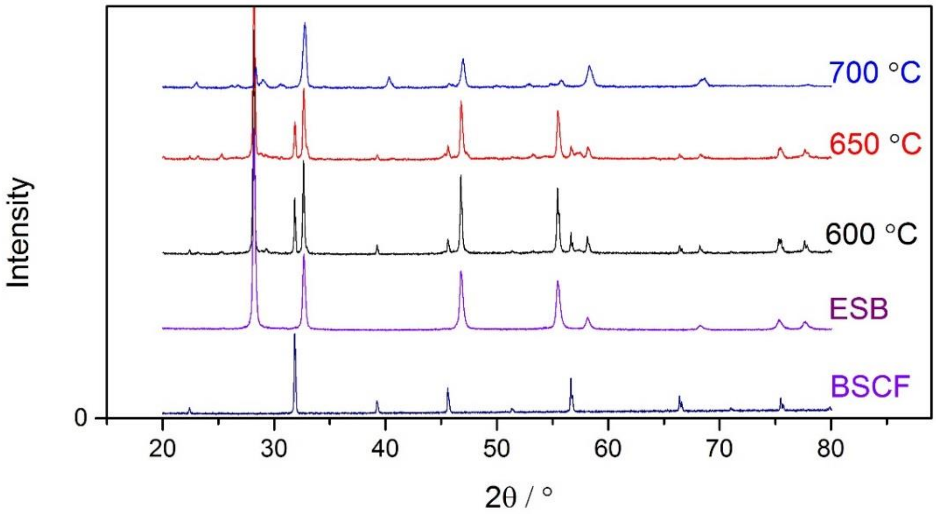

Figure 50 XRD patterns of the mixed BSCF-ESB powder

Electrochemical tests

The electrochemical performances under cathodic current densities of the directly applied mixed BSCF-ESB composite cathode, showed in Figure 51 and Figure 52, were promising and showed a good chemical compatibility between the materials, as expected after the thermo-compatibility tests. The cathodic polarization (i.e. the fuel cell mode) had a dramatic positive effect on the formation of an effective cathode/electrolyte as proved by the decrease of the 50% and of the 35% of the initial value of the ohmic resistance R_Ω due to the 250 mA cm^{-2} and 500 mA cm^{-2} current densities respectively, with a final value of 5 Ω cm^2 and 3.3 Ω cm^2 respectively. The cathodic polarization had a beneficial effect also on the polarization resistance of the cathode, with a decrease of 61% and a final value for R_p of 0.9 Ω cm^2 for 250 mA cm^{-2} current density and of 90% and 0.1 Ω cm^2 for 500 mA cm^{-2} current density. The behaviour of the polarization is characterized by an initial strong decrease followed by a constant value. The high difference in the values of the resistances may be caused by a not perfect preparation of the cell in the low-current density case.

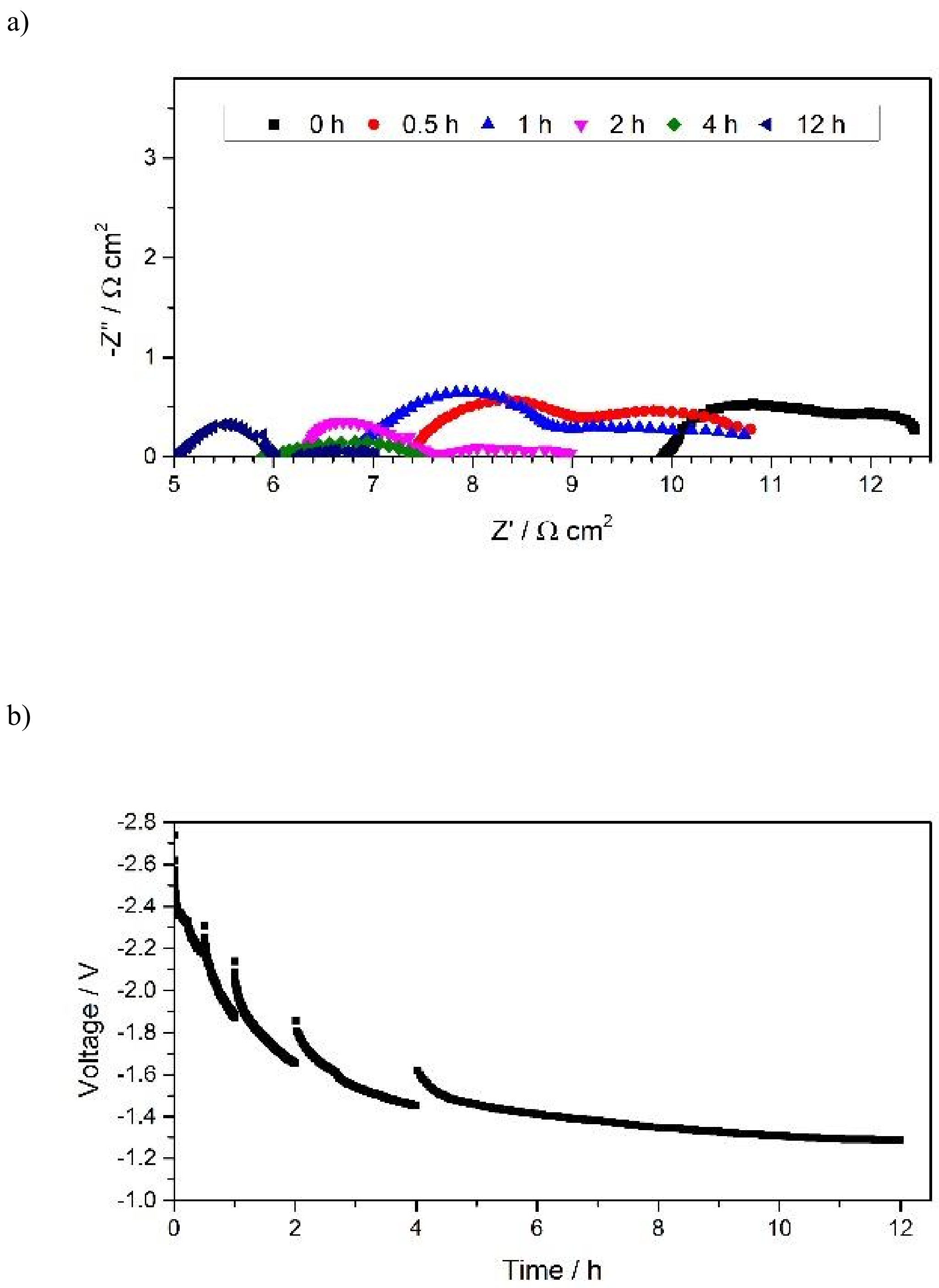

Figure 51 a) Impedance spectra and b) polarization response of direct assembled mixed BSCF-ESB cathode under cathodic polarization at 250 mA cm^{-2} and at 650 °C

a)

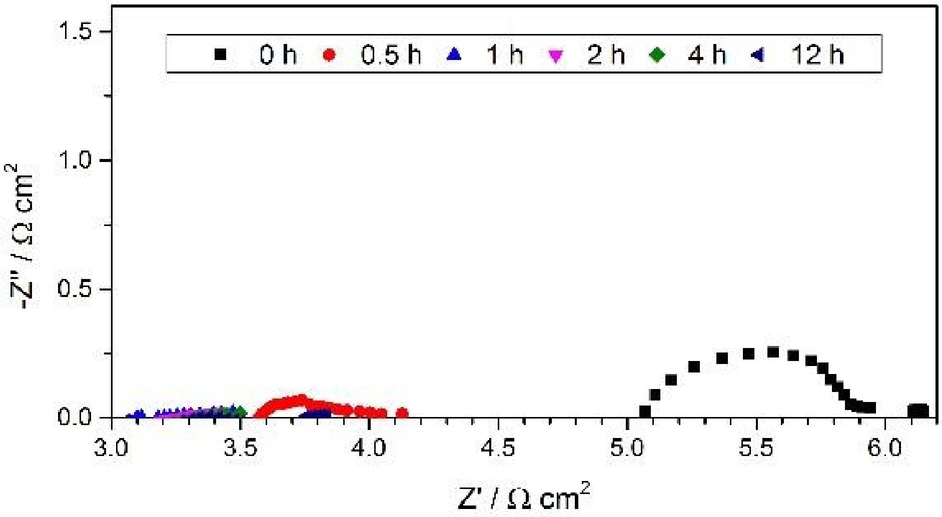

b)

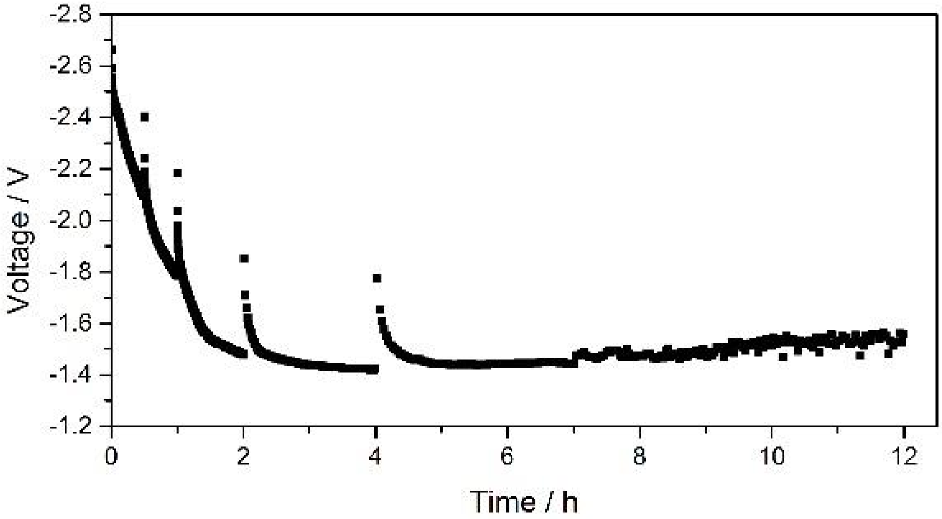

Figure 52 a) Impedance spectra and b) polarization response of direct assembled mixed BSCF-ESB cathode under cathodic polarization at 500 mA cm^{-2} and at 650 °C

Under electrolysis mode, the performance of the composite air electrode was poor and the behaviour were not stable. As it can be seen in Figure 53 and in Figure 54, the anodic polarization did not allow the formation of the electrode/electrolyte interface, since R_Ω did not decrease and its value was much higher than the previous case, with a final value of 6 Ω cm^2 and 7.4 Ω cm^2 in the case of 250 mA cm^{-2} and 500 mA cm^{-2} current densities respectively. Moreover, R_p and the polarization had a sensible increase during the test, especially at higher current densities, showing a worsening of the electrocatalytic activity of the cathode. This may be due to a chemical reaction between the cathode and the electrolyte or a cation segregation activated by the anodic polarization, since it has been proved that BSCF is not stable in a SOEC with YSZ as electrolyte[47] even if they are thermally compatible for temperature below 900 °C[48]. At this stage the mechanism of degradation of the performances in electrolysis mode is not clear and more investigation techniques to characterize the microstructure of the interface (e.g. FIB-STEM tests) are required.

a)

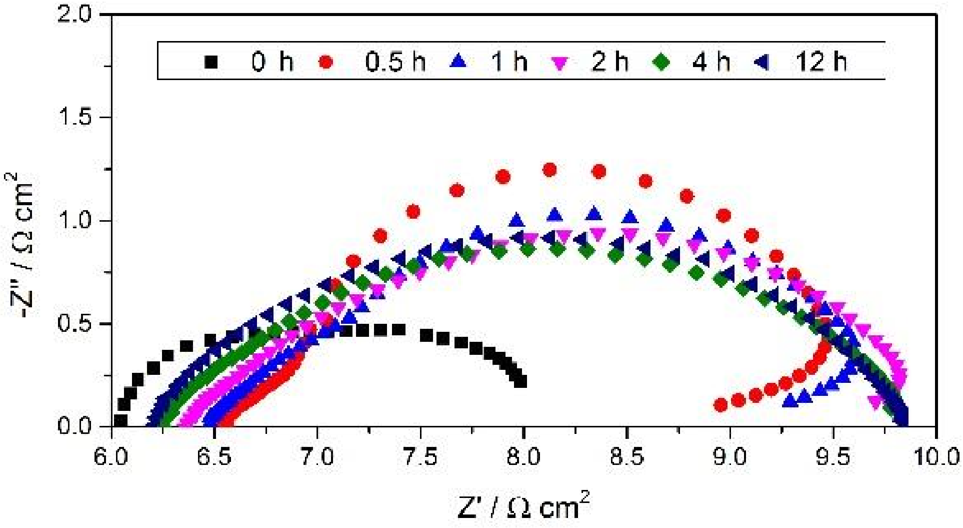

b)

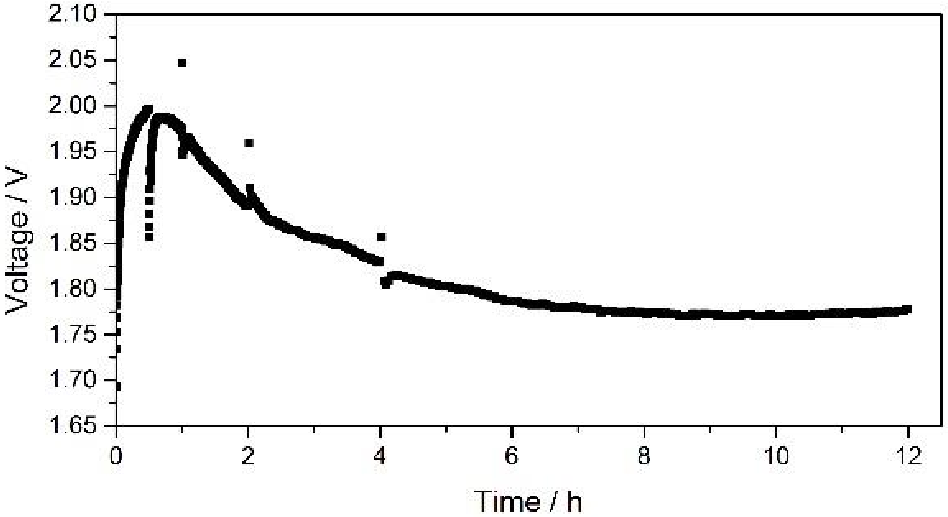

Figure 53 a) Impedance spectra and b) polarization response of direct assembled mixed BSCF-ESB cathode under anodic polarization at 250 mA cm^{-2} and at 650 °C

a)

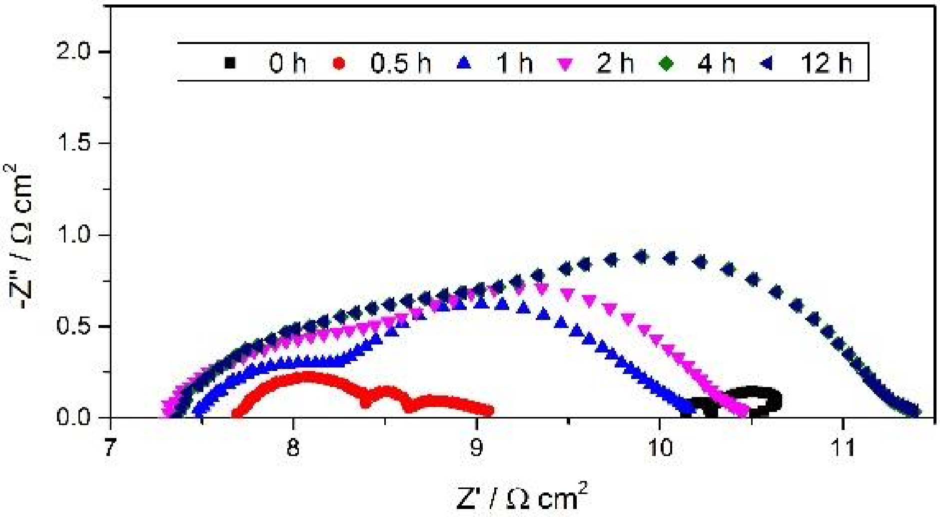

b)

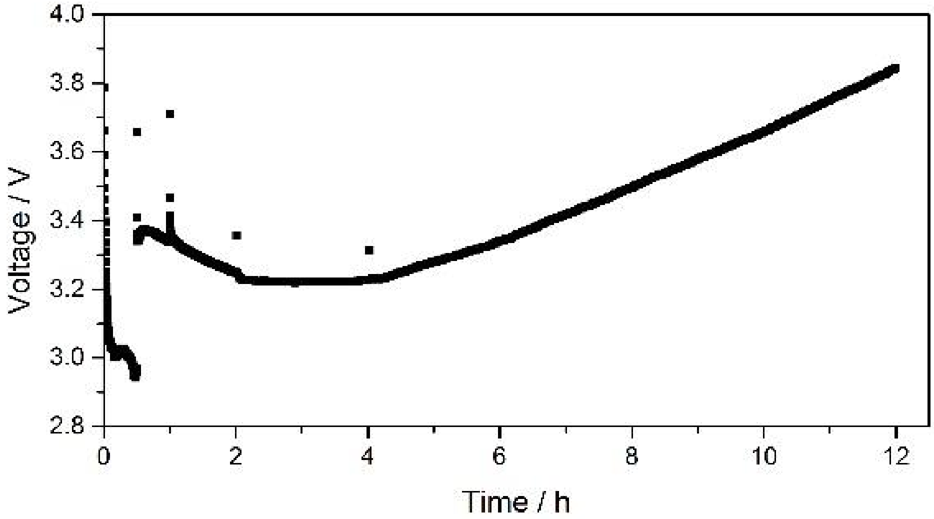

Figure 54 a) Impedance spectra and b) polarization response of direct assembled mixed BSCF-ESB cathode under anodic polarization at 500 mA cm^{-2} *and at 650 °C*

Even in open circuit condition, the temperature did not have a positive effect on the performance of the cathode, with an increase of the 100% of R_p. This behaviour may be due to the poor stability of the perovskite structure of BSCF at relatively low temperature.

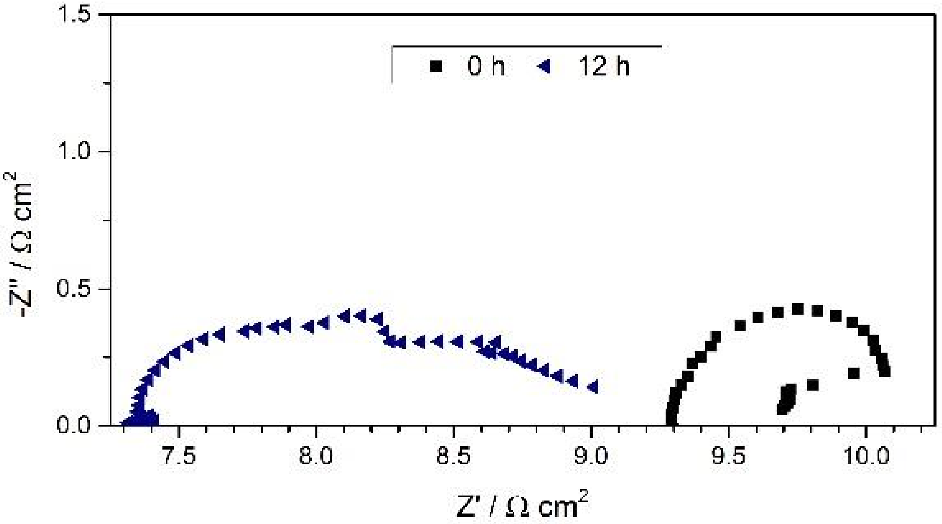

Figure 55 Impedance spectra of direct assembled mixed BSCF-ESB cathode under open circuit at 650 °C

ESB decorated BSCF

In order to improve the stability of BSCF cathode, especially under anodic polarization, the gelation process was adopted to decorate the porous BSCF backbone. In fact, a surface decoration had been reported to enhance the stability and the activity of BSCF cathode[49] and in general of many other cathodes[50–54], preventing a detrimental reaction between the cathode with other cell components, like the electrolyte. The coating of BSCF bulk avoids the direct contact between the two functional layers of the cell. Thanks to its excellent surface exchange properties, ESB can be a good choice as covering material. The gelation process avoids the non-uniform distribution and the high time-consuming process of the infiltration methods.

The electrochemical tests in fuel cell mode and electrolysis mode were performed at 650 °C, like those completed for the mixed BSCF-ESB cathodes.

Electrochemical tests

The electrochemical performances of the ESB decorated BSCF air electrodes working in fuel cell mode are shown in Figure 56 and Figure 57. The cathodic polarization instantaneously started to form an efficient electrode/electrolyte interface, decreasing the contact resistance between the two layers, with a reduction of the 50% and of the 30% in the case of 250 mA cm^{-2} and 500 mA cm^{-2} current densities respectively and final ohmic resistances R_Ω of 4 Ω cm^2 and 3.4 Ω cm^2 respectively, that can ascribed to the thick YSZ electrolyte layer and the contact resistances between the air electrode and the electrolyte and the external circuit. The cathodic polarization had a beneficial effect on the cathode performances as well, improving the intimate contact between the two materials composing the cathode. The final polarization resistance R_p at the end of the electrochemical tests in the two current conditions was 0.9 Ω cm^2 and 0.7 Ω cm^2 respectively, reasonable values at reduced temperatures that can be improved with a more sophisticated method to refine the synthetized BSCF particles size. The decoration method did not bring such a dramatic improvement in the electrode performances recorded in the case of the ESB decorated LSM cathode, probably because the ionic conducting properties of the BSCF were already extremely high and the more refined incorporation of the excellent ion conducting ESB did not affect in such a sensible manner the values of the polarization resistances and of the polarization response to the cathodic current. After an initial strong improvement, due to the decreasing of the ohmic and polarization resistances, the polarization response was well stable during the tests, without showing any degradation in the performances, as highlighted in Figure 56b and Figure 57b.

a)

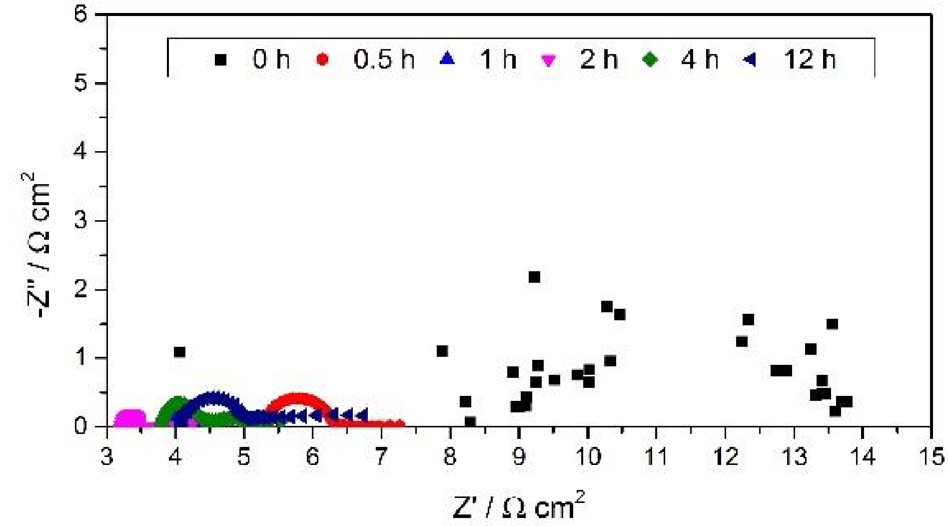

b)

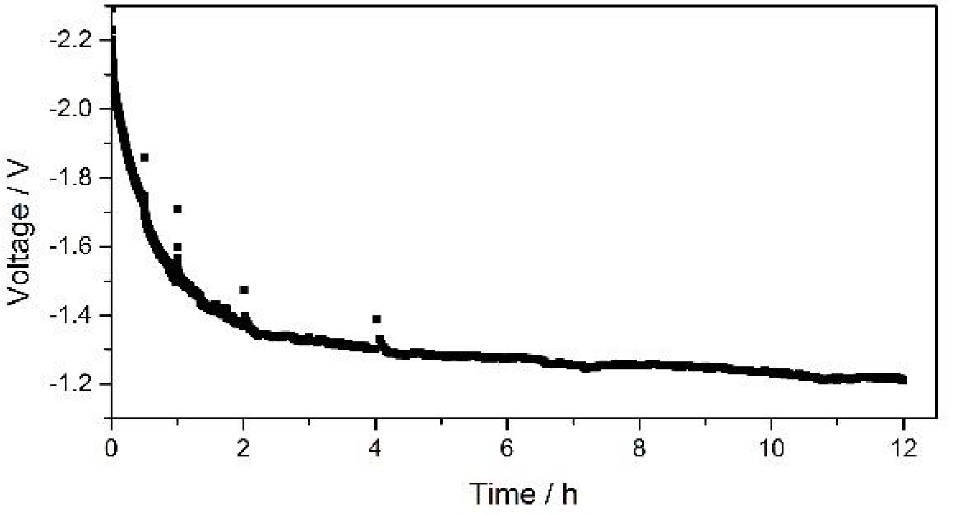

Figure 56 a) Impedance spectra and b) polarization response of direct assembled ESB decorated BSCF cathode under cathodic polarization at 250 mA cm^{-2} and at 650 °C

a)

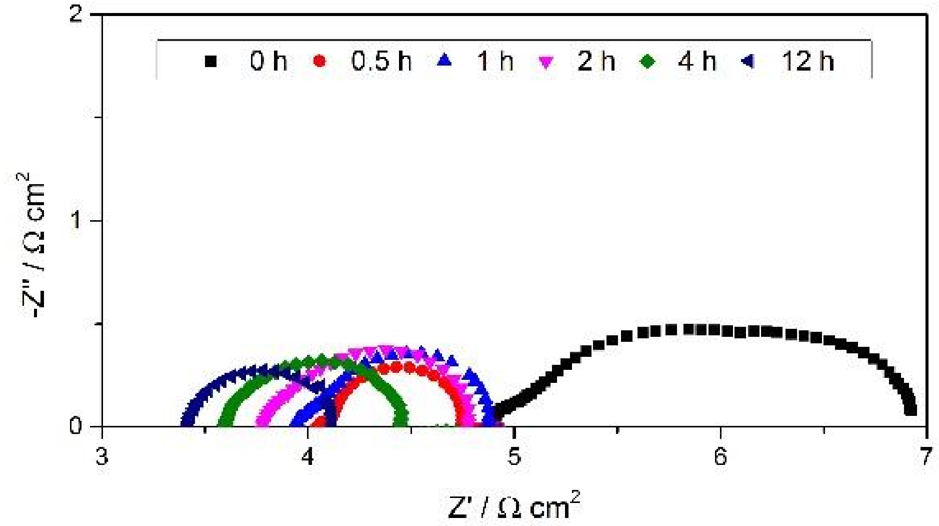

b)

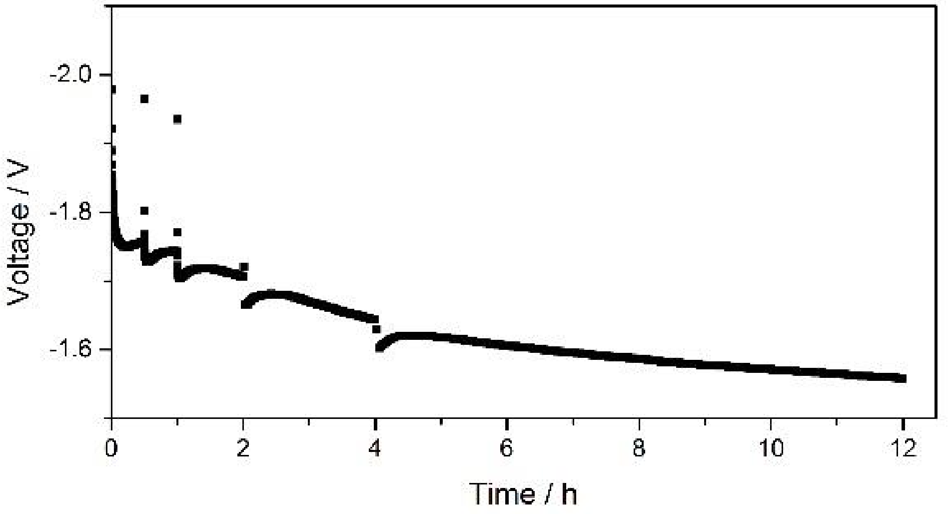

Figure 57 a) Impedance spectra and b) polarization response of direct assembled ESB decorated BSCF cathode under cathodic polarization at 500 mA cm^{-2} and at 650 °C

The improvements of the performances given by the application of the nanostructured and decorated electrode were visible after the electrochemical tests in electrolysis mode, under 250 mA cm^{-2} and 500 mA cm^{-2} anodic polarization. Figure 58b and Figure 59b show the polarization response decreasing and being stable during the tests, contrary to what it happened in the electrolysis mode testing of the mixed BSCF-ESB electrode, cf. Figure 53b and Figure 54b. The impedance spectra in Figure 58a Figure 59a showed that the polarization resistance R_p improved during the tests and reached the final value of 1 Ω cm^2 and 1.3 Ω cm^2 respectively. The ohmic resistance R_Ω decreased during the tests but the anodic polarization did not allow the formation of the proper electrode/electrolyte interface since the high final values of 6.3 Ω cm^2 and 8.4 Ω cm^2 respectively suggest a high contact resistance between the two layers.

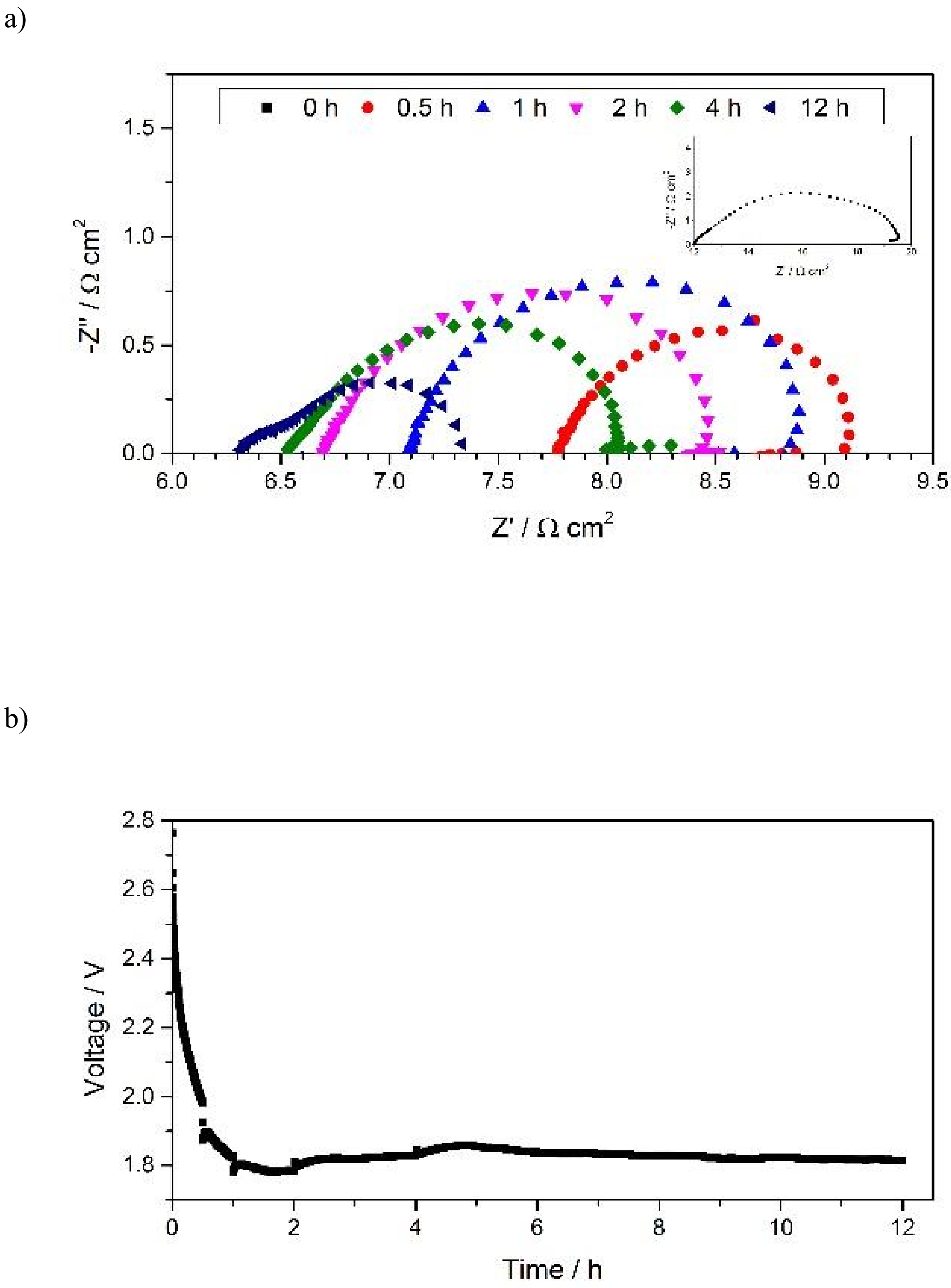

Figure 58 a) Impedance spectra and b) polarization response of direct assembled ESB decorated BSCF cathode under anodic polarization at 250 mA cm^{-2} and at 650 °C

a)

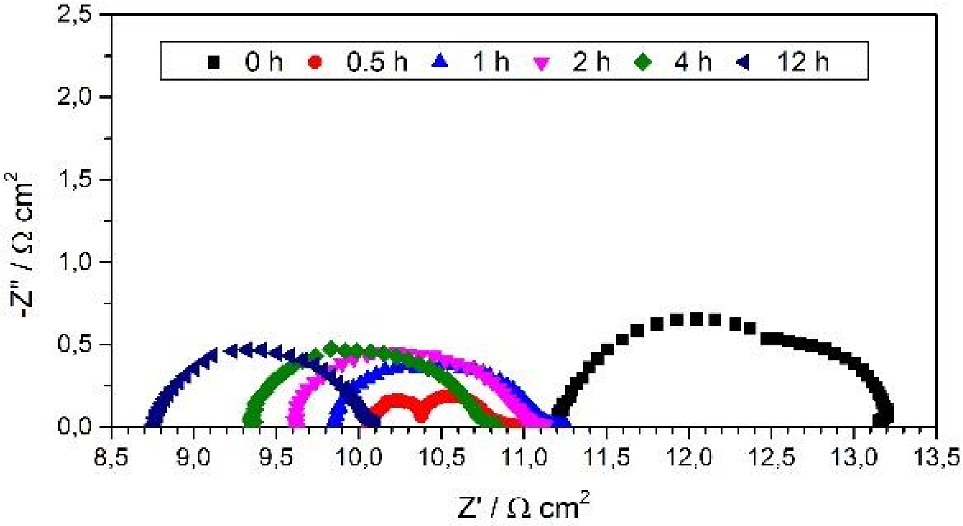

b)

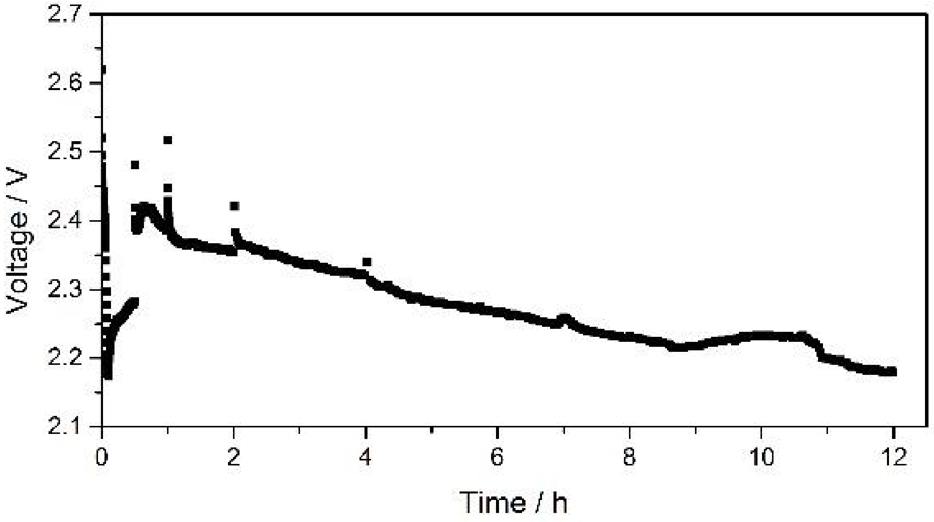

Figure 59 a) Impedance spectra and b) polarization response of direct assembled ESB decorated BSCF cathode under anodic polarization at 250 mA cm^{-2} and at 650 °C

Figure 60 shows the impedance curves of the ESB decorated BSCF cathode before and after a 12-hour electrochemical test in open circuit condition at 650 °C. Even in this case, the decoration of the cathode improved the stability of the electrode, since R_p remained quite constant during the test and did not showed the degradation registered in the case of the mixed composite cathode, even if the value did not improve like in the case analysed above: probably the polarization can improve the intimate contact between the two materials of the cathode. The high initial value of R_Ω due to the poor contact between the electrode and the electrolyte and to the not so excellent electron conductivity of BSCF improved during the test probably because the ESB partly diffused towards the interface thanks to its high mobility and facilitated the ionic migration through the electrolyte. Such a reduction is similar to the one observed during the electrolysis mode, suggesting that also in that case the improvement in the electronic conductivity was a consequence of the exposure of the composite cathode at high temperatures.

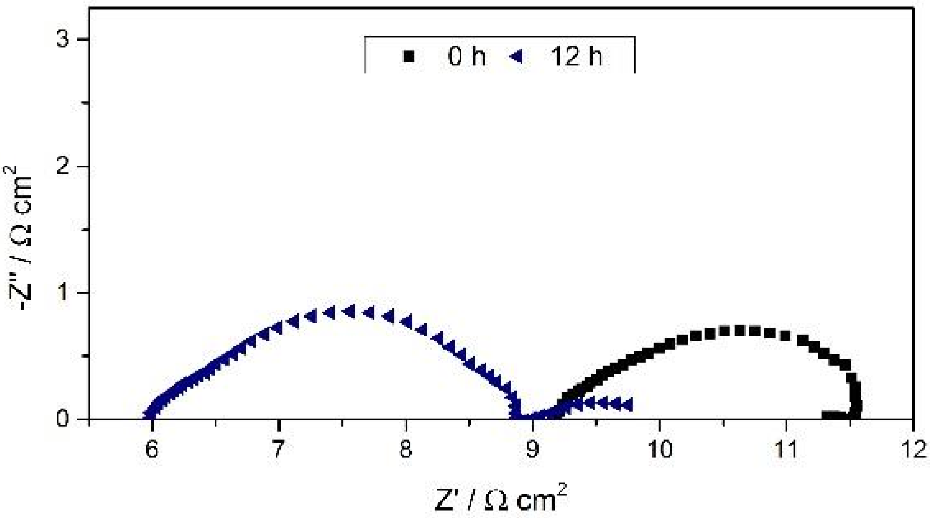

Figure 60 Impedance spectra of direct assembled ESB decorated BSCF cathode under open circuit at 650 °C

Microstructural Analysis

After the electrochemical tests, the electrode/electrolyte interface was analysed with the scanning electron microscope. From Figure 61 where the SEM images at different resolution of the electrolyte surface after the removal of the cathode by adhesive tape of the half-cell polarized with 250 mA cm^{-2} cathodic current are shown, it is possible to see the morphology of the cathode from the particles left on the grains of the electrolyte surface. The cathode particles are relatively small, in the order of hundreds of nm, and quite randomly and homogeneously distributed on all over the electrolyte surface, proving that the nanostructured electrode was formed adopting the decoration method. As in the previous case, the enhanced active surface of the cathode due to this fabrication process allow very high performances at reduced temperature, as described above during the analysis of the electrochemical tests.

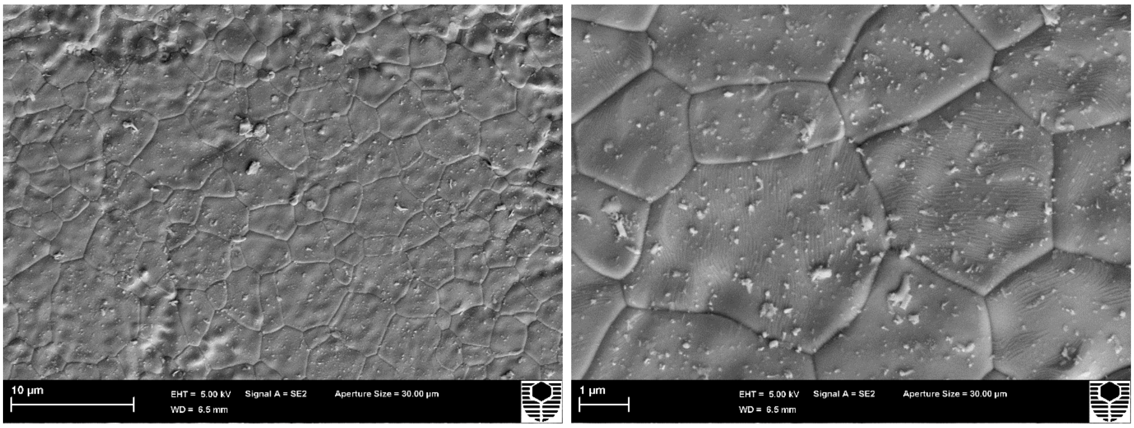

Figure 61 SEM images at different resolution of the YSZ surface after 12-hour cathodic polarization at 250 mA cm^{-2} and removal of the direct applied ESB decorated BSCF cathode by adhesive tape

The particles of the composite cathode are completely by the hydrochloric acid treatment, as it can be seen from the clean and smooth surface of the YSZ layer shown in the SEM images in Figure 62 relative to the half-cell tested under 12-hour cathodic polarization. Moreover, any polarization-induced contact mark is clearly visible on the electrolyte surface.

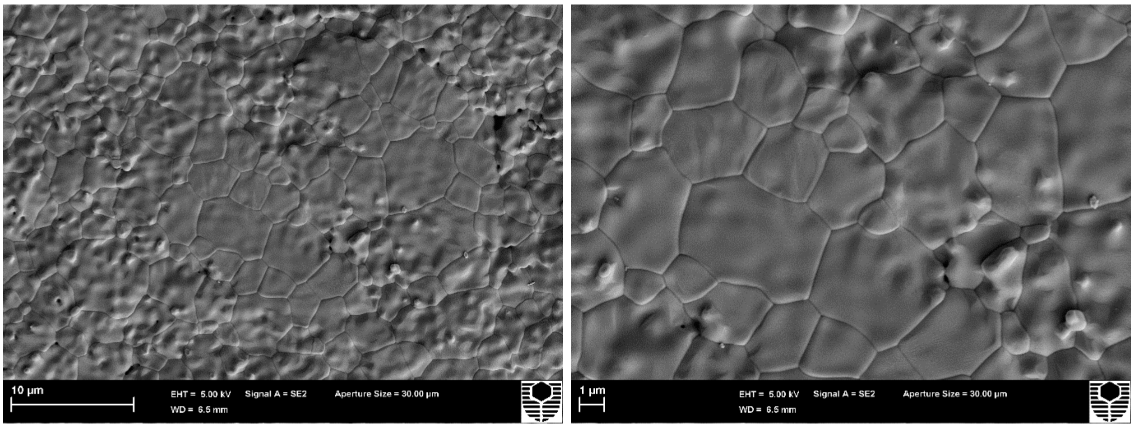

Figure 62 SEM images at different resolution of the YSZ surface after 12-hour cathodic polarization at 250 mA cm^{-2} and removal of the direct applied ESB decorated BSCF cathode by acid treatment

Even in the case of the air electrode polarized by the anodic current, the particles are in the order of hundreds of nm and spread randomly on all over the electrolyte surface, as it can be seen from the SEM images of the anodic polarized half-cell shown in Figure 63 after the removal of the cathode by adhesive tape. The dimension of the BSCF particles, that act as backbone for the composite cathode, and thus the global morphology of the electrode can be further improved with simple but effective mechanical particles refinement processes (e.g. the ball milling).

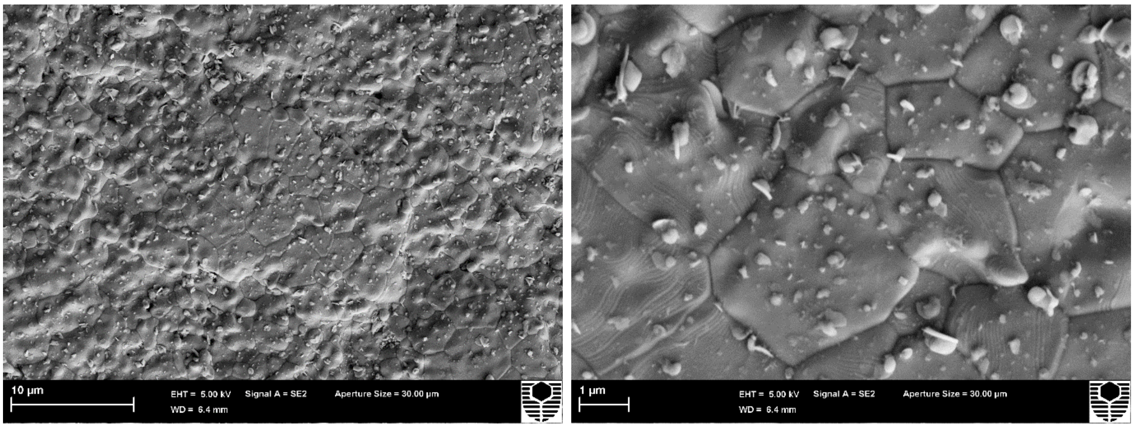

Figure 63 SEM images at different resolution of the YSZ surface after 12-hour anodic polarization at 250 mA cm^{-2} and removal of the direct applied ESB decorated BSCF cathode by adhesive tape

From the SEM images of YSZ surface of the anodic polarized half-cell after the acid treatment shown in Figure 64, any induced contact mark or layer is present on the surface, indicating the improved chemical compatibility between the materials due to the covering of the BSCF backbone with the ESB phase, that prevents the direct contact between the BSCF and the YSZ and their reaction during flow of the anodic current, as described above. The absence of contact marks between the electrolyte and the cathode, and thus a so-intimate contact between the two functional layers as observed in the case of the ESB decorated LSM cathode, can explain the higher ohmic resistances recorded during the electrochemical tests, in addition to the not-excellent electronic conductive properties of BSCF and ESB.

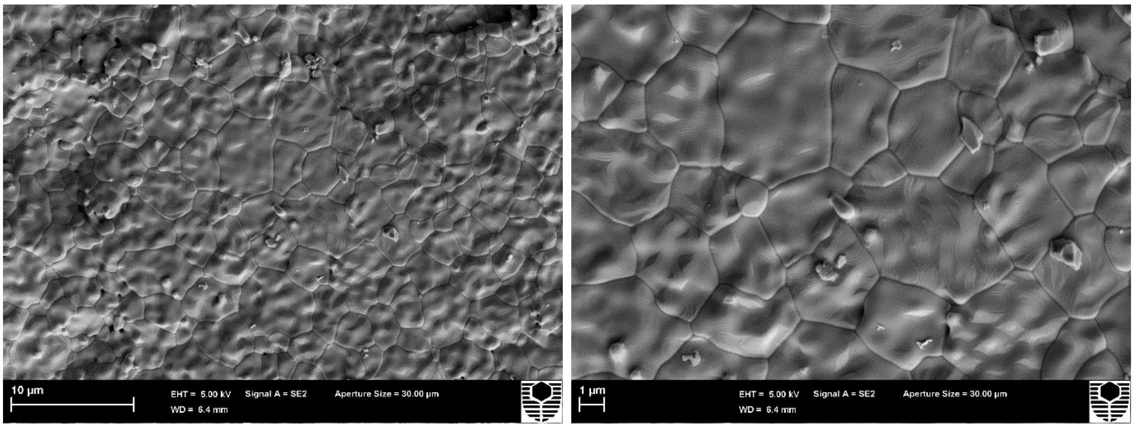

Figure 64 SEM images at different resolution of the YSZ surface after 12-hour anodic polarization at 250 mA cm^{-2} and removal of the direct applied ESB decorated BSCF cathode by acid treatment

The decoration process allowed the fabrication of a BSCF electrode characterized by an improved microstructure, as proved by the analysis of the images of the electrolyte surface recorded with the scanning electron microscope. The improved morphology of the porous electrode through the gelation process proved a sensible improvement of the stability of the performance of this component, especially in the electrolysis operation. A better understanding of the mechanism of the processes occurred in the so-prepared cathode can be reached by a microstructural characterization with the elemental mapping of the interface with FIB-STEM images and further electrochemical tests. These images could highlight if the ESB phase was properly formed in the porous structure of BSCF backbone and to investigate the BSCF structure stability under the test conditions.

The following step of this research can be the testing of the ESB decorated BSCF cathode directly applied on a full cell to investigate if the decoration of the surface of the cathode can improve the long-term stability of this material and avoid the degradation due to the reaction with the CO_2 in air and to the formation of the carbonate, one of the most challenging issues and limiting factor in the development of efficient cathodes made by this material. In order to reach competitive performance of the full cell at temperature below 700 °C, the thickness electrolyte layer must be reduced with the most updated fabrication process or the YSZ must be replaced with other materials more performant in this range of temperatures (e.g. with SDC[55]), and the particle dimension of BSCF must be improved with refinement techniques.

CONCLUSIONS

In this study, the electrochemical behaviour in the first 12 hours of polarization of LSM, LSCF and BSCF composite with an excellent ion conductive phase (ESB) cathodes were investigated, both in fuel cell and electrolysis mode. At first, the thermal compatibility between the materials was tested, proving the chemical stability of the materials at the SOFC operating temperature: ESB and LSM were stable at all the test temperatures (below 850 °C), LSCF and ESB at temperatures below 700 °C and BSCF and ESB at temperatures below 650°C. Then, according to the results of the thermo-compatibility tests, the composite cathodes were in situ assembled on YSZ pellets and electrochemically tested under five different polarization conditions. As expected, especially the cathodic polarization helped to form an effective electrode/electrolyte interface in the first 2 hours of the test, as proved by the strong decrease of the ohmic resistances, measures of the contact resistances between the two layers. In the case of LSM-ESB cathodes, the polarization caused visible contact marks on the YSZ surface. The ESB phase tended to occupy the interface between LSM and YSZ, due to its high wettability and lower melting temperature that helped its migration. For these reasons, it is reasonable to assess that the contact marks on the YSZ surface acted as bridges for the ion migration from the electrode to the electrolyte and vice versa, improving the quality of the interface. Moreover, the polarization improved the intimate contact between the particles constituting the composite electrode, as the observed improvements in the cathodes performances during the operation suggest. The ohmic resistances at the end of the anodic polarization were higher than those recorded after the cathodic polarization, indicating that the anodic current does not form an optimal electrode/electrolyte interface.

The mechanical mixed LSM-ESB cathodes showed an excellent stability in the performances, especially during the fuel cell mode. The final polarization resistances were about 0.4 Ω cm2, less than one third of that recorder for the pristine LSM cathode in the same configuration but at 800 °C, indicating the great enhancement in the performances that can cause a properly chosen second phase in a composite electrode. However, the microscopic characterization of the cells tested showed a non-optimized morphology and phase distribution of the cathodes, characterized by a non-homogeneous size of the particles (with some ESB particles bigger than 1 μm) and well-defined by a phase separation between LSM and ESB, reducing in this way the active surface for the oxygen reduction reaction.

The mixed BSCF-ESB cathodes showed excellent performances in fuel cell mode as well, reaching polarization resistances of 0.1 Ω cm2 at 650°C. Nevertheless, the operation in electrolysis mode was not stable, due to phenomena and reactions between the materials that are not clear at this stage of the study and that require a more detail microstructural characterization.

On the contrary as recorded for the other two materials, the mixed LSCF and ESB cathodes performed badly, showing a degradation during the 12-hour tests, probably due to the Sr segregation and the resulting formation of a detrimental SrO layer at the interface as reported in literature. It would be interesting to study if an ESB coating of LSCF cathode would block this phenomenon and stabilize the performances, or alternatively, to substitute the pristine LSCF with a more stable B-site doped LSCF (e.g. LSCFNb).

The gelation approach allowed to synthetize a nanostructured composite cathode in a simple and effective way. In fuel cell mode, the decoration of the cathode greatly enhanced the performances of LSM, reducing the polarization resistances up to 0.06 Ω cm2, while it did not have the same effect on BSCF, probably because BSCF is already an excellent oxygen ion conductor and the good conductive properties of ESB does not affect in such a sensible way the performance of this material. In the electrolysis mode instead, the behaviours of both LSM and BSCF based cathode became much more stable as compared to those observed during the polarization of the mechanically mixed cathodes. The microstructural characterization after the tests of the ESB decorated LSM cathode proved the success in the preparation of the nanostructured cathode, since a finer, more porous and more homogeneous structure has been observed, and it was more difficult to distinguish the particles of the two phases, with the ESB occupying the pore of the LSM backbone.

On summary, this study proved the great improvements that the introduction of the ESB phase can cause to the pristine cathodes: in the case of LSM we observed a sensible reduction in the polarization resistances and the feasibility of the materials at lower operating temperature; in the case of BSCF the enhanced stability of the behaviour of the cathode under polarization. Moreover, the beneficial effects of a nanostructured cathode fabricated with a simple gelation approach has been demonstrated, with enhanced and more stable performances, especially in electrolysis mode. At last, the results obtained give a further prove of the effectiveness of the *in situ* approach as fabrication method for cathodes of SOFCs. Further investigations on the same cathodes applied on NiO anode supported cells can demonstrate and quantify the feasibility of LSM-based cathodes on cells at temperatures below 700 °C and to study that the effect of the ESB decoration has on the degradation of BSCF due to the reaction with the CO_2 of air.

REFERENCES

1. European Commission. COMMUNICATION FROM THE COMMISION: A Roadmap for moving to a competitive low carbon economy in 2050. *COM(2011) 112 Final* **34,** 1–34 (2011).
2. Milewski, J., Swirski, K., Santarelli, M. & Leone, P. *Advanced Methods of Solid Oxide Oxide Fuel Cell Modeling*. (2011). doi:10.1007/978-0-85729-262-9
3. Singhal, S. C. & Kendall, K. *High Temperature Solid Oxide Fuel Cells: Fundamentals, Design and Applications*. *Advanced Materials & Processes* **161,** (2003).
4. McPhail, S., Leto, L. & Boigues-Muñoz, C. *The Yellow Pages of SOFC Technology - International Status of SOFC deployment 2012-2013*. *Enea* (2013).
5. Sharaf, O. Z. & Orhan, M. F. An overview of fuel cell technology: Fundamentals and applications. *Renew. Sustain. Energy Rev.* **32,** 810–853 (2014).
6. Huneke, F. AUF DEM WEG IN DIE W ETTBEWERBSFÄHIGKEIT: ELEKTROLYSEGASE ERNE UERBAREN URSPRUNGS. *Eur. Grundrechte EuGRZ* (2018).
7. Larminie, J. & Dicks, A. *Fuel cell systems explained*. *Fuel* (2003). doi:10.1002/9781118878330
8. O'hayre, Ryan Cha, Suk-Won Colella, Whitney G. Prinz, F. B. Fuel Cell Fundamentals (3rd Edition). *John Wiley Sons* (2016).
9. Pasricha, S., Keppler, M., Shaw, S. & Nehrir, M. H. *Comparison and Identification of Static Electrical Terminal Fuel Cell Models*. *Energy Conversion, IEEE Transactions on* **22,** (2007).
10. Santarelli, M. Appunti delle lezioni del corso di Poly-generation and Advance Energy Systems. (2016).
11. Tarancón, A. Strategies for lowering solid oxide fuel cells operating temperature. *Energies* **2,** 1130–1150 (2009).
12. Santarelli, M. Celle a combustibile a ossidi solidi (SOFC). Descrizione generale della cella e dei suoi principi di funzionamento. *Appunti del corse Poly-generation Adv. energy Syst.* 1–42 (2016).
13. Nozawa, K., Orui, H. & Komatsu, T. Development of Highly Efficient Planar Solid Oxide Fuel Cells. *Ntt Tech. Rev.* **6,** 1–8 (2008).
14. Jiang, S. P. & Li, J. 3 Cathodes. **2,** (2009).
15. Adler, S. B. Factors governing oxygen reduction in solid oxide fuel cell cathodes. *Chem. Rev.* **104,** 4791–4843 (2004).
16. Fleig, J. Solid Oxide Fuel Cell Cathodes: Polarization Mechanisms and Modeling of the Electrochemical Performance. *Annu. Rev. Mater. Res.* **33,** 361–382 (2003).

17. Zhou, W., Ran, R. & Shao, Z. Progress in understanding and development of Ba0.5Sr0.5Co0.8Fe0.2O3-δ-based cathodes for intermediate-temperature solid-oxide fuel cells: A review. *J. Power Sources* **192,** 231–246 (2009).

18. Kilner, J. A. & Burriel, M. Materials for Intermediate-Temperature Solid-Oxide Fuel Cells. *Annu. Rev. Mater. Res.* **44,** 365–393 (2014).

19. Jiang, S. P. Development of lanthanum strontium manganite perovskite cathode materials of solid oxide fuel cells: A review. *Journal of Materials Science* **43,** (2008).

20. Jiang, S. A comparison of O 2 reduction reactions on porous (La, Sr) MnO 3 and (La, Sr)(Co, Fe) O 3 electrodes. *Solid State Ionics* **146,** 1–22 (2002).

21. Liu, M. Equivalent Circuit Approximation to Porous Mixed-Conducting Oxygen Electrodes in Solid-State Cells. *J. Electrochem. Soc.* **145,** 142 (1998).

22. Mahato, N., Banerjee, A., Gupta, A., Omar, S. & Balani, K. Progress in material selection for solid oxide fuel cell technology: A review. *Prog. Mater. Sci.* **72,** 141–337 (2015).

23. Baharuddin, N. A., Rahman, H. A., Muchtar, A., Sulong, A. B. & Abdullah, H. Development of lanthanum strontium cobalt ferrite composite cathodes for intermediate- to low-temperature solid oxide fuel cells. *Journal of Zhejiang University SCIENCE A* **14,** (2013).

24. Chen, K. *et al.* Direct application of cobaltite-based perovskite cathodes on yttria-stabilized zirconia electrolyte for intermediate temperature solid oxide fuel cells. *J. Mater. Chem. A* **0,** (2016).

25. Chen, K. *et al.* Polarization-induced interface and Sr segregation of in situ assembled La0.6Sr0.4Co0.2Fe0.8O3-δ electrodes on Y2O3-ZrO2 electrolyte of solid oxide fuel cells. *ACS Applied Materials and Interfaces* **8,** (2016).

26. Ai, N. *et al.* Highly Stable Sr-Free Cobaltite-Based Perovskite Cathodes Directly Assembled on a Barrier-Layer-Free Y2O3-ZrO2 Electrolyte of Solid Oxide Fuel Cells. *ChemSusChem* **10,** (2017).

27. Lee, S., Lim, Y., Lee, E. A., Hwang, H. J. & Moon, J. W. Ba0.5Sr0.5Co0.8Fe0.2O3-δ(BSCF) and La0.6Ba0.4Co0.2Fe0.8O3-δ(LBCF) cathodes prepared by combined citrate-EDTA method for IT-SOFCs. *J. Power Sources* **157,** 848–854 (2006).

28. Liu, Q. L., Khor, K. A. & Chan, S. H. High-performance low-temperature solid oxide fuel cell with novel BSCF cathode. *J. Power Sources* **161,** 123–128 (2006).

29. Chen, Z., Ran, R., Zhou, W., Shao, Z. & Liu, S. Assessment of Ba0.5Sr0.5Co1-yFeyO3-δ(y = 0.0-1.0) for prospective application as cathode for IT-SOFCs or oxygen permeating membrane. *Electrochim. Acta* **52,** 7343–7351 (2007).

30. Wei, B. *et al.* Thermal and Electrical Properties of New Cathode Material Ba[sub 0.5]Sr[sub 0.5]Co[sub 0.8]Fe[sub 0.2]O[sub 3−δ] for Solid Oxide Fuel Cells. *Electrochem. Solid-State Lett.* **8,** A428 (2005).

31. Yan, A., Yang, M., Hou, Z., Dong, Y. & Cheng, M. Investigation of Ba1−xSrxCo0.8Fe0.2O3−δ as cathodes for low-temperature solid oxide fuel cells both in the absence and presence of CO2. *J. Power Sources* **185,** 76–84 (2008).

32. Švarcová, S., Wiik, K., Tolchard, J., Bouwmeester, H. J. M. & Grande, T. Structural instability of cubic perovskite BaxSr1 − xCo1 − yFeyO3 − δ. *Solid State Ionics* **178,** 1787–1791 (2008).

33. Li, J. *et al.* La0.84Sr0.16MnO3-δcathodes impregnated with Bi1.4Er0.6O3for intermediate-temperature solid oxide fuel cells. *J. Power Sources* **194,** 625–630 (2009).

34. Wachsman, E. D. & Lee, K. T. Lowering the Temperature of Solid Oxide Fuel Cells. *Science (80-.).* **334,** 935–939 (2011).

35. Kan, C. C., Kan, H. H., Van Assche, F. M., Armstrong, E. N. & Wachsman, E. D. Investigating Oxygen Surface Exchange Kinetics of La[sub 0.8]Sr[sub .20]MnO[sub 3-δ] and La[sub 0.6]Sr[sub 0.4]Co[sub 0.2]Fe[sub 0.8]O[sub 3-δ] Using an Isotopic Tracer. *J. Electrochem. Soc.* **155,** B985 (2008).

36. Lee, K. T., Lidie, A. A., Yoon, H. S. & Wachsman, E. D. Rational Design of Lower-Temperature Solid Oxide Fuel Cell Cathodes via Nanotailoring of Co-Assembled Composite Structures. *Angew. Chemie Int. Ed.* **53,** 13463–13467 (2014).

37. Mitterdorfer, A. & Gauckler, L. J. La2Zr2O7 formation and oxygen reduction kinetics of the La0.85Sr0.15MnyO3, O2(g)|YSZ system. *Solid State Ionics* **111,** 185–218 (1998).

38. Jiang, S. P. Thermally and Electrochemically Induced Electrode/Electrolyte Interfaces in Solid Oxide Fuel Cells: An AFM and EIS Study. *Journal of The Electrochemical Society* **162,** (2015).

39. Chen, K. *et al.* In situ assembled La0.8Sr0.2MnO3 cathodes on aY2O3–ZrO2 electrolyte of solid oxide fuel cells – interface and electrochemical activity. *J. Mater. Chem. A* **8,** (2016).

40. Chen, K., Liu, S.-S., Ai, N., Koyama, M. & Jiang, S. P. Why solid oxide cells can be reversibly operated in solid oxide electrolysis cell and fuel cell modes? *Phys. Chem. Chem. Phys.* **17,** (2015).

41. Ai, N. *et al.* Highly active and stable Er0.4Bi1.6O3 decorated La0.76Sr0.19MnO3+δ nanostructured oxygen electrodes of reversible solid oxide cells. *J. Mater. Chem. A* (2017). doi:10.1039/C7TA02950K

42. Li, M. *et al.* Smart utilization of cobaltite-based double perovskite cathodes on barrier-layer-free zirconia electrolyte of solid oxide fuel cells. *J. Mater. Chem. A* **4,** 19019–19025 (2016).

43. Chen, K. *et al.* Highly Stable Sr-Free Cobaltite-Based Perovskite Cathodes Directly Assembled on a Barrier-Layer-Free Y2O3-ZrO2 Electrolyte of Solid Oxide Fuel Cells. *Journal of Materials Science* **8,** (2016).

44. http://www.rsc.org/publishing/journals/prospect/ontology.asp?id=CMO:0001313&MSID=B101516H.

45. Sammes, N. M., Tompsett, G. A., Näfe, H. & Aldinger, F. Bismuth based oxide electrolytes— structure and ionic conductivity. *J. Eur. Ceram. Soc.* **19,** 1801–1826 (1999).

46. Lee, K. T. *et al.* Interfacial modification of La0.80Sr0.20MnO3−δ–Er0.4Bi0.6O3 cathodes for high performance lower temperature solid oxide fuel cells. *J. Power Sources* **220,** 324–330 (2012).

47. Kim-Lohsoontorn, P., Brett, D. J. L., Laosiripojana, N., Kim, Y. M. & Bae, J. M. Performance of solid oxide electrolysis cells based on composite La0.8Sr0.2MnO3-δ- yttria stabilized zirconia and Ba0.5Sr0.5Co0.8Fe0.2O3-δoxygen electrodes. *Int. J. Hydrogen Energy* **35,** 3958–3966 (2010).

48. Qingshan Zhu, Tongan Jin & Yong Wang. Thermal expansion behavior and chemical compatibility of BaxSr1-xCo1-yFeyO3-δwith 8YSZ and 20GDC. *Solid State Ionics* **177,** 1199–1204 (2006).

49. Zhu, X., Xia, H., Li, Y. & Lü, Z. A (La,Sr)MnO<inf>3</inf> nano-film embedded into (Ba,Sr)(Co,Fe)O<inf>3</inf> porous cathode for stability enhancement. *Mater. Lett.* **161,** 549–553 (2015).

50. Zhou, W., Liang, F., Shao, Z. & Zhu, Z. Hierarchical CO2-protective shell for highly efficient oxygen reduction reaction. *Sci. Rep.* **2,** 327 (2012).

51. M., V. J. & J., G. R. High-Performance SOFC Cathodes Prepared by Infiltration. *Adv. Mater.* **21,** 943–956 (2009).

52. Ai, N., Jiang, S. P., Lü, Z., Chen, K. & Su, W. Nanostructured (Ba , Sr) (Co , Fe) O3 − δ Impregnated (La , Sr) MnO3 Cathode for Intermediate-Temperature Solid Oxide Fuel Cells. *J. Electrochem. Soc.* **157,** B1033–B1039 (2010).

53. Lynch, M. E. *et al.* Enhancement of La0.6Sr0.4Co0.2Fe0.8O3-[small delta] durability and surface electrocatalytic activity by La0.85Sr0.15MnO3+/-[small delta] investigated using a new test electrode platform. *Energy Environ. Sci.* **4,** 2249–2258 (2011).

54. Huang, Y., Vohs, J. M. & Gorte, R. J. An Examination of LSM-LSCo Mixtures for Use in SOFC Cathodes. *J. Electrochem. Soc.* **153,** A951–A955 (2006).

55. Shao, Z. & Haile, S. M. A high-performance cathode for the next generation of solid-state fuel cells. *Nature* **431,** 170–173 (2004).